

III-V Nanowires and Nanoneedles on Lattice Mismatched Substrates for Optoelectronic Device Applications

Chih-Wei Linus Chuang



Electrical Engineering and Computer Sciences
University of California at Berkeley

Technical Report No. UCB/EECS-2011-122

<http://www.eecs.berkeley.edu/Pubs/TechRpts/2011/EECS-2011-122.html>

December 1, 2011

Copyright © 2011, by the author(s).
All rights reserved.

Permission to make digital or hard copies of all or part of this work for personal or classroom use is granted without fee provided that copies are not made or distributed for profit or commercial advantage and that copies bear this notice and the full citation on the first page. To copy otherwise, to republish, to post on servers or to redistribute to lists, requires prior specific permission.

III-V Nanowires and Nanoneedles on Lattice Mismatched Substrates
for Optoelectronic Device Applications

by

Chih-Wei Chuang

A dissertation submitted in partial satisfaction of the

requirements for the degree of

Doctor of Philosophy

in

Engineering-Electrical Engineering and Computer Sciences

and the Designated Emphasis

in

Nanoscale Science and Engineering

in the

Graduate Division

of the

University of California, Berkeley

Committee in charge:

Professor Constance J. Chang-Hasnain

Professor Ming C. Wu

Professor Peidong Yang

Fall 2009

III-V Nanowires and Nanoneedles on Lattice Mismatched Substrates
for Optoelectronic Device Applications

©2009

by Chih-Wei Chuang

Abstract

III-V Nanowires and Nanoneedles on Lattice Mismatched Substrates for Optoelectronic Device Applications

by

Chih-Wei Chuang

Doctor of Philosophy in Engineering-Electrical Engineering and Computer Sciences
and the Designated Emphasis in Nanoscale Science and Engineering

University of California, Berkeley

Professor Constance J. Chang-Hasnain, Chair

We believe that high-speed, low power consumption diode lasers and photodetectors directly integrated onto Si CMOS devices are key elements to high speed optical interconnects. Despite many years of research, integration of direct bandgap III-V compounds onto Si CMOS remains challenging. The bottleneck has been the process incompatibility of the two types of material systems. It is now widely accepted that optoelectronic devices should be fabricated on finished CMOS ICs to avoid these issues. One critical parameter is temperature – the temperature at which high-quality III-V materials can be grown needs to be low enough to sustain CMOS ICs. Another major challenge for the integration is the large lattice mismatch between III-Vs and Si. The large lattice mismatch results in a high misfit dislocation density for III-V thin films grown onto Si which largely degrades the crystal quality.

In this dissertation, I will present III-V nanowires and nanoneedles which we successfully grew dislocation-free on Si and other kinds of lattice mismatched substrates with CMOS-compatible growth temperatures. The strain energy due to the lattice mismatch is relieved via elastic relaxation for these one-dimensional materials.

For the Au-catalytic vapor-liquid-solid III-V nanowires on Si, the nanowires were grown at 430-470°C in a metal-organic chemical vapor deposition system. We observed that there existed a critical diameter for epitaxial nanowires grown on lattice-mismatched substrates, up to as large as 11.6% mismatch for InAs nanowires on Si. Below the critical diameter, well aligned nanowires with bright photoluminescence can grow, while above the critical diameter, spiky structures form. We report well aligned InP nanowires on Si with a very narrow photoluminescence linewidth of 1.4 meV, indicating excellent crystal quality. Regarding the growth parameter study, the precursor V/III ratio could be used to tailor the InP nanowire shape and the optical properties.

For the catalyst-free GaAs-based nanoneedles, including InGaAs and AlGaAs materials, needles were successfully grown on GaAs, Si and sapphire substrates at 400°C. A typical

nanoneedle has a hexagonal cross section with a $6-9^\circ$ taper angle, which results in a high aspect ratio. The nanoneedle tip has only a few atoms in diameter but the base can be sub-micron wide which allows the typical microfabrication processes, such as optical lithography, to be applied. Core-shell GaAs/AlGaAs and InGaAs/GaAs quantum-well nanoneedles are demonstrated with very bright photoluminescence indicating superior material quality. Nanoneedles doped n-type and p-type are also demonstrated with Te and Zn dopants.

Regarding device level work, a GaAs-nanoneedle based photodetector on Si and an InGaAs/GaAs quantum-well nanoneedle-based light emitting diode on Si will also be presented in the dissertation. These III-V optoelectronic devices monolithically integrated on Si demonstrate that high performance optical interconnects for Si CMOS devices could be realized with these novel one dimensional materials.

Dedicated to my loving family,

Liz

Mimi

&

Adrian

Table of Contents

Chapter 1 Introduction	1
1.1 <i>Introduction to Nanowires</i>	1
1.2 <i>Introduction to Nanoneedles</i>	2
Chapter 2. Critical Diameter for III-V Nanowires Grown on Lattice-Mismatched Substrates	5
2.1 <i>Nanowire Growth</i>	5
2.2 <i>Nanowire Structural Properties</i>	6
2.3 <i>Nanowire Optical Properties</i>	10
Chapter 3. Optical Properties of InP Nanowires on Si Substrates with Varied Synthesis Parameters	13
3.1 <i>InP Nanowire Structural Properties with Different V/III Ratios</i>	13
3.2 <i>InP Nanowire Optical Properties with Different V/III Ratios</i>	14
Chapter 4. GaAs-Based Nanoneedles Including InGaAs, AlGaAs and Quantum Wells	19
4.1 <i>The Discovery of Nanoneedle Growth Mode</i>	20
4.2 <i>GaAs Nanoneedle Growth Details</i>	23
4.3 <i>GaAs Nanoneedle Structural Properties</i>	24
4.4 <i>GaAs Nanoneedle Optical Properties</i>	29
4.5 <i>InGaAs Nanoneedle and InGaAs/GaAs Quantum Wells</i>	31
4.6 <i>AlGaAs Nanoneedle and GaAs/AlGaAs Heterostructures</i>	36
Chapter 5. Doping of GaAs Nanoneedles and Nanoneedle P-N Junctions ...	43
5.1 <i>n-type GaAs Nanoneedle with Disilane (Si₂H₆) Doping Source</i>	43

5.2 <i>n</i> -type GaAs Nanoneedle with Diethyltellurium (DETe) Doping Source	47
5.3 <i>p</i> -type GaAs Nanoneedle with Diethylzinc (DEZn) Doping Source	51
5.4 <i>P-N</i> Junctions in a GaAs Nanoneedle	55
Chapter 6 .InGaAs/GaAs Nanoneedles on Si for Photodetector and Light Emitting	
Diode Applications	62
6.1 GaAs-Based Nanoneedle Photodetectors on a Si Substrate	62
6.2 GaAs/InGaAs Quantum-Well-Based Nanoneedle Light Emitting Diodes on a Si Substrate	71
Chapter 7. Wurtzite GaAs Nanoneedles Epitaxially Grown on 46% Lattice-	
mismatched Sapphire with Bright Luminescence	76
7.1 Structural Properties of GaAs Nanoneedles Grown on Sapphire	76
7.2 Nucleation Theory for GaAs Nanoneedles Grown on Sapphire	83
7.3 Optical Properties of GaAs Nanoneedles Grown on Sapphire	86
Chapter 8. Conclusion	92

Acknowledgements

I would like to express my deepest gratitude to my adviser, Prof. Connie Chang-Hasnain. Her guidance and support to my research were the best of what I could have thought of. Her enthusiasm, devotion and persistence to the research and science made me realize and learn what the essential elements were behind a long list of quality publications. I would also like to thank Prof. Chang-Hasnain for creating an innovative and supportive group environment, which I have been lucky to stay in for the past five and a half years.

In addition, I would like to thank Prof. Ming Wu, Prof. Peidong Yang and Prof. Ivan Kaminow for being in my dissertation and qualification-exam committees. Their generous and insightful advice greatly helped me expand the background of my research.

I deeply appreciate my parents for encouraging me to do what I wanted to do, which included traveling to and studying at the other side of the Pacific Ocean. I also appreciate my very supportive wife, Liz, for taking care of my little family while pursuing her own PhD degree. I would say that talking and playing with my two lovely kids, Mimi and Adrian, could counteract all the frustrations I have from elsewhere. They keep me seeing the very bright side of everyday life.

I have many thanks to my wonderful labmates. I especially would like to thank Michael Moewe and Kar Wei “Billy” Ng, who shared the most workload with me on the material growth. Wai Son “Wilson” Ko’s later joining the growth group also helped to move my research forward in a faster pace. The multi-talented Wilson also did device simulations to enrich the analyses for our nanoneedle devices. I appreciate it. I have always been amazed how fast and accurate Forrest Sedgwick could set up an optical/electrical characterization tool from scratch which provided the most needed measurements for the nanoneedle devices. His strong physics background led to lots of insightful observations and later helpful discussions. The same credit goes to Roger Chen, Thai-Truong Tran and Shanna Crankshaw. I appreciate their helping out with the characterization of nanowire/nanoneedle materials and with their attention to detail to even the finest features on the spectra. I also would like to thank Chris Chase for initiating the nanowire/nanoneedle-related processes and provided a lot of discussions for the later process development. Again the same credit goes to our group alumni, Mike Huang and Ye “Mervin” Zhou. Some early-days MOCVD work with Nobuhiko “Nobby” Kobayashi and Pei-Cheng “P. C.” Ku, when I first came to UCB, proved to provide me a solid ground to stand on. I appreciate that. I would also like to thank all other labmates whom I do not specifically list above as their intellectual support and friendship would actually deserve a separate paragraph to describe.

My deepest gratitude also goes to many outside collaborators. Through the collaboration with Prof. Vladimir Dubrovskii, we were able to have a theory describing our nanowire and especially the novel nanoneedle growth. I also want to thank Ralph Rothmund for measuring the nanoneedle optical properties and providing the related analyses during his one-year visit to UCB.

Chapter 1: Introduction

The nanowires and nanoneedles to be discussed in this dissertation are quasi-one-dimensional semiconductor structures. They are the last frontier of the low-dimensional structure researches after the maturation of the two-dimensional quantum-well structures in the 1980's and the booming of the zero-dimensional quantum-dot structures in the 1990's. With the International Technology Roadmap for Semiconductors (ITRS) technology node size came to 130 nm in 2002 and 100 nm in 2005,¹ the need of nanometer-scale one-dimensional structures was evident, for example, as an improved FET channel material.² These one-dimensional structures also have a large impact to the optoelectronics since the versatility of the nanowire and nanoneedle material systems include a vast amount of important direct-bandgap materials.^{3,4}

1.1 Introduction to Nanowires

Nanowires, particularly the III-V compound semiconductor nanowires to be discussed in this dissertation have drawn much attention since 2000. Fig. 1.1 shows the number of the III-V-nanowire-related papers versus the year published. It is clearly seen that the number of papers per year has been growing rapidly and the trend continues. The statistical data is taken from a keyword search from the Web-of-Science database. Details of the search are given in the figure caption. Not only does the one-dimensional quantum confinement intrigue people, but also the unique geometrical shape with high aspect ratio results in new and creative ways to construct functional devices with these fundamental nanowire blocks.^{2,5}

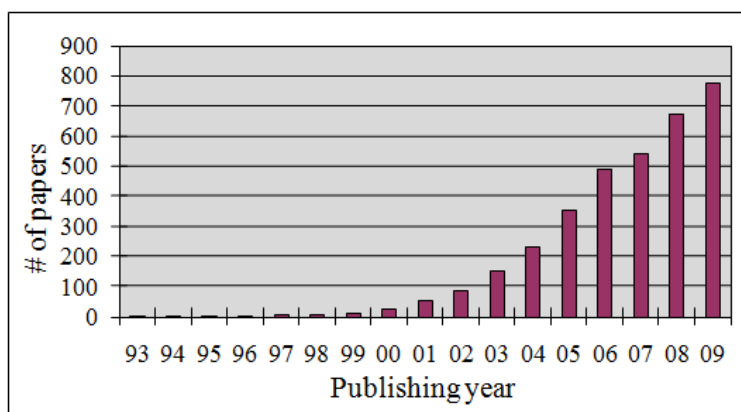


Figure 1.1 Number of III-V nanowire papers versus year published. Data was obtained from the Web-of-Science database with the following combination of keywords, “(nanowire OR nanowires) AND (III OR InP OR GaAs OR GaP OR InAs OR GaN OR InN OR AlN)”. The capital “OR” and “AND” here are Boolean operations.

One of the constraints for conventional heteroepitaxy is the existence of a critical thickness, which limits the dislocation-free thickness of a strained layer.⁶ Nanowires, due to their unique one-dimensional shapes, on the other hand, can relieve strain energy by lateral elastic relaxation.^{7,8} Therefore an initially strained nanowire, in principle, can be grown infinitely long without generating any dislocation, as long as its footprint is smaller than the critical diameter. Ertekin *et al.*⁷ and Glas⁸ modeled this problem using equilibrium analysis to predict the critical diameters as a function of lattice mismatch. The critical diameter decreases as lattice mismatch increases, as it intuitively would. This lateral relaxation opens an opportunity to integrate high-quality III-V nanowires onto Si-based circuits. Therefore, some fundamental research for growing III-V nanowires on Si substrates was conducted recently.⁹

A few methods were investigated to synthesize nanowires in the early days of nanowire research. Some are based on vapor phase reactants, such as vapor-liquid-solid (VLS)¹⁰ and vapor-solid (VS)¹¹ processes. Some are based on the pure solution-phase techniques.¹² Among these methods, the VLS method is the most widely used because it offers a controlled synthesis of a broad range of semiconductor nanowires. The catalyst is a nanocluster or nanodroplet that defines the diameter of a nanowire and serves as the site that directs preferentially the addition of vapor-phase reactants to the end of a growing nanowire. The identification of a VLS growth mode is usually from the remaining catalyst droplet on the nanowire tip.

In this dissertation, I will present VLS InP and InAs nanowires, which we successfully grew dislocation-free on Si and other kinds of lattice-mismatched substrates with CMOS-compatible growth temperatures of 430-470°C. We observed that there existed a critical diameter for epitaxial nanowires grown on lattice-mismatched substrates, up to as large as 11.6% mismatch for InAs nanowires on Si.¹³ Below the critical diameter, well aligned nanowires with bright photoluminescence can grow, while above the critical diameter, spiky structures form. We report well aligned InP nanowires on Si with a record narrow photoluminescence linewidth of 1.4 meV, indicating excellent crystal quality. Regarding the nanowire growth parameter study, the precursor V/III ratio could be used to tailor the InP nanowire shape and the optical properties.¹⁴

1.2 Introduction to Nanoneedles

A nanoneedle is a special type of nanowire which has at least the following two unique properties. First, a nanoneedle tip is atomically sharp which typically has only a few atoms wide. Second, the needle-like shape also comes from its tapered sidewall.¹⁵ Nanoneedles are a new field of research as the same type of literature search as the nanowire counterpart shown in Fig. 1.1, returned with only 46 matches. In order to have a sharp tip, nanoneedles usually are not grown via VLS otherwise the tip size would be bound to the metal catalyst size. Two advantages of nanoneedles are found and they correspond to the above two features. First the usually catalyst-free growth would avoid any possible contamination from the metal catalyst used in VLS growth. For example, Au is a known deep level for Si. Second, the taper nanoneedle shape results in a thick root which is robust enough to mechanically support the nanoneedle structure through typical microfabrication processes such as photolithography.

In this dissertation, I will present catalyst-free GaAs-based nanoneedles, including InGaAs and AlGaAs materials, successfully grown on GaAs, Si and sapphire substrates at a CMOS-compatible low growth temperature of 400°C. A typical nanoneedle has a hexagonal cross

section with a 6-9° taper angle, which results in a high aspect ratio. The nanoneedle tip has only a few atoms in diameter, but the base can be sub-micron wide which allows the typical microfabrication processes, such as optical lithography, to be applied. Core-shell GaAs/AlGaAs and InGaAs/GaAs quantum-well nanoneedles are demonstrated with very bright photoluminescence indicating superior material quality.^{15,16} Nanoneedles doped n-type and p-type are also demonstrated with Te and Zn dopants.

By utilizing the mechanically robustness of these nanoneedles, a GaAs-nanoneedle based photodetector on Si and an InGaAs/GaAs quantum-well nanoneedle-based light emitting diode on Si were demonstrated. I will also present this exciting device-level work in the dissertation. These III-V optoelectronic devices monolithically integrated on Si demonstrate that high performance optical interconnects for Si CMOS circuits or other Si photonics applications could be realized with these novel nanoneedle materials.

References:

- (1) *International Technology Roadmap for Semiconductors* (Semiconductor Industry Association, San Jose, CA, 2000).
- (2) Thelander, C. *et al.* Nanowire-based one-dimensional electronics. *Mater. Today* **9**, 28-35 (2006).
- (3) Li, Y., Qian, F., Xiang, J., & Lieber, C. M. Nanowire electronic and optoelectronic devices. *Mater. Today* **9**, 18-27 (2006).
- (4) Pauzauskis P. & Yang P. Nanowire photonics. *Mater. Today* **9**, 36-45 (2006).
- (5) Law, M., Goldberger, J., & Yang, P. Semiconductor nanowires and nanotubes. *Annu. Rev. Mater. Res.* **34**, 83-122 (2004).
- (6) Matthews, J. W. & Blakeslee, A. E. Defects in epitaxial multilayers. *J. Cryst. Growth* **27**, 118-125 (1974).
- (7) Ertekin, E., Greaney, P. A., Chrzan, D. C., & Sands, T. D. Equilibrium limits of coherency in strained nanowire heterostructures. *J. Appl. Phys.* **97**, 114325 (2005).
- (8) Glas, F. Critical dimensions for the plastic relaxation of strained axial heterostructures in free-standing nanowires. *Phys. Rev. B* **74**, 121302 (2006).
- (9) Mårtensson, T. *et al.* Epitaxial III-V nanowires on silicon. *Nano Lett.* **4**, 1987-1990 (2004).
- (10) Wagner, R.S. & Ellis, W. C. Vapor-liquid-solid mechanism of single crystal growth. *Appl. Phys. Lett.* **4**, 89-90 (1964).
- (11) Dai, Z. R., Pan, Z. W., & Wang, Z. L. Novel nanostructures of functional oxides synthesized by thermal evaporation. *Adv. Funct. Mater.* **13**, 9-24 (2003).
- (12) Greene, L. E. *et al.* Low-temperature wafer-scale production of ZnO nanowire arrays. *Angew. Chem. Int. Ed.* **42**, 3031-3034 (2003).
- (13) Chuang, L. C., Moewe, M., Chase, C., Kobayashi, N. P., and Chang-Hasnain, C. Critical diameter for III-V nanowires grown on lattice-mismatched substrates. *Appl. Phys. Lett.* **90**, 043115 (2007).
- (14) Chuang, L. C., Moewe, M., Crankshaw, S. & Chang-Hasnain, C. Optical properties of InP nanowires on Si substrates with varied synthesis parameters. *Appl. Phys. Lett.* **92**, 013121 (2008).

- (15) Moewe, M., Chuang, L. C., Crankshaw, S., Chase, C., & Chang-Hasnain, C. Atomically sharp catalyst-free wurtzite GaAs/AlGaAs nanoneedles grown on silicon, *Appl. Phys. Lett.* **93**, 023116 (2008).
- (16) Moewe, M., Chuang, L. C., Crankshaw, S., Ng, K. W., & Chang-Hasnain, C. Core-shell InGaAs/GaAs quantum well nanoneedles grown on silicon with silicon-transparent emission. *Opt. Express* **17**, 7831-7836 (2009).

Chapter 2:

Critical Diameter for III-V Nanowires Grown on Lattice-Mismatched Substrates

Monolithic integration of semiconductors with different lattice constants has excited much interest because of its promise to combine the best performance of different material systems.¹ In particular, it is desirable to integrate compound semiconductors onto a Si substrate, where Si is the prevalent platform for microelectronics, and compound semiconductors for light emitting diodes and lasers. Past attempts failed due to high defect densities resulting from large lattice mismatches and high temperatures required for typical epitaxial synthesis ($\sim 600^\circ\text{C}$).^{2,3} Nanowires grown by the vapor-liquid-solid (VLS) mechanism⁴ are promising because of the substantially lower temperatures reported ($400\text{-}500^\circ\text{C}$).⁵⁻¹¹ Typical Si CMOS back-end processes require temperatures below 450°C . Recently, theoretical calculations on equilibrium limitations for coherent growth of strained nanowires were reported.^{12,13} Here, I will present our experimental observation that there exists a critical diameter for epitaxial nanowires grown on lattice-mismatched substrates, up to as large as 11.6%. Below the critical diameter, well-aligned nanowires with bright photoluminescence can grow, while above the critical diameter, spiky structures form. The epitaxial nanowires possess excellent optical properties and will be discussed shortly. The highly strain-tolerant epitaxial III-V nanowire growth on Si may serve as a guideline to synthesize defect-free compound semiconductor materials on Si substrates.

2.1 Nanowire Growth

We use colloidal Au nanoparticles as catalysts in a low-pressure metal-organic chemical vapor deposition (MOCVD) reactor (EMCORE D75) with the VLS growth mode. In the following experiment, five material combinations and various sizes of Au nanoparticles are used to study the growth as a function of lattice mismatch and catalyst size. The material combinations are listed in Table 2.1. The Au nanoparticle size ranges from 10 nm to 160 nm. To derive the size-dependent information, Au nanoparticles with different sizes were placed onto different parts of the same substrate for a given growth run.

Table 2.1 Material combinations used in this work for obtaining different lattice mismatches.

Nanowire/substrate	InAs/Si	InP/Si	InP/GaAs	GaP/Si	InP/InP
Lattice mismatch (%)	11.6	8.1	3.8	0.4	0

The growth process on a Si substrate begins with cleaning the substrate with a standard 3-step process in the sequence of acetone, methanol and de-ionized water for 3 minutes each. The Si substrate is then chemically deoxidized in a 5:1 buffered oxide etch for 3 min. Au nanoparticle solution, which is with a toluene solvent, is then dispensed onto the Si substrate. After the solvent evaporates, the substrate containing Au nanoparticles and the toluene residue is then immediately transferred into the loadlock chamber of an MOCVD system to avoid oxidation. The substrate is first annealed at 606°C for 3 minutes before the introduction of any sources. This annealing step was originally meant to convert a thin Au film onto the substrate surface into small Au droplets in some even earlier experiments. When Au nanoparticles are used, like the current experiment, this annealing step should be ok to be taken away since the Au/Si eutectic point is only 363°C. The nanowire growth temperature of 430-470°C would already be high enough to convert the solid-phase Au nanoparticles into liquid Au/Si droplets. However, for the experiments described in this chapter, this annealing step was still left there. After the pre-growth annealing, the reactor temperature is brought down to typically 470°C for the nanowire growth. Metal-organic sources used in this work were tertiarybutylphosphine (TBP), tertiarybutylarsine (TBA), trimethylindium (TMI) and triethylgallium (TEGa). In this study, the growth temperature (430-470°C), pre-growth annealing temperature (610-660°C), V/III ratio, growth rate, growth pressure, and substrate orientation were experiment parameters. More than 120 growth runs, including many with repeated conditions, were conducted. The platter which holds the substrate spins at 1400 rpm at a pressure of 76 Torr during the growth. The optimum V/III ratio for growing InP nanowires is 60-90, which will be described into more detail in the next chapter. The typical V/III ratio for InAs nanowires is ~20.

For the growth on a GaAs substrate, the wafer cleaning process is the same. The deoxidation process is done through a 3-min 10:1 diluted HCl solution for 3 min, or until the surface becomes hydrophobic. The remaining growth procedures for a GaAs substrate are exactly the same as those for a Si substrate.

2.2 Nanowire Structural Properties

Nanowire structural properties were first investigated under a field-emission scanning electron microscope (FE-SEM). Fig 2.1 shows a 20°-tilt SEM picture for InAs nanowires grown on a (111) Si substrate, with 11.6 % lattice mismatch. The thickest epitaxial nanowire found has a 26 nm diameter. The Au nanoparticle size used for this InAs nanowire growth was determined by SEM in a separate, anneal-only run to be nominally 20 nm, with a wide size distribution from 10 nm to 40 nm. Hence we deduce that the maximum epitaxial nanowire diameter of 26 nm was due to the existence of a critical diameter. Above this critical diameter, epitaxial nanowires do not exist.

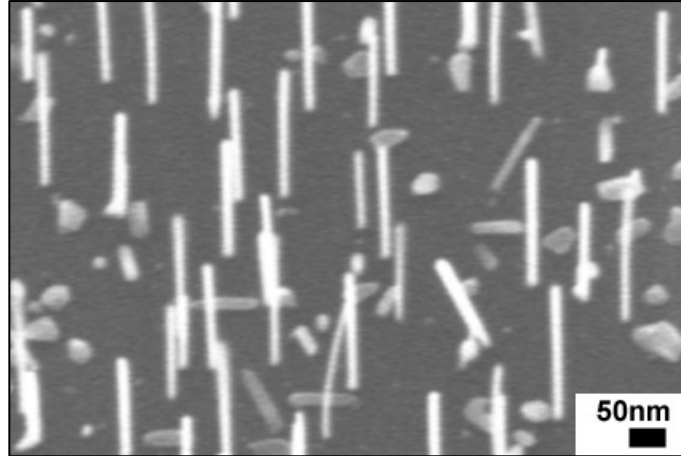


Figure 2.1 20°-tilt SEM image of InAs nanowires grown on a (111)Si substrate. Epitaxial nanowires up to 26 nm in diameter can be seen implying that this is the critical diameter for this 11.6% lattice-mismatched system.

Fig. 2.2, a-c, show 20°-tilt SEM images for InP nanostructures grown on a (111)Si substrate using nominal (a) 20 nm, (b) 60 nm, and (c) 120 nm Au nanoparticles, respectively. With 8.1% lattice mismatch, only the 20 nm-Au region supports epitaxial nanowire growth with vertically aligned nanowires along the [111] direction. In the 60 and 120 nm Au nanoparticle regions, spiky star-like structures are created. For this case, the critical diameter was found to be 36 nm. The spiky structures already suggest that these materials might have a high dislocation density.

Fig. 2.2d shows a typical transmission electron microscopy (TEM) image for a 17 nm InP nanowire on Si. No dislocations were observed along the 450 nm length of the nanowire. Furthermore, the period between the image planes is 3.4 Å throughout the full length of the nanowire, in agreement with the period for fully relaxed wurtzite InP (0001) planes.

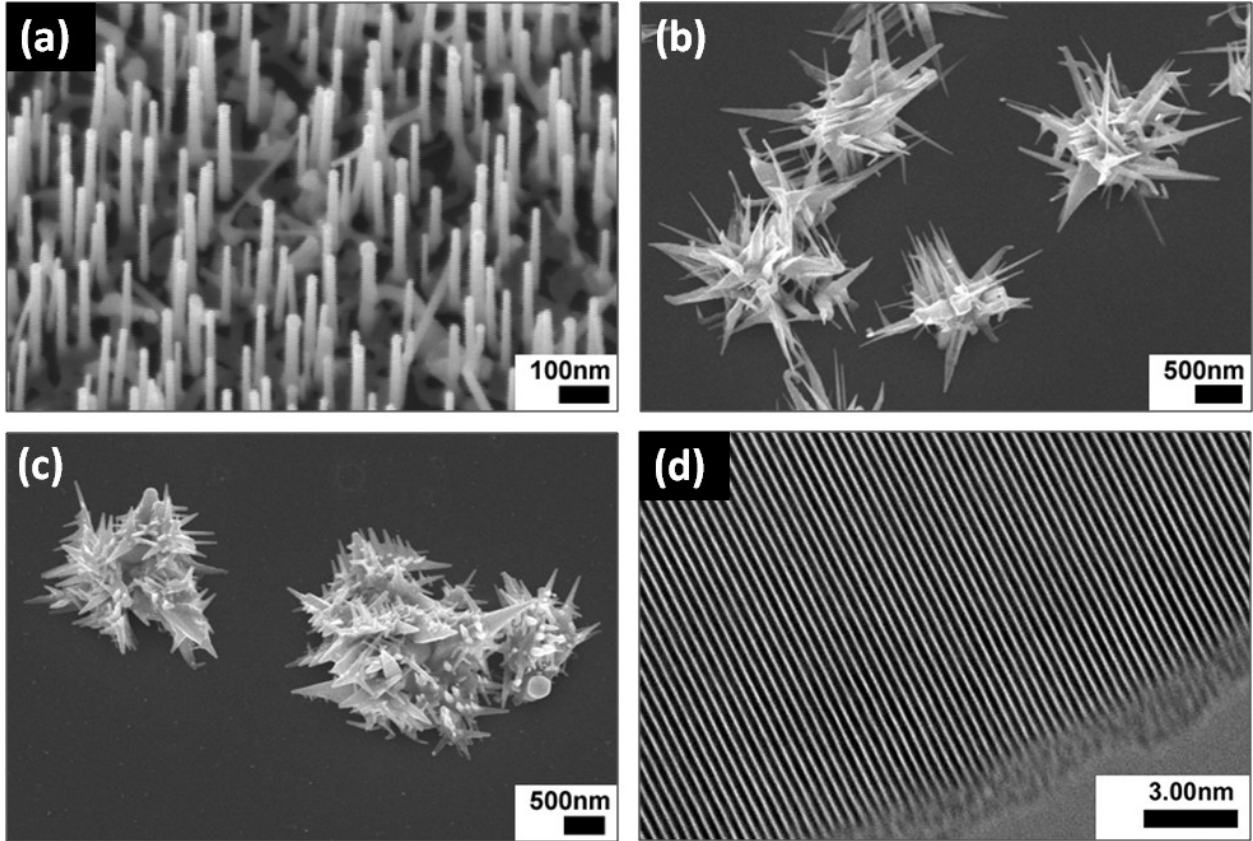


Figure 2.2 20°-tilt SEM pictures for InP nanostructures grown on (111) Si substrates. (a) InP nanowires grown with nominal 20 nm Au nanoparticles. (b)(c) Star-like InP structures using nominal (b) 60 nm and (c) 120 nm Au nanoparticles, respectively. (d) TEM image of a 17 nm diameter InP nanowire showing clear wurtzite (0001) planes perpendicular to growth axis with 3.4 Å spacing. No dislocations were observed along the entire 450 nm nanowire length.

Fig. 2.3a shows the SEM picture of InP nanowires grown on a (111)B GaAs substrate with a mixture of nominally 20 nm and 60 nm Au nanoparticles. With 3.8% lattice mismatch, well-aligned, epitaxial nanowires are obtained with both 20 nm and 60 nm Au nanoparticles. A clear bimodal distribution of nanowire diameters appears in this region, supporting that the dominant factor for nanowire size is the catalyst size as long as it is less than the critical diameter. In the 120 nm-Au-nanoparticle region (shown in Fig. 2.3b), branching is observed. The critical diameter in this case is 96 nm.

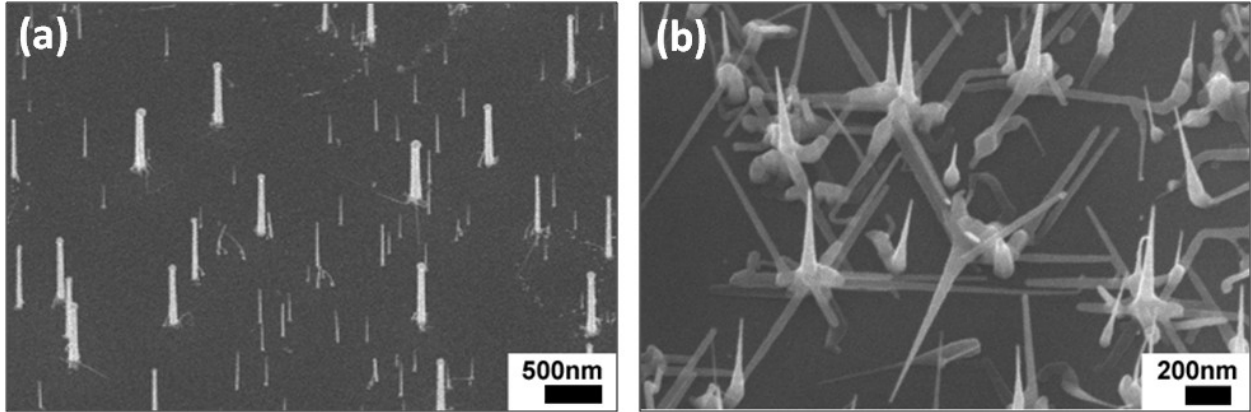


Figure 2.3 20°-tilt SEM pictures for InP nanowires grown on a (111)B GaAs substrate with (a) a mixture of nominal 20 nm and 60 nm Au-nanoparticle catalysts. (b) A region with nominal 120 nm Au nanoparticle catalysts. The branching of nanowires is clearly seen.

A quasi-lattice-matched system, GaP/Si, was also tested with GaP nanowires grown on a (100)Si substrate. For this sample, a thin $\sim 8 \text{ \AA}$ Au film was used, instead of Au nanoparticles, as the catalyst. The GaP nanowires are seen grown along the four equivalent $\langle 111 \rangle$ directions and they are all epitaxial (Fig. 2.4a). The GaP nanowire diameters seen here are between 60-98 nm. The all-epitaxial feature implies that the critical diameter for this 0.4% lattice-mismatched system is beyond 98 nm. A truly lattice-matched system with InP nanowires on a (100) InP substrate was also tested. Epitaxial nanowires as thick as 273 nm (shown in Fig. 2.4b) and even thicker were seen. This verifies that there should not be a critical diameter for a lattice-matched system.

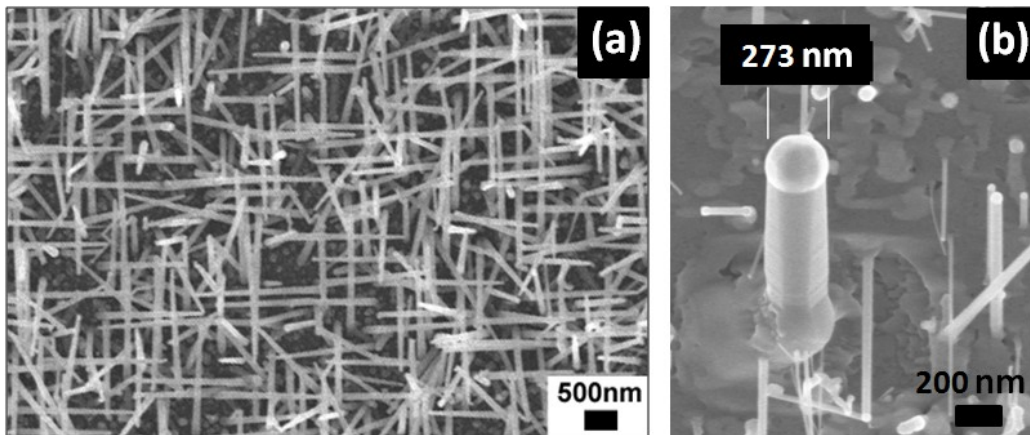


Figure 2.4 (a) GaP nanowires grown on a (100)Si substrate. A $\sim 8 \text{ \AA}$ Au film was used as the catalyst for this sample. Au film was converted into Au droplets during the pre-growth annealing process. All the GaP nanowires are seen epitaxial here with a diameter of 60-98 nm, which is dictated by the Au droplet size. (b) A thick, epitaxial InP nanowire grown on a (100) InP substrate.

Fig. 2.5 summarizes these growth results. The pink, dashed curve in this figure is the theoretical curve of the misfit-dislocation-free critical diameter from Ertekin¹² for comparison. An equilibrium model similar to the Matthews critical thickness model¹⁴ was used to calculate the misfit-dislocation-free critical diameter. When the nanowire diameter is less than misfit-dislocation-free critical diameter, the nanowire will be coherent everywhere solely via lateral relaxation. Another theoretical curve from Glas¹³ is also shown in the figure as the black, dashed curve. The epitaxial-nanowire critical diameters experimentally obtained in this work were fitted by the solid blue curve. Our experimental critical-diameter curve fits the Glas's theory well and has a similar trend to the Ertekin's curve. It is worthwhile to note that the theories mentioned above were done assuming equilibrium growth conditions without considering the kinetic factors hence a small deviation is reasonable and expected.¹⁵⁻¹⁷

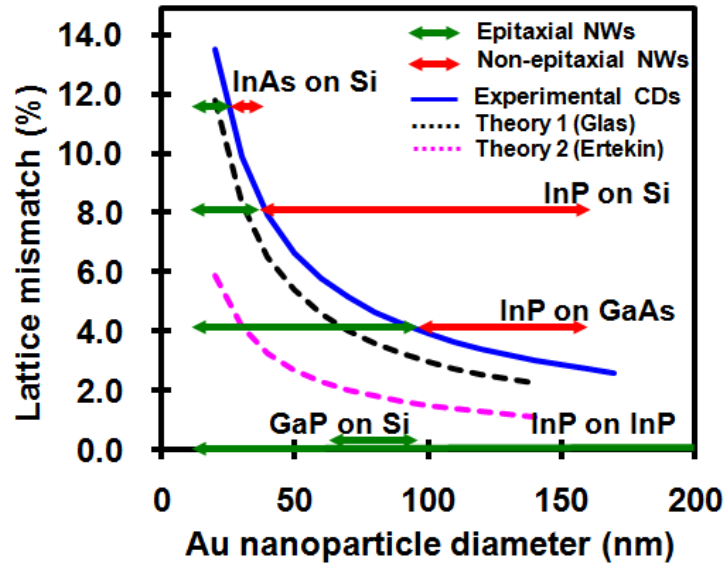


Figure 2.5 The experimental nanowire (NW) critical diameters (CDs) as a function of lattice mismatch. Two theoretical curves from Ertekin¹² and Glas,¹³ respectively, are shown here. Green arrows denote that epitaxial nanowires within this size range were observed. Red arrows denote that Au nanoparticles within this size range were used as catalysts but no corresponding epitaxial nanowire could be found. Hence the boundary between a green arrow and a red arrow is the experimental critical diameter for that particular lattice mismatch. The three critical-diameter data points found in this work were then fitted with the blue curve.

2.3 Nanowire Optical Properties

The linewidth and intensity of photoluminescence (PL) are key indicators of the material optical quality. The PL linewidth is particularly critical as its broadening often results from structural fluctuations and defects. A broad PL linewidth has deleterious effects on devices such as lasers.¹⁸ Hence, it is crucial to obtain a narrow linewidth for optoelectronic applications. Fig. 2.6a shows micro-PL (μ -PL) results of as-grown InP nanostructures on (111)Si (see Fig. 2.2) at 4 K, with an excitation laser beam size of $\sim 1.5 \mu\text{m}$. The excitation source is a diode-pumped solid-state laser at 532 nm. The power used was extremely low: 120 nW, corresponding to a power density of 6.8

W/cm². Fig. 2.6a compares typical μ -PL spectra for nanowires (20 nm Au catalyst) and star-like structures (60 and 120 nm Au catalysts). A sharp peak at 1.597 eV with a full width half maximum (FWHM) of 5.1 meV is observed for a single nanowire. Furthermore, the brightness of this emission, when normalized to the volume of the nanowire, is comparable with that of a standard GaAs/AlGaAs multi-quantum-well sample. The μ -PL spectra for star-like structures have a broad FWHM (\sim 60 meV). The inset shows the PL intensity normalized by the nanostructure volume. The brightness of nanowire is over four orders of magnitude higher than that of the star-like structures, which attests the good optical quality of the nanowires.

Another even sharper PL peak from an epitaxial InP nanowire on (111)Si is shown in Fig. 2.6b. The 1.4 meV FWHM is the narrowest that has ever been reported. The single-nanowire PL shows a 178 meV blueshift from the InP bandgap (1.424 eV) due to quantum confinement. This was also the most significant blueshift ($\Delta E/E \sim 12.5\%$) ever reported in nanowires.

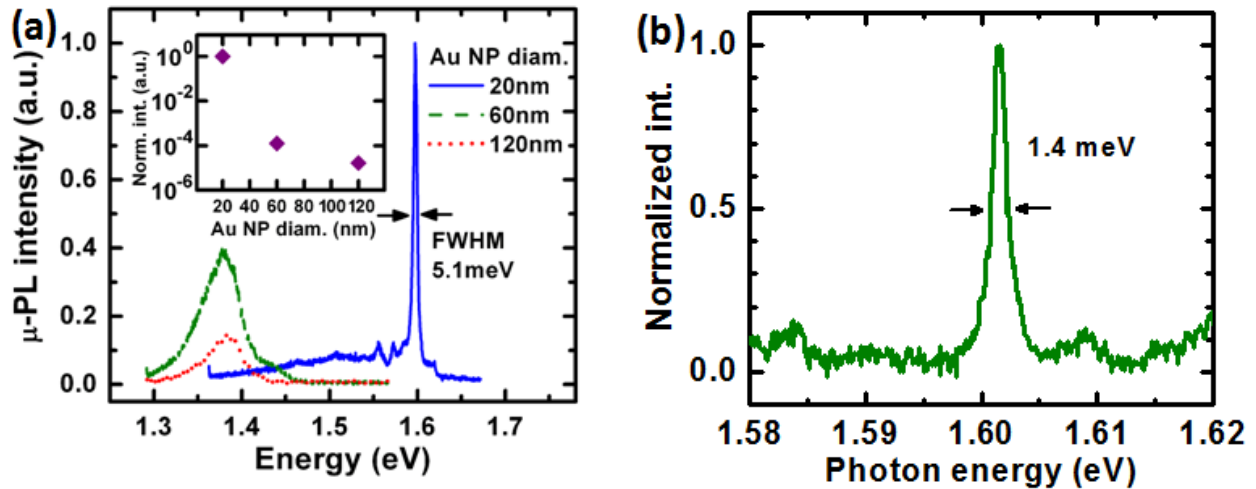


Figure 2.6 (a) Low temperature (4 K) μ -PL spectra of InP nanostructures on (111)Si for nanowires (20 nm Au nanoparticle catalyst) and star structures (60 nm and 120 nm Au nanoparticles). A single-nanowire PL shows a sharp peak with a narrow 5.1 meV FWHM with a 173 meV blueshift from the InP bandgap. The inset shows the μ -PL intensity normalized to nanostructure volume. (b) A record-narrow PL linewidth of 1.4 meV of an epitaxial InP nanowire. A larger blueshift of 178 meV due to quantum confinement is also observed.

In conclusion, we report the experimental evidence of a critical diameter for epitaxial-nanowires on lattice-mismatched substrates, with nanowires smaller than this value demonstrating extremely narrow PL linewidths and bright PL intensity. We show that critical diameter is inversely dependent on the lattice mismatch. The critical diameter can serve as a general guideline in heterogeneous material growth for obtaining high brightness, well-aligned III-V nanowires on Si or other dissimilar substrates. This observation will be important for monolithic integration of optoelectronic and electronic devices with highly mismatched lattice constants.

References:

- (1) Soref, R. A. Silicon-based optoelectronics. *Proc. IEEE* **81**, 1687-1706 (1993).
- (2) Fang, S. F. *et al.* Gallium arsenide and other compound semiconductors on silicon. *J. Appl. Phys.* **68**, R31-R58 (1990).
- (3) Lum, R. M. *et al.* Effects of misfit dislocations and thermally induced strain on the film properties of heteroepitaxial GaAs on Si. *J. Appl. Phys.* **64**, 6727-6732 (1988).
- (4) Wagner, R.S. & Ellis, W. C. Vapor-liquid-solid mechanism of single crystal growth. *Appl. Phys. Lett.* **4**, 89-90 (1964).
- (5) Hiruma, K. *et al.* Growth and optical properties of nanometer-scale GaAs and InAs whiskers. *J. Appl. Phys.* **77**, 447-462 (1995).
- (6) Duan, X., Huang, Y., Agarwal, R., & Lieber, C. M. Single-nanowire electrically driven lasers. *Nature* **421**, 241-245 (2003).
- (7) Huang, Y. *et al.* Logic gates and computation from assembled nanowire building blocks. *Science* **294**, 1313-1317 (2001).
- (8) Mårtensson, T. *et al.* Epitaxial III-V nanowires on silicon. *Nano Lett.* **4**, 1987-1990 (2004).
- (9) Björk, M. T., *et al.* One-dimensional heterostructures in semiconductor nanowhiskers. *Appl. Phys. Lett.* **80**, 1058-1060 (2002).
- (10) Wu, Y., Fan, R., & Yang, P. Block-by-block growth of single-crystalline Si/SiGe superlattice nanowires. *Nano Lett.* **2**, 83-86 (2002).
- (11) van Weert, M. H. M. *et al.* Large redshift in photoluminescence of p-doped InP nanowires induced by Fermi-level pinning. *Appl. Phys. Lett.* **88**, 043109 (2006).
- (12) Ertekin, E., Greaney, P. A., Chrzan, D. C., & Sands, T. D. Equilibrium limits of coherency in strained nanowire heterostructures. *J. Appl. Phys.* **97**, 114325 (2005).
- (13) Glas, F. Critical dimensions for the plastic relaxation of strained axial heterostructures in free-standing nanowires. *Phys. Rev. B* **74**, 121302 (2006).
- (14) Matthews, J. W. & Blakeslee, A. E. Defects in epitaxial multilayers. *J. Cryst. Growth* **27**, 118-125 (1974).
- (15) Dodson, B. W. & Tsao, J. Y. Relaxation of strained-layer semiconductor structures via plastic flow. *Appl. Phys. Lett.* **51**, 1325-1327 (1987).
- (16) Dong, L., Schnitker, J., Smith, R. W., & Srolovitz, D. J. Stress relaxation and misfit dislocation nucleation in the growth of misfitting films: A molecular dynamics simulation study. *J. Appl. Phys.* **83**, 217-227 (1998).
- (17) Orders, P. J. & Usher, B. F., Determination of critical layer thickness in $\text{In}_x\text{Ga}_{1-x}\text{As}/\text{GaAs}$ heterostructures by x-ray diffraction. *Appl. Phys. Lett.* **50**, 980-982 (1987).
- (18) Hader, J. *et al.* Quantitative prediction of semiconductor laser characteristics based on low intensity photoluminescence measurements. *IEEE Photon. Tech. Lett.* **14**, 762-764 (2002).

Chapter 3:

Optical Properties of InP Nanowires on Si Substrates with Varied Synthesis Parameters

Integration of III-V compound materials with Si has been an important research area for monolithic integration of semiconductor diode lasers and Si-based electronic circuits.¹⁻⁴ I mentioned, in the previous chapter, that past attempts have not been successful due to high defect densities resulting from a large lattice mismatch and process incompatibility with CMOS from the high growth temperatures of epilayers.^{5,6}

In Chapter 2, I showed that we have successfully grown dislocation-free III-V nanowires on Si with excellent optical properties with a low growth temperature (430-470°C) using MOCVD.⁷ In this chapter, I will discuss the effect of the precursor V/III ratio on the shape and optical properties of InP nanowires grown on (111) Si substrates. The V/III ratio can be used to tailor the nanowire shape and optical properties. In particular, with the optimum growth condition, we grew nanowires with uniform diameters along the axial direction with a record narrow photoluminescence (PL) peak of 1.4 meV and a large blueshift of 178 meV due to quantization. These uniform nanowires also have less power dependence for their PL emission peak. This wavelength stability is important for critical applications such as nanowire lasers. The PL intensity can also be maximized when using high V/III ratios.

3.1 InP Nanowire Structural Properties with Different V/III Ratios

Five InP-nanowire-on-(111)Si samples were grown with V/III ratios equal to 15, 30, 67, 180 and 240. The Si substrates were first cleaned and then chemically deoxidized with buffered oxide etch followed by Au nanoparticle dispensing. Colloidal Au nanoparticles with an average of 20 nm in diameter were used as the catalysts for VLS nanowire growth. The growth details were given in Chapter 2.1.

The group V and group III precursors were tertiarybutylphosphine (TBP) and trimethylindium (TMIn), respectively. The TMIn mole fraction was held at 1.9×10^{-5} in a 12 l/min hydrogen carrier gas flow for all the growths. The TBP mole fraction was varied to attain the five V/III ratios: 15, 30, 67, 180 and 240 (samples A, B, C, D, and E, respectively). The V/III ratios we quote above are the supplied gas-phase mole ratios which are the input experimental parameters for the nanowire syntheses in this work. The growth time was three minutes for all the samples and the growth pressure was 76 Torr. The nanowire shape was characterized by FE-SEM.

Fig.3.1 shows the FE-SEM images of the five InP nanowire/(111)Si samples. With increasing V/III ratio, a significant nanowire shape change was observed. With a low V/III = 15, nanowires did not grow due to insufficient phosphorus (Fig. 3.1a). Many indium-rich balls, whose composition was determined by SEM energy dispersive spectroscopy, were observed. Improvement for nanowire formation is seen for sample B with V/III = 30 (Fig. 3.1b). Nanowires on sample C, with V/III = 67, have uniform diameter along the entire nanowire length (Fig.

3.1c). Further increasing the V/III ratio resulted in tapered nanowires with wider bases and narrow tips, shown in Fig. 3.1d and 1e, with V/III ratios equal to 180 and 240, respectively. The tapering is attributed to an increase in the thin-film deposition rate on nanowire sidewalls comparing to that of the vertical VLS growth. The dependence of thin film growth rate on V/III ratio has been previously reported for GaAs material in conventional thin film growth.⁸ Here, we observed the sidewall thin-film growth mechanism for InP nanowire growth, which has a similar V/III ratio dependence as that shown in reference 8. The two tapered nanowire samples, D and E, appear to have slightly thinner tips than sample C. This might be due to the more Au-catalyst diffusion into the nanowires during the growth for the higher V/III ratio conditions.⁹ This phenomenon served as a secondary effect to make the nanowires more tapered. Between the straight nanowire sample C (V/III = 67) and the tapered nanowire sample D (V/III = 180), two more V/III ratios, 90 and 120, were tested. While the V/III = 90 nanowire sample still looks straight, the V/III = 120 sample begins to show some taperness. The onset of nanowire tapering is then deduced as between V/III = 90 and 120.

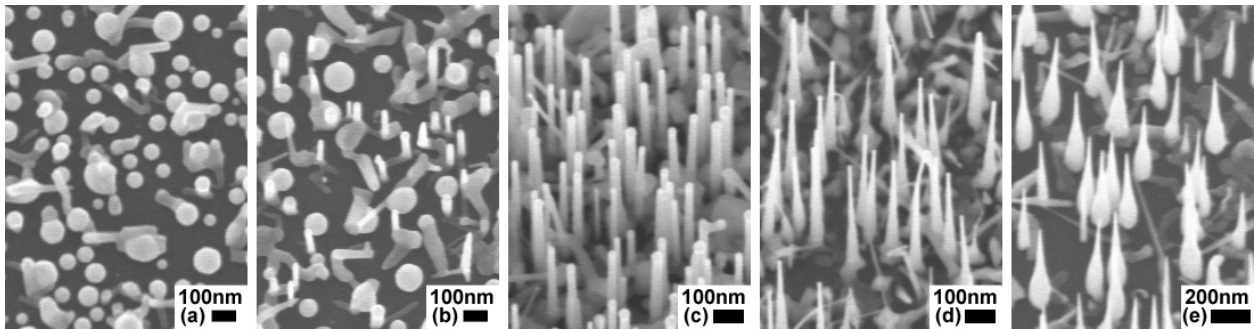


Figure 3.1 20°-tilt FE-SEM images for five InP nanowire/(111)Si samples, sample A, B, C, D and E, with V/III ratios equal to (a) 15 (b) 30 (c) 67 (d) 180 (e) 240, respectively. (a) and (b) represent an insufficient V/III ratio and hence indium-rich growth condition. (c) represents a growth condition for yielding non-tapered nanowires. (d) and (e) represent the high V/III ratio growth conditions which yield tapered-nanowires due to the stronger thin-film nanowire sidewall deposition.

3.2 InP Nanowire Optical Properties with Different V/III Ratios

Optical properties were characterized by micro-photoluminescence (μ -PL) measurements at both room temperature and at 4 K using a diode-pumped solid state laser at 532 nm focused to a ~ 1.5 μ m spot. Fig. 3.2 shows the 4 K μ -PL spectrum comparison for the five samples in Fig. 3.1. The emission wavelengths of sample A and B are expected to be very close to the bulk InP bandgap since there are very few nanowires on both samples but only some larger InP blobs, which might contribute to this PL emission. The PL peak of sample C with uniform nanowires shows a blueshift of 40 meV from the bulk InP bandgap due to quantum confinement.⁷ Single-wire peaks from the narrowest nanowires are visible on the high-energy side of the ensemble spectrum. For example, a peak with a 178 meV blueshift and linewidth of 1.4 meV was observed (see Fig. 3.2 inset), which is the narrowest linewidth reported for a III-V nanowire.¹⁰ Sample D has a similar PL blueshift as sample C. However, the spiky features at the high energy side are not observed

for sample D. This can be explained by the following. At low temperature, the carrier diffusion length is longer.¹¹ Hence, carriers originally generated at the tips of the very narrow nanowires can diffuse to the wider parts of the nanowires where they see less quantum confinement (smaller photon energy) and recombine there. For sample E, the carrier diffusion phenomenon is more pronounced for the strongly tapered nanowires. As a consequence, for sample E, not only have the spiky features disappeared, but the PL peak shifts significantly to the redder side of sample C, at 20 meV blueshift of the InP bulk bandgap.

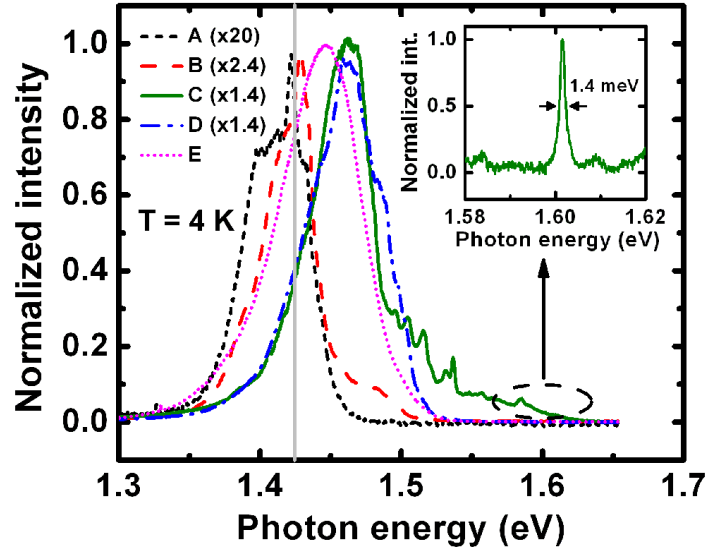


Figure 3.2 ($T = 4$ K) Representative μ -PL spectra for various V/III ratio growth conditions (sample A to E) with excitation power equal to $1.8 \mu\text{W}$. Gray line indicates the 4 K InP bulk bandgap (1.424 eV). Inset shows a single nanowire spectrum from a straight and narrow nanowire (from sample C, V/III = 67), with a FWHM of 1.4 meV and blueshift of 178 meV from the bulk bandgap. For sample C, the high-energy side of the spectrum is spiky due to the contribution of these individual thin and straight nanowires.

The room-temperature μ -PL spectra (Fig. 3.3) show significant differences from those at 4 K. First of all, the fine features are no longer visible for sample C. Secondly, sample E has the same PL peak energy and linewidth as samples C and D, instead of being 20 meV redder at 4 K. This is particularly interesting since the nanowire base is wider than 100 nm and emission at the bulk bandgap is expected. We attribute this observation to luminescence from the narrow nanowire tips, where at room temperature confined carriers recombine radiatively before being able to diffuse to the wider base region. Third, samples A to D all show an extra 60 meV blueshift from the bulk InP bandgap compared to the amount of blueshift at 4 K (see Fig. 3.2). The origin of this extra 60 meV blueshift is under further investigation.

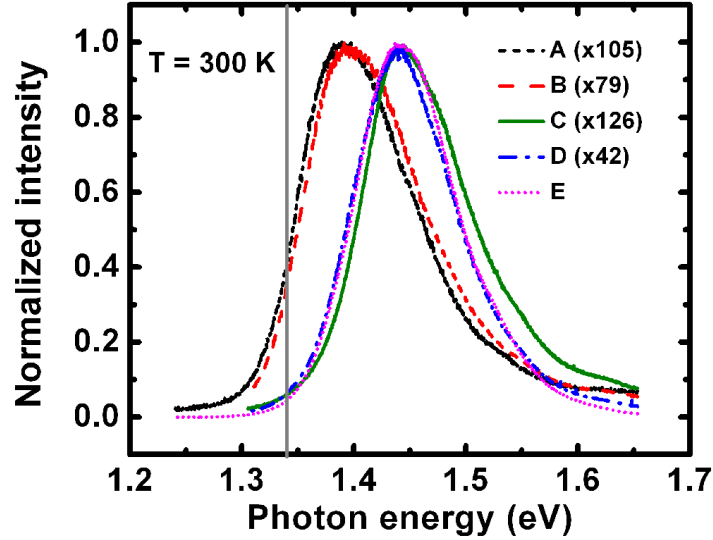


Figure 3.3 Room-temperature PL spectrum for the various V/III ratios with excitation power equal to 400 μ W. Gray line indicates room-temperature InP bulk bandgap (1.340 eV). All samples are blueshifted with respect to the bulk bandgap. No fine features are seen due to thermal broadening.

The PL intensities for both 4 K (Fig. 3.2) and room-temperature (Fig. 3.3) measurements increase with V/III ratio. A similar trend is observed for InP epilayers,^{12,13} where it has been shown that high V/III ratios result in epilayers with lower defect densities.^{13,14}

Fig. 3.4a shows the peak energy position as a function of the excitation power at 4 K. When the excitation power is swept from 600 nW to 1.6 mW, over a three-decade power increase, the straight (V/III = 67) and most tapered nanowires (V/III = 240) show a blueshift of 9 meV and 40 meV, respectively. The small power-dependent blueshift for the straight nanowires reflects the one-dimensional density of states nature of these nanowires. Wavelength stability over a large excitation power range is important for critical devices such as lasers. The large blueshift for the tapered nanowires is attributed to the effect of decreased carrier diffusion length at higher pumping, resulting in emission from the narrower part of the tapered nanowires.

The μ -PL peak intensity versus excitation power was also studied as shown in Fig. 3.4b. The higher V/III ratio, as described earlier, resulted in a larger PL peak intensity. For example, sample E is more than 10 times brighter than sample C at 1.6 mW excitation. This effect might be also due to the larger nanowire volume since higher V/III ratio increases the sidewall deposition rate. The PL peak intensity shows some saturation at higher excitation powers for sample C and D, while there is no saturation observed for E within this range, likely due to the nanowire volume difference. For example, the nanowire volume of sample E is estimated as $2.5 \times 10^{-15} \text{ cm}^3$ and the nanowire volume ratio between sample E and D is ~ 6 . The number of available electronic states is proportional to the volume which makes sample E remain unsaturated at higher pumping levels.

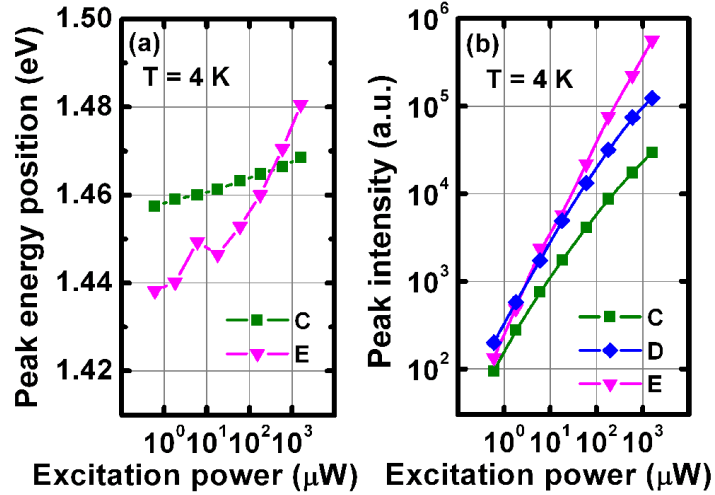


Figure 3.4 T = 4 K (a) μ -PL peak energy position versus excitation power for straight InP nanowires (sample C, V/III = 67) and strongly tapered InP nanowires (sample E, V/III = 240), respectively. Sample C shows a smaller wavelength dependence of only a 9 meV blueshift when excitation power is increased from 600 nW to 1.6 mW, while sample E shows a 40 meV blueshift. (b) μ -PL peak intensity vs. excitation power from 600 nW to 1.6 mW for various V/III ratios. The higher the V/III ratio, the larger the PL peak intensity is. Samples C and D show some intensity saturation at higher excitation powers while sample E does not.

In conclusion, we demonstrate the V/III ratio effects on both the shape and optical properties for InP nanowires grown on (111) Si substrates. The higher the V/III ratio is, the more tapered the nanowires become. The PL intensity increases dramatically with the V/III ratio. When the V/III ratio is optimized to 67, non-tapered InP nanowires were grown. These nanowires show a record narrow PL peak and weak excitation-power dependence, resembling features of ideal one-dimensional structures. In our experiments, non-tapered InP nanowires could be synthesized for V/III ratios ranging from 60-90 hence offering a reasonable growth window. We also showed that the PL peak intensity could be increased with the increase of V/III ratio.

Reference:

- (1) Razeghi, M. *The MOCVD Challenge, Volume 1: A Survey of GaInAsP-InP for Photonic and Electronic Applications* (Adam Hilger, Bristol and Philadelphia, 1989).
- (2) Mi, Z. *et al.* High performance self-organized InGaAs quantum dot lasers on silicon. *J. Vac. Sci. Technol. B* **24**, 1519-1522 (2006).
- (3) Balakrishnan, G., *et al.* Room-temperature optically pumped (Al)GaSb vertical-cavity surface-emitting laser monolithically grown on an Si(100) substrate. *IEEE J. Sel. Topics Quantum Electron.* **12**, 1636-1641 (2006).

- (4) Groenert, M. E. et al. Improved room-temperature continuous wave GaAs/AlGaAs and InGaAs/GaAs/AlGaAs lasers fabricated on Si substrates via relaxed graded $\text{Ge}_x\text{Si}_{1-x}$ buffer layers. *J. Vac. Sci. Technol. B* **21**, 1064-1069 (2003).
- (5) Fang, S. F. et al. Gallium arsenide and other compound semiconductors on silicon. *J. Appl. Phys.* **68**, R31-R58 (1990).
- (6) Lum, R. M. et al. Effects of misfit dislocations and thermally induced strain on the film properties of heteroepitaxial GaAs on Si. *J. Appl. Phys.* **64**, 6727-6732 (1988).
- (7) Chuang, L. C., Moewe, M., Chase, C., Kobayashi, N. P., and Chang-Hasnain, C. Critical diameter for III-V nanowires grown on lattice-mismatched substrates. *Appl. Phys. Lett.* **90**, 043115 (2007).
- (8) Kikkawa, T., Tanaka, H., & Komeno, J. The growth of GaAs, AlGaAs, and selectively doped AlGaAs/GaAs heterostructures by metalorganic vapor phase epitaxy using tertiarybutylarsine. *J. Appl. Phys.* **67**, 7576-7582 (1990)
- (9) Hannon, J. B., Kodambaka, S., Ross, F. M., & Tromp, R. M. The influence of the surface migration of gold on the growth of silicon nanowires. *Nature* **440**, 69-71 (2006).
- (10) van Weert, M. H. M. et al. Large redshift in photoluminescence of p-doped InP nanowires induced by Fermi-level pinning. *Appl. Phys. Lett.* **88**, 043109 (2006).
- (11) Sze, S. M. *Physics of Semiconductor Devices* (John Wiley & Sons, New York, 1981).
- (12) Kasemset, D., Hess, K. L., Mohammed, K., & Merz, J. L. The effects of V/III ratio and growth temperature on the electrical and optical properties of InP grown by low-pressure metalorganic chemical vapor deposition. *J. Electron. Mater.* **13**, 655-671 (1984).
- (13) Hsu, C. C., Yuan, J. S., Cohen, R. M., & Stringfellow, G. B. Doping studies for InP grown by organometallic vapor phase epitaxy. *J. Cryst. Growth* **74**, 535-542 (1986).
- (14) Keiper, D., Westphalen, R., & Landgren, G. Metal organic vapour-phase epitaxy (MOVPE) growth of InP and InGaAs using tertiarybutylarsine (TBA) and tertiarybutylphosphine (TBP) in N_2 ambient. *J. Cryst. Growth* **204**, 256-262 (1999).

Chapter 4:

GaAs-Based Nanoneedles Including InGaAs, AlGaAs and Quantum Wells

The VLS nanowire materials described in the previous two chapters are excellent materials to overcome the lattice mismatch and the growth temperature issue when being integrated with the Si-CMOS devices. However, when it comes to the integration at device level, there are generally two concerns. First, the introduction of the metal catalysts, especially Au, might be forming deep levels¹ for CMOS devices and hence largely deteriorating the CMOS device performances. Second, the volume of each single nanowire is too small hence nanowires might not be suitable for some applications when a larger output power is needed. The nanowire size limitation is particularly an issue for the integration of the highly lattice-mismatched nanowires on Si since the epitaxial nanowire diameters are limited to < 100 nm for lattice mismatches $> 4\%$.² The nanowire diameter for yielding single phase materials without defects such as twin boundaries is also limited to a small value, e.g., 60 nm for InP nanowires on Si.³

In this chapter, I will present a novel growth mode for synthesizing catalyst-free, sharp GaAs-based nanoneedle structures, with only a few atoms wide at the tip, and a sharp $6-9^\circ$ taper angle. Most importantly, these GaAs nanoneedles can be grown epitaxially onto substrates with a large lattice mismatch, such as Si and sapphire, with excellent structural (dislocation-free) and optical properties. A schematic of a typical GaAs nanoneedle is shown in Fig. 4.1a. Fig. 4.1b shows an SEM image of a GaAs nanoneedle grown on a c-plane sapphire substrate. These GaAs nanoneedles have a hexagonal cross-section and the sharp tip is only a few nanometers wide. The taper angle is $6-9^\circ$ for GaAs nanoneedles grown on Si and $10-12^\circ$ for GaAs nanoneedles on sapphire. The GaAs nanoneedle shown in Fig. 4.1b is with an 82-min growth time. The nanoneedle aspect ratio remains the same as growth time increases with the sharp tip feature maintained.

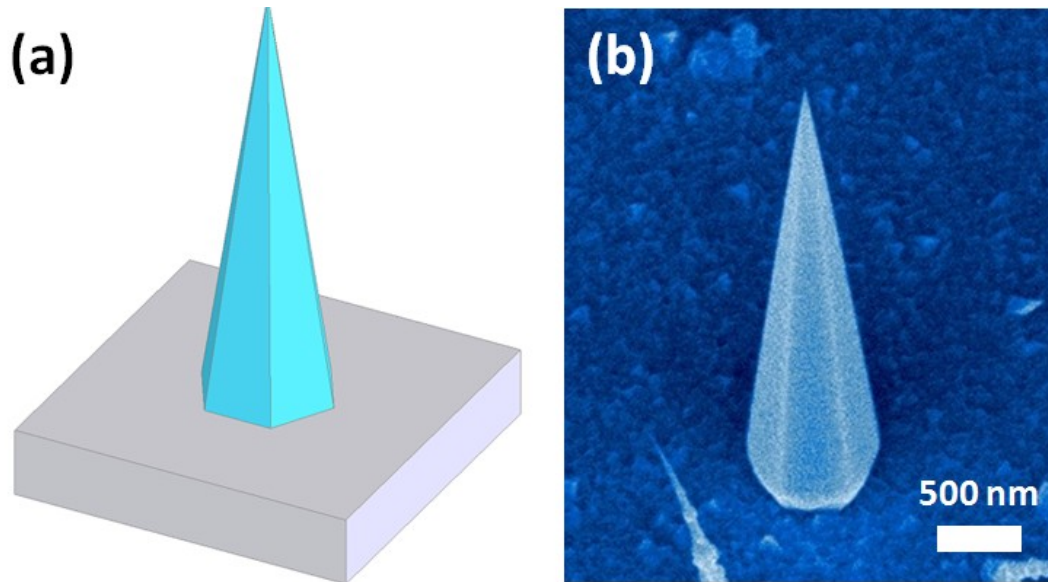


Figure 4.1 (a) Schematic of a typical nanoneedle with a hexagonal cross-section and a sharp tip. (b) SEM image of a GaAs nanoneedle grown on a c-plane sapphire substrate. The sharp nanoneedle tip is typically only a few nanometers wide. Despite the 46% lattice mismatch between GaAs and sapphire, the nanoneedle still grows epitaxially onto the substrate.

4.1 The Discovery of Nanoneedle Growth Mode

An early attempt for growing GaAs nanowires on a (100)GaAs substrate with Ge as the VLS catalyst resulted in GaAs nanoneedle growth at the area which was accidentally scratched. Later control experiments showed that the presence of Ge thin-film and the substrate surface scratch made with a stainless-steel tweezers are both needed to initiate the nanoneedle growth. Fig. 4.2a shows a GaAs nanoneedle growth on an intentional and controlled scratch line with a 2.5 nm Ge thin film pre-deposited on a (100) GaAs substrate. The growth temperature was 400°C. Fig. 4.2b is with the same substrate preparation steps but with a higher nanoneedle growth temperature of 430°C. The majority of the GaAs nanoneedles align very well to the $\langle 111 \rangle_B$ directions. The role of Ge thin film is believed not being the liquid-phase catalyst in the typical VLS growth mechanism since Ge is not seen at the nanoneedle tips.

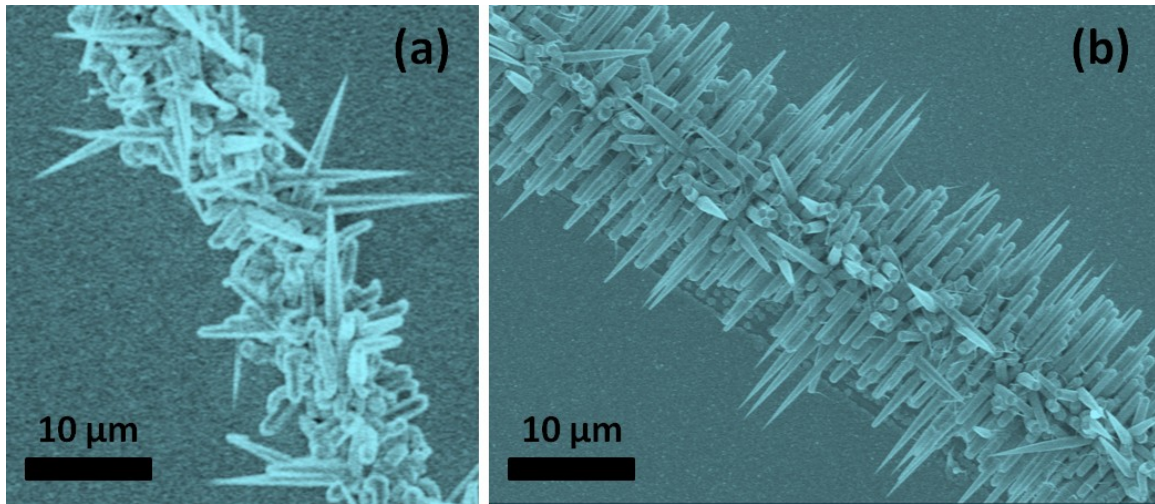


Figure 4.2 GaAs nanoneedles grown on (100)GaAs substrates with a 2.5 nm Ge thin film pre-deposited onto the substrate before the growth. A stainless-steel-tweezers scratch is needed to initiate the nanoneedle growth. (a) The growth temperature is 400°C. (b) The growth temperature is 430°C.

The necessity of both a Ge thin film and scratches for initiating the GaAs nanoneedle growth on a GaAs substrate led to the speculation that other types of surface treatment might also be able to nucleate the nanoneedle seeds. Since it is well known that lattice mismatch would prefer 3-dimensional growth such as the quantum dot growth via the Stranski–Krastanov growth mode or the Volmer-Weber growth mode, using lattice mismatch to initiate the nanoneedle growth was then attempted. For GaAs nanoneedles grown on a Si substrate, Ge thin film is not needed but the scratch is still necessary. This shows that the 4.1% lattice mismatch might take the role of the Ge thin film for the nanoneedle seed nucleation. Fig. 4.3a shows several GaAs nanoneedles epitaxially grown on a (111)Si with only scratch lines needed to induce the growth. Ge thin film is not needed probably due to the aid of the 4.1% lattice mismatch between GaAs and Si. Fig. 4.3b shows the zoomed-in view of a single nanoneedle showing very smooth sidewalls. The (111)Si used here was a 4°-offcut one hence from the top-down view in Fig. 4.3b the epitaxial GaAs nanoneedle is with a small tilt angle. These nanoneedles grow along the Si [111] direction. Details for the nanoneedle crystal structure and how it aligns on different substrates would be discussed shortly.

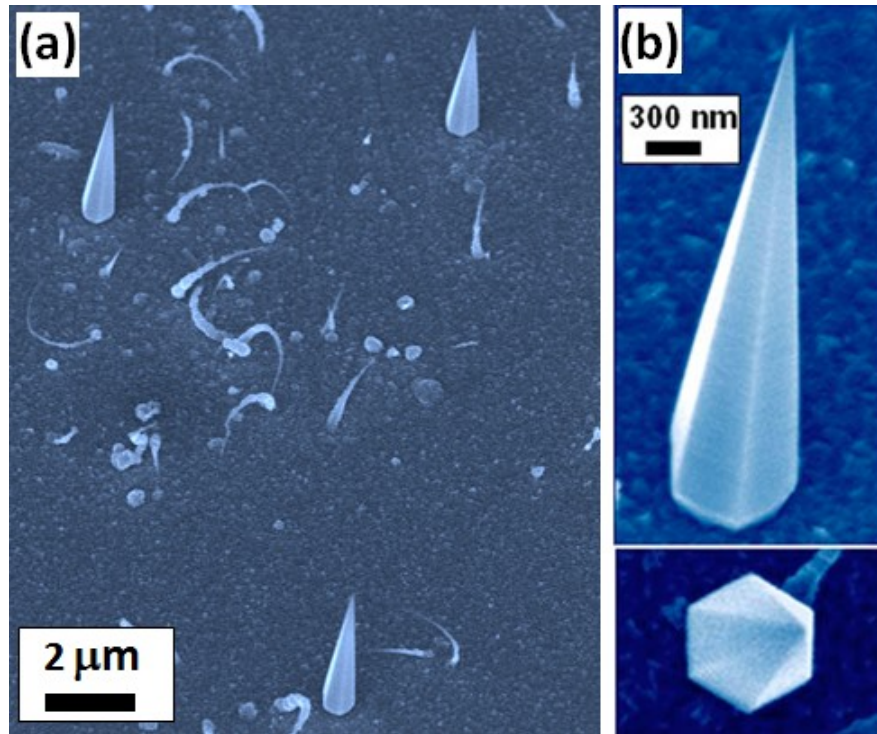


Figure 4.3 GaAs nanoneedles grown on a 4°-offcut (111)Si substrate. Ge thin film is not needed to initiate the nanoneedle growth probably due to the 4.1% lattice mismatch between GaAs and Si. However, scratch lines are still needed. (a) 30°-tilt SEM image of several epitaxial GaAs nanoneedles. (b) Zoomed-in view of a single nanoneedle. A top-down view is also shown. The growth temperature is 400°C.

With the success of eliminating the Ge thin film while still being able to initiate the nanoneedle growth for GaAs nanoneedles on Si with a 4.1% lattice mismatch, a sapphire substrate was tested which provided a very large lattice mismatch of 46% to GaAs. Fig. 4.4 shows GaAs nanoneedles spontaneously grew on a c-plane sapphire substrate without any surface treatment. The successful nucleation of the GaAs nanoneedle seeds is attributed to the large 46% lattice mismatch. The GaAs nanoneedles are still seen epitaxially grown onto the sapphire substrate despite the large 46% lattice mismatch. Detailed discussions for GaAs nanoneedles grown on sapphire will be presented in Chapter 7.

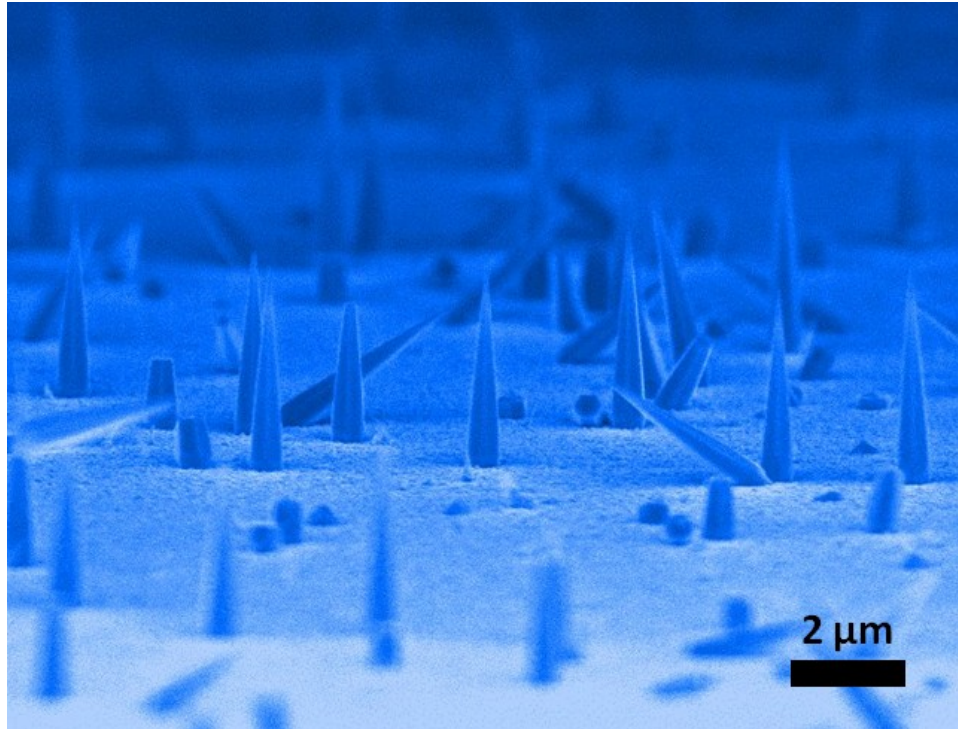


Figure 4.4 GaAs nanoneedles spontaneously grown on a c-plane sapphire substrate. No surface treatment is needed to initiate the nanoneedle seed nucleation. This is attributed to the 46% lattice mismatch between sapphire and GaAs.

4.2 GaAs Nanoneedle Growth Details

The nanoneedles grow on GaAs, silicon and sapphire substrates under the same growth conditions, resulting in similar nanoneedle dimensions and optical properties. However, the substrate preparation is very substrate-dependent as described earlier.

The growth on a GaAs substrate begins with cleaning the substrate with a standard 3-step process in the sequence of acetone, methanol and de-ionized water for 3 minutes each. The GaAs wafer is then chemically deoxidized in a 10:1 diluted HCl solution for 3 min, or until the surface becomes hydrophobic. The wafer is then immediately transferred into an e-beam evaporator for depositing a Ge thin film. The typical Ge film thickness is 2.5 nm. However, it has been tested that Ge films with thickness down to ~0.6 nm could still initiate the nanoneedle growth. After the Ge deposition, the wafer is then scratched with a stainless-steel tweezers on a home-made scratching stage. After the scratch the wafer is immediately transferred into the loadlock chamber of an MOCVD system to minimize the oxidation. GaAs nanoneedles are grown with an EMCORE D75 MOCVD system. The wafer is first annealed at 606°C for 3 minutes, which is meant to thermally dioxide the surface if there is any oxide residual. The GaAs nanoneedle growth itself is conducted typically at 400°C. Triethylgallium (TEGa) and tertiarybutylarsine (TBA) are the sources. TEGa and TBA are chosen for their relatively low decomposition temperatures (300 °C and 380 °C, respectively).^{4,5} These low decomposition temperatures are

suitable for the low-temperature GaAs nanoneedle growth. Typical TEGa and TBA mole fractions are 1.12×10^{-5} and 5.42×10^{-4} , respectively, in a 12 l/min hydrogen carrier gas flow. Therefore the typical V/III ratio is 48. TBA is introduced to the reactor whenever the reactor temperature is higher than 200°C to protect the substrate surface. The platter which holds the substrate spins at 1400 rpm at a pressure of 76 Torr during the growth.

For (111)Si substrates, the wafer cleaning process is the same. The deoxidation process is done through a 3-min 5:1 buffered oxide etch. The silicon-oxide-free surface can be checked with the substrate hydrophobicity. After the deoxidation the Si wafer is then scratched and then transferred into the MOCVD loadlock chamber, which is pumped down to $\sim 10^{-6}$ Torr to avoid further oxidation. The growth procedure is the same as that for a GaAs substrate. TBA is still introduced into the reactor for temperatures higher than 200°C to keep the growth recipes the same for better comparison. Similarly, the 3-min 606°C pre-growth annealing is still kept.

For sapphire substrate, the cleaning procedure is still identical with a 3-step acetone, methanol and de-ionized water rinse. There is no deoxidation process for a sapphire substrate since sapphire itself is single-crystal aluminum oxide. The growth recipe for GaAs nanoneedles on sapphire is the same as that for a GaAs or a Si substrate.

4.3 GaAs Nanoneedle Structural Properties

When the nanoneedle density is high, sometimes it is observed that two nanoneedles cross each other. Fig. 4.5a shows GaAs nanoneedles grown on a (100)GaAs substrate. The epitaxial nanoneedles grow along the $\langle 111 \rangle_B$ directions and two nanoneedles happen to cross each other. This shows that the nanoneedle growth mode is core-shell. An schematic of the nanoneedle core-shell growth mode is shown in Fig. 4.5b.

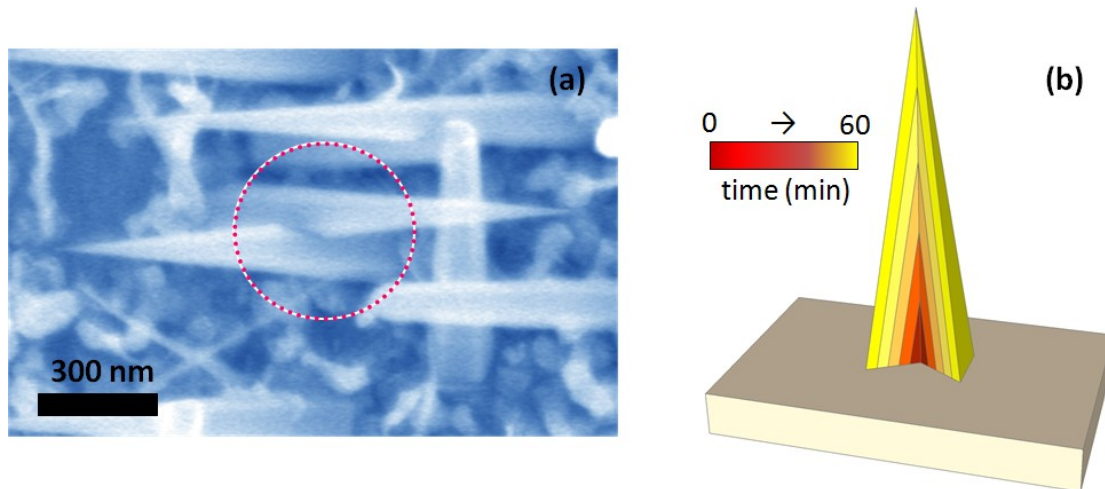


Figure 4.5 (a) GaAs nanoneedles grown on a (100)GaAs substrate. Two nanoneedles are seen crossing over each other indicating the core-shell nanoneedle growth mode. (b) Schematic of the nanoneedle core-shell growth mode.

The growth direction of the GaAs nanoneedles is analyzed as follows. For GaAs nanoneedles grown on a (111)B GaAs substrate, nanoneedles are found grown in parallel to the surface normal, which is the $[111]_B$ direction, as shown in Fig. 4.6.

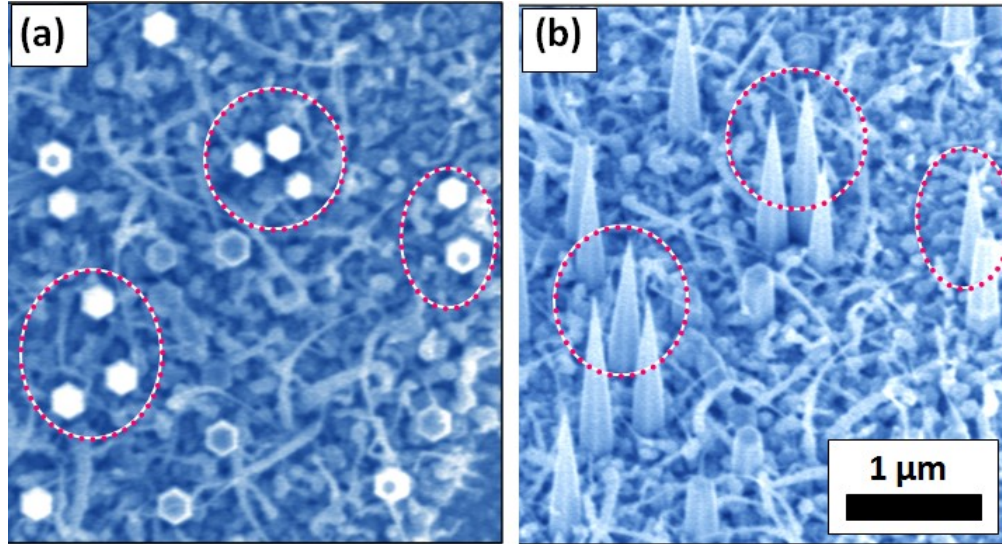


Figure 4.6 (a) Top-down SEM image of GaAs nanoneedles grown on a (111)B GaAs substrate. Nanoneedles are epitaxially grown along the $[111]_B$ GaAs substrate direction. (b) 30°-tilt view of the same area showing that the all-white hexagons in (a) represent sharp nanoneedles while the one with a dark central dot represents a flat-top nanoneedle.

The crystal structure of the GaAs nanoneedle grown on (111)B GaAs is investigated via TEM. The as-grown nanoneedles were first wiped onto a carbon film and then placed under a TEM for observation. Fig. 4.7a shows a high-resolution TEM (HRTEM) image of a nanoneedle tip with only ~ 5 nm in diameter. There is no dislocation seen near the nanoneedle tip. Fig. 4b is the low-resolution TEM image of the same nanoneedle. The Fast Fourier Transform (FFT) pattern of Fig. 4.7a is shown in Fig. 4.7c for further analysis. The zone axis is identified as $[1\bar{1}00]$. The nanoneedle is surprisingly seen with a pure wurtzite (WZ) phase, which is very different from the common zinc-blende (ZB) phase seen for typical bulk GaAs. Bulk WZ GaAs has only been previously reported in powder form and is fabricated through a high pressure (~ 14 GPa) treatment.⁶ Thin vapor-liquid-solid GaAs nanowires with 30-60 nm in diameter are also reported with WZ crystalline structure.⁷ The MOCVD GaAs nanoneedle growth mode reported here is the only known method of synthesizing epitaxial WZ GaAs of bulk size at typical crystal growth temperature and pressure. The WZ GaAs nanoneedle grows along the $[0001]$ direction, i.e., c-axis, as can be seen from the FFT pattern. The nanoneedle under observation was with one of its 6 sidewall facets in contact with the carbon film, as verified independently by SEM. The orientation of the nanoneedle on carbon film is schematically shown in Fig. 4.7b. This means the zone axis, $[1\bar{1}00]$, is nearly in parallel to the surface normal of the sidewall facets, except that there is a small angle (half of the nanoneedle taper angle) between them. The nanoneedle sidewall is actually made of $\{1\bar{1}00\}$ and (0001) terraces as details will be shown in Chapter 7.

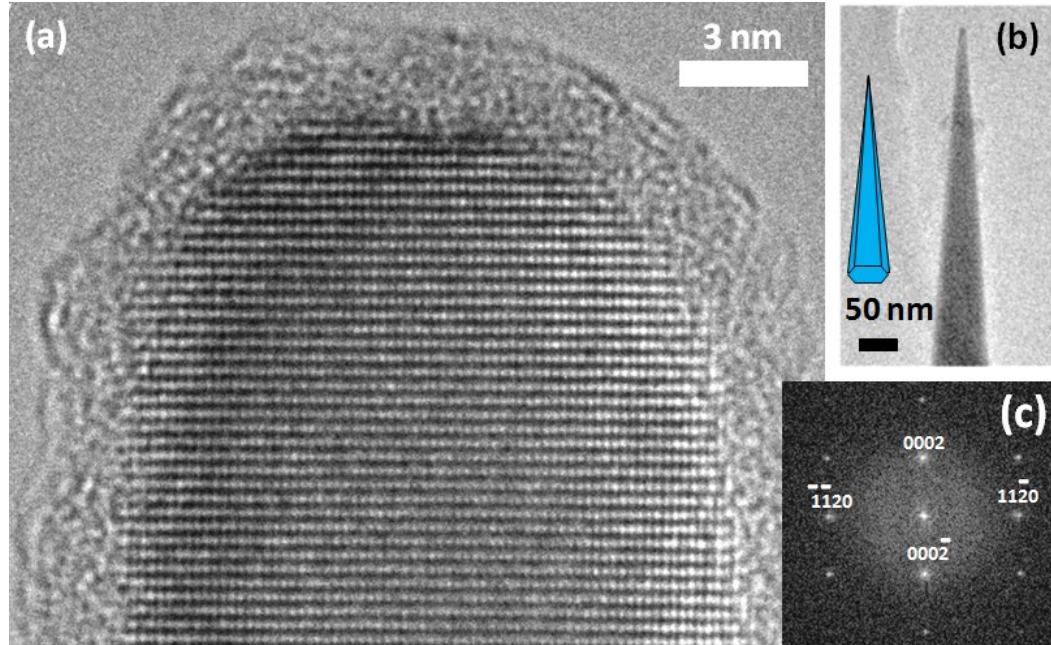


Figure 4.7 (a) HRTEM of a GaAs nanoneedle wiped from the as-grown (111)B GaAs substrate. The tip is only ~5nm in diameter. No dislocation is seen. (b) Low-resolution TEM image of the same nanoneedle. Inset shows the facet orientation of this nanoneedle as independently identified by SEM. (c) FFT pattern of the image shown in (a). Zone axis is $[1\bar{1}00]$. The GaAs nanoneedle is with WZ phase and grows along the $[0001]$ direction. The taper sidewall is made of $\{1\bar{1}00\}$ and (0001) terraces.

The GaAs nanoneedle is labeled as a WZ structure through Fig. 4.7c. However, the diffraction pattern shown in Fig. 4.7c is not unique to WZ. It can be labeled with ZB $[2\bar{1}\bar{1}]$ zone axis as well. In order to unambiguously identify the WZ structure of a nanoneedle, another zone axis has to be checked. Fig. 4.8a is a HRTEM image of another sharp nanoneedle. This ultra-sharp nanoneedle has only three lattice spacing on its tip and is the sharpest semiconductor material which has ever been reported. This nanoneedle is with the jointed edge of two adjacent sidewalls facing the electron beam of the TEM as schematically shown in Fig. 4.8b, which also shows a low-resolution image. Comparing this nanoneedle orientation with that shown in Fig. 4.7b, the current nanoneedle is rotated by 30° with respect to the $[0001]$ nanoneedle axis. As a consequence, the FFT of the current nanoneedle should show a zone axis of $[1\bar{2}10]$, if the nanoneedle is with WZ structure. The expected $[1\bar{2}10]$ zone axis indeed shows up as Fig. 4.8c. If the nanoneedle were with ZB structure, this 30° rotation would bring up the ZB $[1\bar{1}0]$ zone-axis diffraction pattern, which would be completely different from what is shown in Fig. 4.8c. As a consequence, GaAs nanoneedles are unambiguously identified with WZ crystal structure.

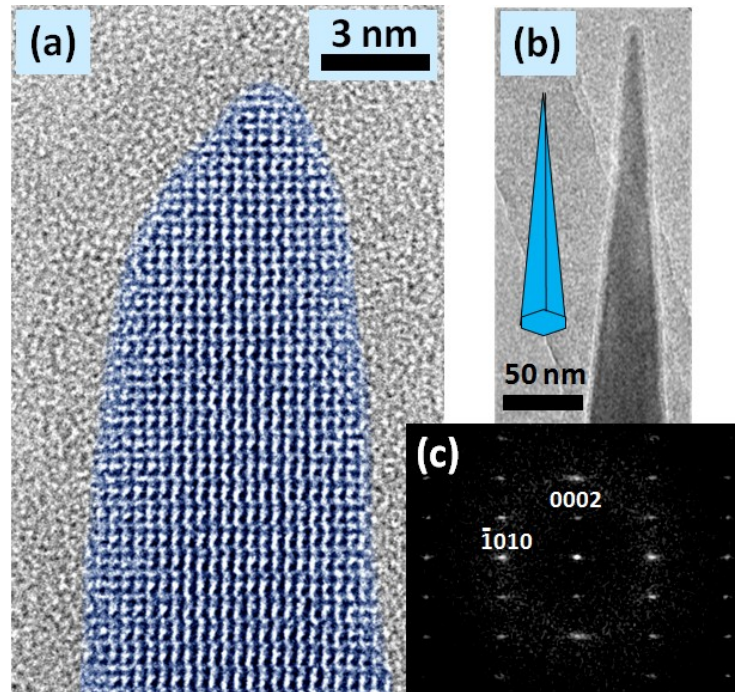


Figure 4.8 (a) HRTEM of a GaAs nanoneedle wiped from the as-grown (111)B GaAs substrate. The tip has only 3 lattice spacing in diameter. Again no dislocation is seen. (b) Low-resolution TEM image of the same nanoneedle. Inset shows the facet orientation of this nanoneedle as independently identified by SEM. (c) FFT pattern with an zone axis of $[1\bar{2}10]$. The GaAs nanoneedle is then unambiguously identified with WZ phase. The $[0001]$ nanoneedle growth direction is also seen here.

GaAs nanoneedles grown on a (111)Si substrate was also analyzed in a similar way under TEM. GaAs nanoneedles on Si are also found with WZ crystal structure, $[0001]$ growth direction, $\{1\bar{1}00\}$ and (0001) sidewall terraces. Fig. 4.9 is the TEM analysis of such a GaAs nanoneedle. The structural property of a GaAs grown on Si is identical to that grown on a (111)B GaAs substrate.

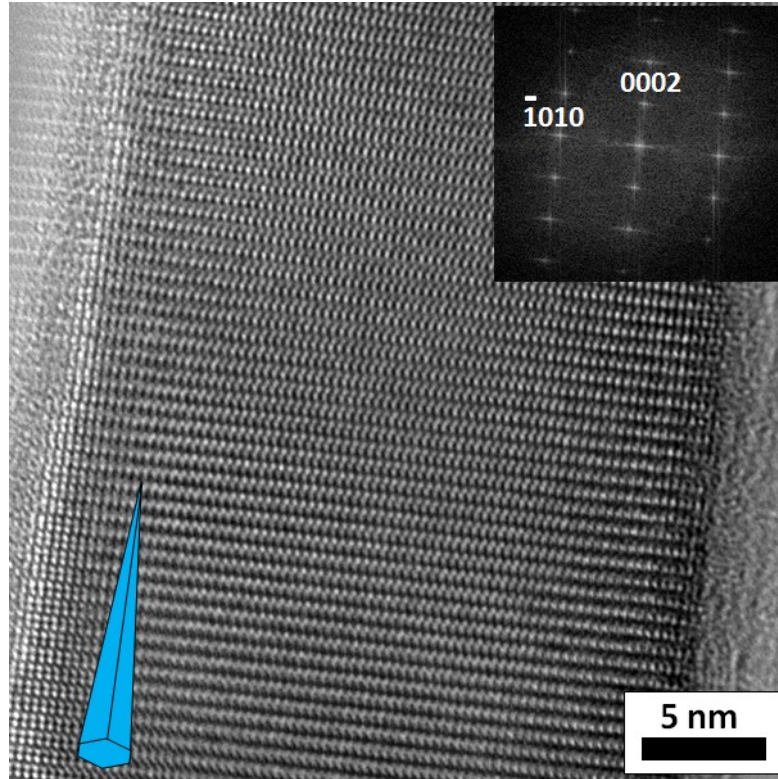


Figure 4.9 HRTEM of a GaAs nanoneedle wiped from a (111) Si substrate. Inset shows the facet orientation of this nanoneedle. Inset also shows the FFT pattern with a zone axis of $[1\bar{2}10]$. The GaAs nanoneedle is identified with WZ phase with $[0001]$ growth direction.

The alignment of an epitaxial GaAs nanoneedle to a (111)Si substrate can be seen from Fig. 4.3. The GaAs nanoneedle $[0001]$ direction is parallel to the Si $[111]$ direction. Comparing The TEM analyses from Fig. 4.7, 4.8 and 4.9 to Fig. 4.6, with the recognition of the substrate orientation, it is now possible to show the exact alignment of an epitaxial WZ GaAs nanoneedle grown on a cubic template, such as a ZB (111)B GaAs or a diamond (111)Si. Fig. 4.10 illustrates this alignment. The alignment between a GaAs nanoneedle and a cubic substrate is growth axis $\langle 0001 \rangle // \langle 111 \rangle$, sidewall $\langle 1\bar{1}00 \rangle // \langle 2\bar{1}\bar{1} \rangle$ and nanoneedle corner $\langle 11\bar{2}0 \rangle // \langle 01\bar{1} \rangle$.

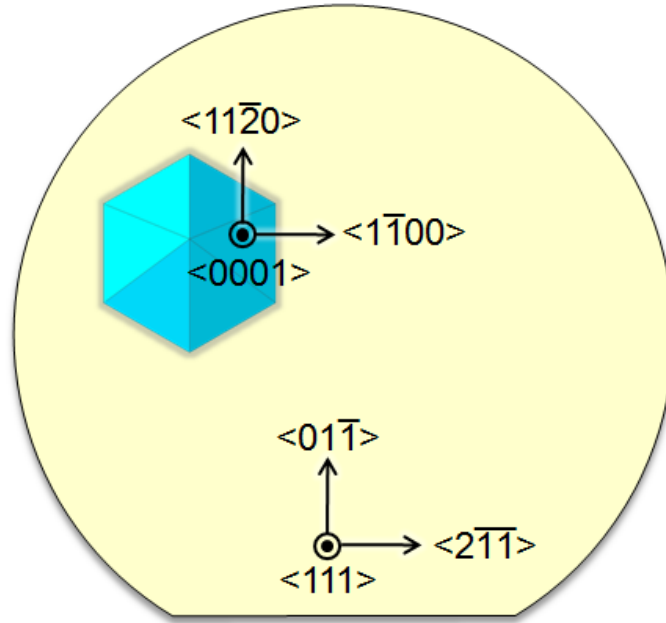


Figure 4.10 Schematic showing the alignment of a WZ GaAs nanoneedle to a cubic template, such as a (111)B GaAs substrate or a (111)Si substrate.

GaAs nanoneedles grown on a c-plane sapphire substrate was also analyzed by TEM and showed the identical structural properties as those of a GaAs nanoneedle on GaAs or Si. The GaAs nanoneedle on sapphire naturally aligns its [0001] growth axis to the [0001] direction of the sapphire substrate. The in-plane alignment and other properties are particularly interesting and will be further discussed later in Chapter 7. Such a system is with a 46% lattice mismatch, an extreme condition while the growth result is still excellent.

4.4 GaAs Nanoneedle Optical Properties

GaAs nanoneedles grown on a (111)Si substrate was measured with a micro-photoluminescence (μ -PL) setup at both 4 K and room temperature. The 532 nm excitation source was focused down to $\sim 1.5 \mu\text{m}$ in diameter to excite a single nanoneedle at a time. The 4 K PL spectra with various excitation powers are shown in Fig. 4.11a. Two peaks are seen with one at 1.509 eV and one at 1.521 eV. At higher excitation power, the 1.521 eV peak dominates and the 1.509 eV peak starts to saturate a little bit. As a consequence, the 1.521 eV peak is assigned to the free-exciton recombination in a WZ GaAs nanoneedle. The 1.509 eV peak is then temporarily assigned as the impurity-related emission since it starts to saturate for higher excitations. A more detailed analysis of the peak assignment will be given in Chapter 7. The position of the two peaks were resolved by fitting the PL spectra with two Lorentzian functions and a fitting example for the lowest excitation level, 10 μW , is shown in Fig. 4.11b. The free-exciton peak at 1.521 eV is with a narrow linewidth of only 20 meV. It is comparable to the 23 meV reported by Titova *et al.* for AlGaAs-passivated WZ GaAs nanowires on a GaAs substrate.⁸ The narrow linewidth indicates

good crystal quality. The free-exciton energy of 1.521 eV is ~ 6 meV larger than that of the ZB GaAs, which is at 1.515 eV.⁹ The ~ 6 meV larger WZ GaAs free-exciton energy agrees very well to the 7 meV reported by Martelli *et al.* from a WZ GaAs nanowire measurement.¹⁰ The energy difference between the two PL peaks shown in Fig. 4.11b is 12 meV. We previously tentatively assign the 1.509 eV emission as an impurity-related one according to its power dependence. The actual type of the impurity and the transition details still need further investigation. Carbon is suspected since it is a common residual impurity for MOCVD-grown materials.¹¹ The closest carbon peak to the free-exciton peak is the free electron to neutral carbon recombination, which is 22 meV away, for ZB GaAs.¹² The smaller 12 meV difference seen in WZ GaAs nanoneedles might be still from carbon but due to the carbon binding energy difference between ZB and WZ GaAs materials.¹³

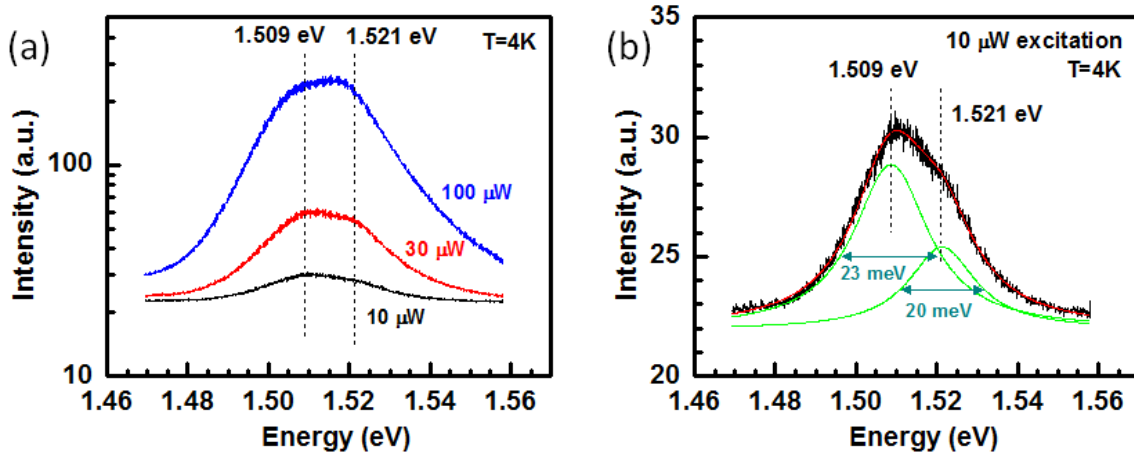


Figure 4.11 4K μ -PL analysis for a GaAs nanoneedle grown on (111)Si. (a) PL spectra for various excitation powers. Two peaks are seen. The 1.521 eV peak is assigned to the free-exciton emission while the 1.509 eV is tentatively assigned as the impurity related emission. (b) A fitting example with two Lorentzian functions for determining the two peak positions. The free-exciton peak at 1.521 eV has a narrow linewidth of 20 meV indicating good crystal quality.

Room-temperature PL spectra are shown in Fig. 4.12. Only one peak is seen and it is assigned as the bandedge emission. The large thermal energy kT of ~ 25 meV washes out the impurity-related fine features. The peak redshifts as the excitation power increases due to the thermal effect. The peak energy of the 100 μ W excitation spectrum is 1.435 eV. This is 11 meV larger than the ZB GaAs bandgap energy of 1.424 eV. This is similar to the WZ-to-ZB bandgap difference determined at 4 K.

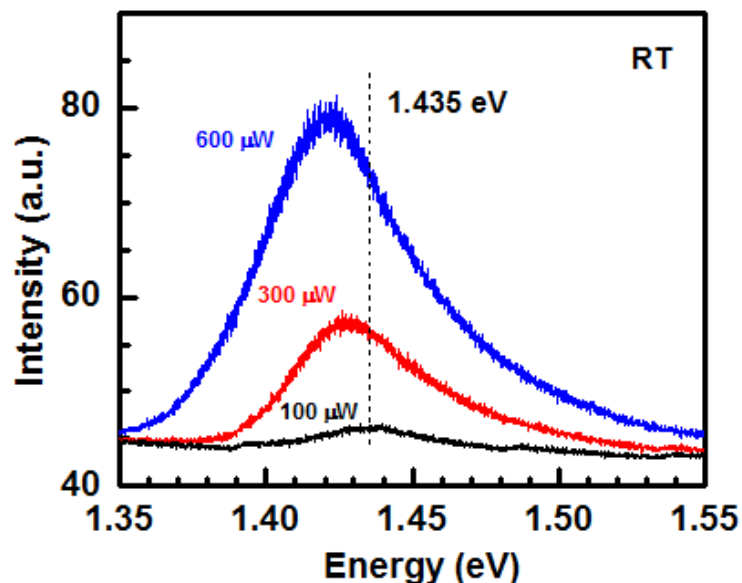


Figure 4.12 Room-temperature μ -PL spectra for a GaAs nanoneedle grown on (111)Si. The 1.435 eV peak is assigned to the bandedge emission. The room-temperature WZ GaAs bandgap is hence estimated here as 11 meV larger than that of ZB GaAs.

4.5 InGaAs Nanoneedle and InGaAs/GaAs Quantum Wells

Trimethylindium (TMIn) is used in addition to the TEGa and TBA sources to grow InGaAs nanoneedles. All the other growth conditions remain the same. The InGaAs nanoneedles are still grown at a low temperature of 400°C. Fig. 4.13 shows InGaAs nanoneedles grown on (111)Si with different indium compositions. Fig. 4.13a is just a pure GaAs nanoneedle. The different indium composition in InGaAs nanoneedles were achieved with different TMIn flow rate. The composition is determined by the PL peak position using the ZB InGaAs bandgap equation.¹⁴ From Fig. 4.13 it is seen that the $\text{In}_{0.05}\text{Ga}_{0.95}\text{As}$ (Fig. 4.13b) has the same aspect ratio, hence the same taper angle, as that of the pure GaAs nanoneedle in Fig. 4.13a. However, the $\text{In}_{0.15}\text{Ga}_{0.85}\text{As}$ nanoneedle (Fig. 4.13c) starts to show a larger taper angle. The tip sharpness, nevertheless, is still maintained for the up to 15% indium composition as shown here.

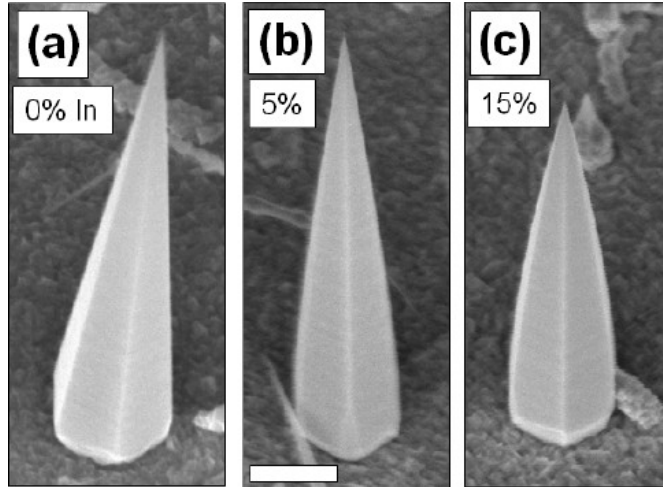


Figure 4.13 30°-tilt SEM images for a (a) GaAs, (b) $\text{In}_{0.05}\text{Ga}_{0.95}\text{As}$ and (c) $\text{In}_{0.15}\text{Ga}_{0.85}\text{As}$ nanoneedle on (111)Si. The 15% InGaAs nanoneedle shows a little larger taper angle than the pure GaAs nanoneedle and the 5% InGaAs nanoneedle. The sharp tip feature is still maintained for InGaAs nanoneedles up to 15% indium composition.

The 4 K μ -PL spectra for the three samples shown in Fig. 4.13 are shown below in Fig. 4.14. The PL linewidths broadened only slightly by 2x from the 30 meV of a pure GaAs nanoneedle to the 60 meV of a $\text{In}_{0.15}\text{Ga}_{0.85}\text{As}$ nanoneedle. This indicates that the crystal quality is maintained with the addition of indium. The PL intensity is also comparable. The indium composition is estimated from this PL measurement.

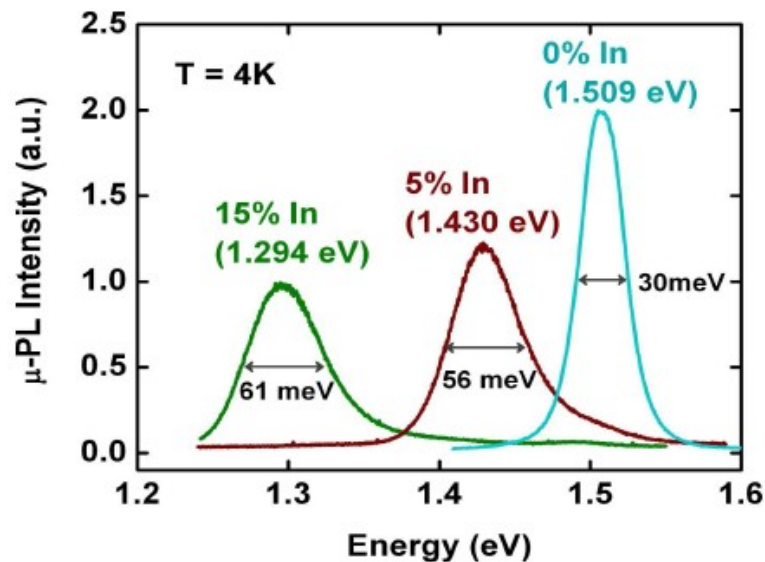


Figure 4.14 4 K spectra of the GaAs and InGaAs nanoneedles. The indium composition is estimated from the PL peak energy as 5% and 15% for the nanoneedles shown in Fig. 4.13b and 4.13c, respectively. The PL linewidth only slightly broadens $\sim 2x$ from 30 meV for a GaAs nanoneedle to 61 meV for an $\text{In}_{0.15}\text{Ga}_{0.85}\text{As}$ nanoneedle indicating the crystal quality is maintained even with the addition of the 15% indium. The PL intensity is also comparable.

With the capability of growing GaAs and InGaAs nanoneedles, InGaAs/GaAs quantum wells (QWs) in a nanoneedle was then attempted since QW laser structures are known with a reduced threshold current density and improved temperature stability.¹⁵ The nanoneedle quantum well structure is shown in Fig. 4.15a. The growth starts with a 60-min growth of a pure GaAs core (~600 nm in diameter) followed by a 1-3 minute growth of a single In_{0.15}Ga_{0.85}As QW. Finally a 10-min (~50 nm thick) GaAs barrier/cap is deposited on the In_{0.15}Ga_{0.85}As QW to complete the growth. Fig. 4.15b shows the 4 K PL spectra of several In_{0.15}Ga_{0.85}As/GaAs QW nanoneedles with different QW thicknesses. Starting from the bulk GaAs nanoneedle, only one peak is seen. The 5 nm QW nanoneedle sample starts to show blueshift. However, since the QW is thin, carriers overspill to the GaAs barrier hence a PL peak at the GaAs peak position is also seen for this sample. With the QW thickness increased to 10 and 15 nm, the main PL peak further redshifts since less quantum confinement is expected for these wider QW structures. The PL spectrum from a bulk In_{0.15}Ga_{0.85}As nanoneedle is also shown in Fig. 4.15b for comparison. Since there is no quantum confinement, the peak position at 1.294 eV is hence redder than any of the QW samples. This shows that the emission peak energy of an InGaAs/GaAs QW nanoneedle can be tuned and controlled very well by the QW thickness. This also implies an abrupt InGaAs/GaAs interface.

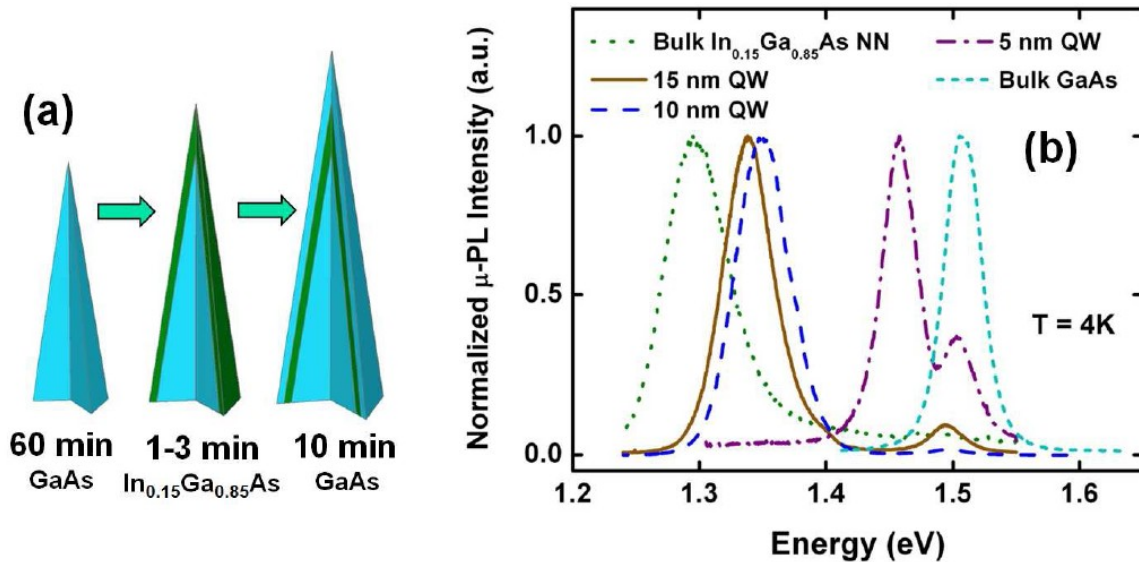


Figure 4.15 (a) Growth sequence for synthesizing InGaAs/GaAs single QW nanoneedles. (b) 4 K PL spectra for several In_{0.15}Ga_{0.85}As/GaAs QW nanoneedles with different QW thicknesses from 5 nm to 15 nm. The PL spectra of a pure GaAs nanoneedle and a pure In_{0.15}Ga_{0.85}As nanoneedle are shown for comparison. QW PL peak energy has a good correspondence to the designed QW thickness.

With the success of growing bulk InGaAs and InGaAs/GaAs QW structures with 15% indium, higher indium composition was further attempted. However, the attempted In_{0.3}Ga_{0.7}As growth on a (111)Si resulted in no sharp nanoneedle at all. Fig. 4.16 shows the typical SEM images from this In_{0.3}Ga_{0.7}As nanoneedle sample. All the nanoneedles are with a flat top. It is clearly seen that the 30% indium affected the nanoneedle growth. Current assumption is that the

high indium composition perturbs the nanoneedle growth mode and form defects/stacking faults at the tip of an originally sharp nanoneedle. Once this defect/stacking fault is present, vertical growth cannot continue hence a flat-top nanoneedle is formed. The flat-top size, however, varies largely from nanoneedle to nanoneedle. Some nanoneedles can have a very small flat top surface. This indicates that the perturbation happens in a random fashion therefore for a very short growth time, defect-free $\text{In}_{0.3}\text{Ga}_{0.7}\text{As}$ could still be grown.

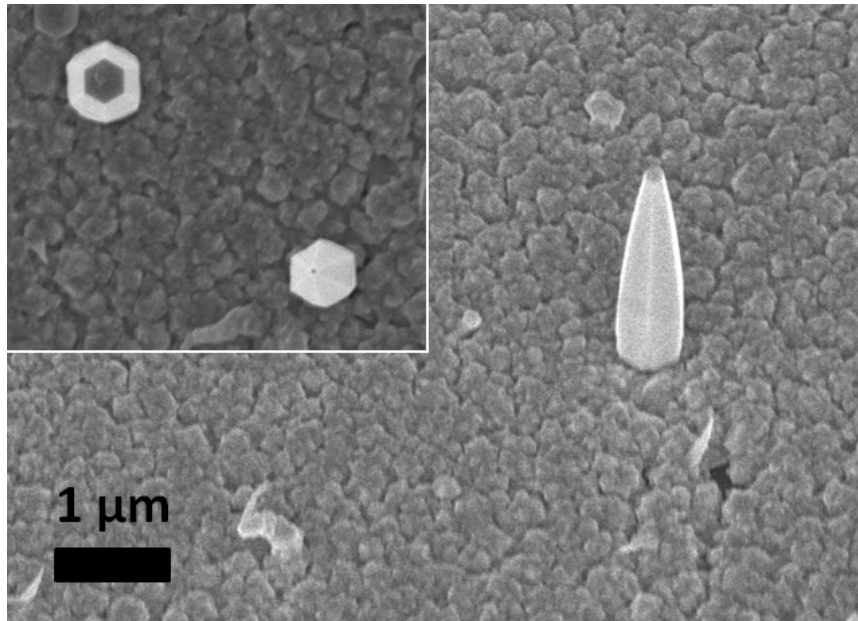


Figure 4.16 Top-down and 30°-tilt SEM images of an $\text{In}_{0.3}\text{Ga}_{0.7}\text{As}$ nanoneedle on (111)Si sample. No sharp nanoneedle is seen for this sample indicating that the 30% indium composition perturbs the sharp nanoneedle growth mode. The flat-top size, however, varies largely from nanoneedle to nanoneedle.

A 10 nm-thick $\text{In}_{0.3}\text{Ga}_{0.7}\text{As}/\text{GaAs}$ QW nanoneedle structure similar to that shown in Fig. 4.15a was grown and showed satisfactory optical properties. Fig. 4.17 compares the 4 K PL spectrum of this $\text{In}_{0.3}\text{Ga}_{0.7}\text{As}/\text{GaAs}$ QW nanoneedle sample to that of an $\text{In}_{0.15}\text{Ga}_{0.85}\text{As}/\text{GaAs}$ QW nanoneedle. The PL emission of the 30% indium InGaAs QW sample further redshifts to 1.119 eV. Such a peak energy is even transparent in Si hence this $\text{In}_{0.3}\text{Ga}_{0.7}\text{As}/\text{GaAs}$ QW nanoneedles structure is a potential light emitter for Si photonics applications since it can be grown onto as-fabricated Si CMOS devices at a low growth temperature of 400°C while still having excellent optical properties. The narrow PL linewidth for the $\text{In}_{0.3}\text{Ga}_{0.7}\text{As}/\text{GaAs}$ QW is also an indicator of the good crystal quality.

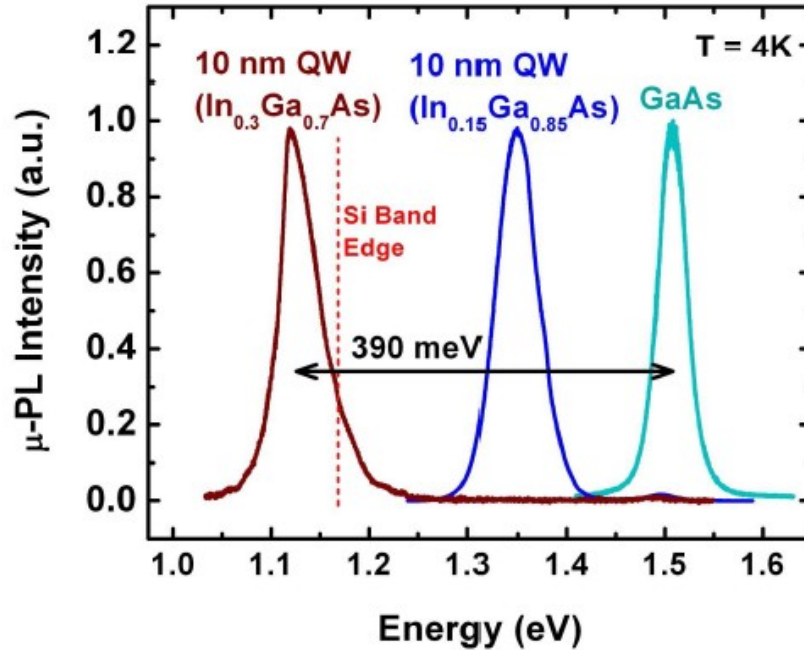


Figure 4.17 4 K PL spectra for a 10 nm-thick $\text{In}_{0.3}\text{Ga}_{0.7}\text{As}/\text{GaAs}$ QW nanoneedle and that for a similar $\text{In}_{0.15}\text{Ga}_{0.85}\text{As}/\text{GaAs}$ QW nanoneedle. The PL peak position for the $\text{In}_{0.3}\text{Ga}_{0.7}\text{As}/\text{GaAs}$ QW is already transparent in Si. The PL linewidth is still comparable to that of the $\text{In}_{0.15}\text{Ga}_{0.85}\text{As}/\text{GaAs}$ QW and the pure GaAs nanoneedle.

The fact that 30% indium composition affecting the nanoneedle vertical growth seen in the $\text{In}_{0.3}\text{Ga}_{0.7}\text{As}$ nanoneedle growth can actually be utilized to grow a “pancake” like structure with the capability of tuning the pancake diameter and height independently. Fig. 4.18a illustrates such an idea. The growth starts with a small pure GaAs nanoneedle core, therefore the tip is extremely sharp. $\text{In}_{0.3}\text{Ga}_{0.7}\text{As}$ is then introduced after the GaAs core to stop the vertical growth. All the subsequent $\text{In}_{0.3}\text{Ga}_{0.7}\text{As}$ growth will then only be in the lateral direction with very minimum deposition on the top flat surface. As a consequence, a pancake-shape structure can be grown. The height of the structure is determined by the growth time of the sharp GaAs core while the diameter of the pancake is determined by the $\text{In}_{0.3}\text{Ga}_{0.7}\text{As}$ growth time. Fig. 4.18b shows a pancake grown on a c-plane sapphire substrate with a 5-min sharp GaAs core growth followed by a 55-min $\text{In}_{0.3}\text{Ga}_{0.7}\text{As}$ growth. This pancake-shape structure can be designed to support some cavity modes such as the whispering gallery mode.¹⁶

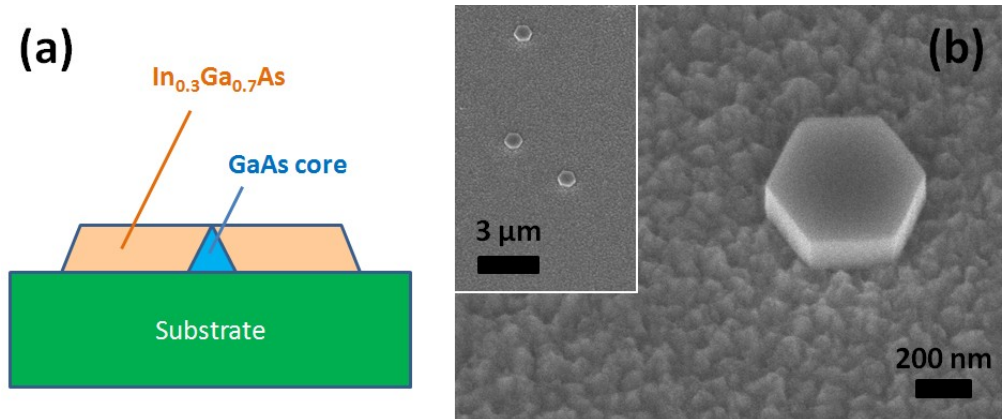


Figure 4.18 “Pancake” growth mode utilizing the sharp GaAs and flat In_{0.3}Ga_{0.7}As nanoneedle growth mode. (a) Schematic showing the growth sequence of a pancake. A small GaAs nanoneedle core is first grown. The GaAs core determines the height of the pancake. In_{0.3}Ga_{0.7}As is then introduced to stop the vertical growth and hence later growth is only in the lateral direction. The In_{0.3}Ga_{0.7}As growth time can be tuned to adjust the pancake diameter. (b) A 5-min/55-min GaAs/ In_{0.3}Ga_{0.7}As pancake structure grown on a c-plane sapphire substrate.

4.6 AlGaAs Nanoneedle and GaAs/AlGaAs Heterostructures

AlGaAs nanoneedle growths were also attempted to further engineer the material bandgap and also provide surface passivations to the GaAs nanoneedle surface. It is well known that GaAs has a high surface recombination velocity, which would result in an “optically dead zone” near the GaAs surface.¹⁷ Proper surface passivations, with AlGaAs as one of the most common choices, are essential for obtaining better optical properties for GaAs structures. GaAs nanowires were previously reported to have a much brighter emission after being coated with an AlGaAs passivation layer.¹⁸

The growth of a high Al composition (> 70% Al) AlGaAs material was first attempted to passivate a bare GaAs nanoneedle. Trimethylaluminum (TMAI) with a mole fraction of 1×10^{-5} was added to the TEGa and TBA mole fractions of 1.12×10^{-5} and 5.42×10^{-4} , respectively, in a 12 l/min hydrogen carrier gas flow.

The result is a nanoneedle structure with an AlGaAs shell and a GaAs core. In order to demonstrate the AlGaAs shell layer, a sample was sonicated to break the nanoneedle tip followed by selective wet etch to remove the inner GaAs portion. Fig. 4.19 illustrates the process.

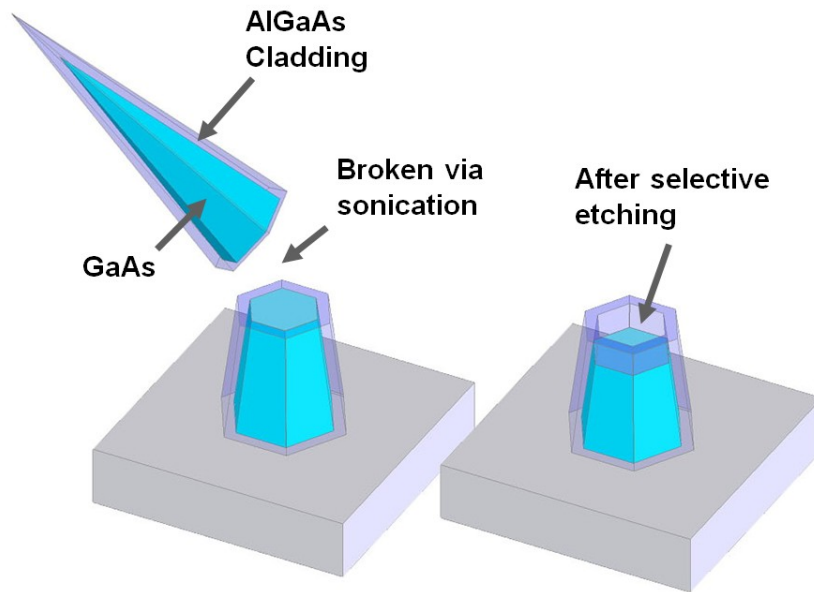


Figure 4.19 Sonication of the AlGaAs-shell, GaAs-core nanoneedles resulted in broken tips. A selective etch was then performed to remove part of the core GaAs material to form hollow nanoneedles.

Fig. 4.20 shows a shell-core AlGaAs-GaAs nanoneedle sample going through the sonication and etching processes. The wet etch was done with a citric-acid solution prepared as follows. First the citric acid powder is mixed with water with a 1:1 weight ratio. Ammonia solution is then slowly added to the above citric acid solution until the pH value reaches 6.4. This solution is then mixed with hydrogen peroxide (H_2O_2) with a 5:1 ratio. The final solution is then heated up to $60^\circ C$ for the desired etch rate. The etch time for the samples shown in Fig. 4.20 was only 3 seconds since the nanoneedles dimensions are small. The etch time was chosen to etch away ~ 150 nm GaAs. After the etch, the AlGaAs shell is seen with ~ 80 nm in thickness and is uniform from the nanoneedle bottom to the top indicating a uniform core-shell growth mode of the AlGaAs material. It also demonstrates the smooth GaAs/AlGaAs interface.

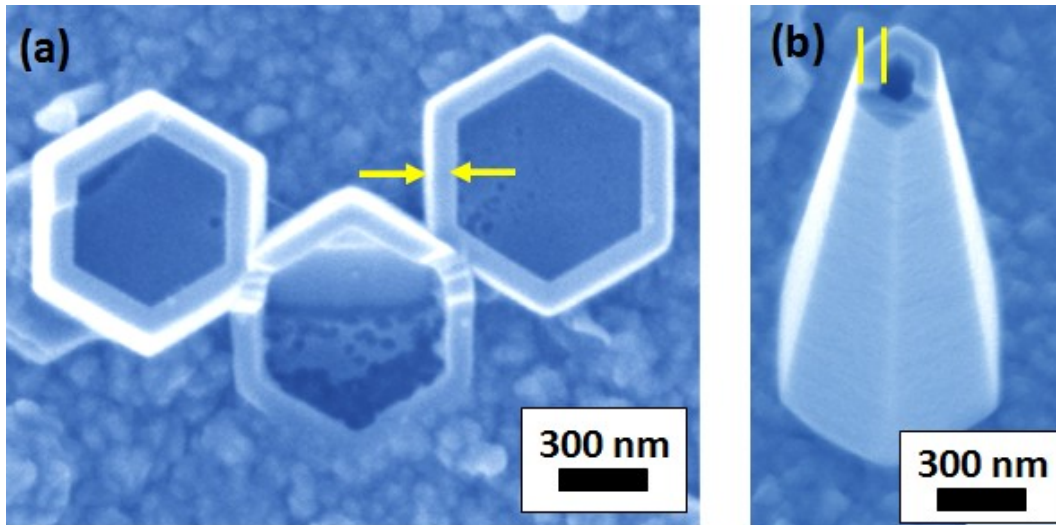


Figure 4.20 (a) Planar-view and (b) 20°-tilt view of some AlGaAs-shell, GaAs-core nanoneedles grown on a (111)Si after sonication and selective GaAs etch. The AlGaAs shell is seen with ~ 80 nm in thickness is uniform from the nanoneedle bottom to the top indicating a uniform core-shell growth mode of AlGaAs material.

Previously in Chapter 4.3 I discussed the optical properties of pure GaAs nanoneedles grown on a (111)Si substrate. The AlGaAs-shell/GaAs core nanoneedles shown above were then measured with the μ -PL setup to test the AlGaAs passivation. Fig. 4.21a shows the PL spectra of an AlGaAs-passivated GaAs nanoneedle and a bare GaAs nanoneedle. The GaAs sizes of the two nanoneedles are the same for fair comparison. It can be seen that the PL intensity from the AlGaAs-passivated sample is $\sim 2x$ brighter than that of the pure GaAs nanoneedle. Fig. 4.21b shows the room-temperature comparison of the same set of nanoneedles. The AlGaAs-passivated nanoneedle shows an even higher $\sim 5x$ improvement as compared to the bare GaAs nanoneedle. This verifies that AlGaAs shell could indeed well passivate the GaAs surface for reducing the non-radiative surface recombinations.

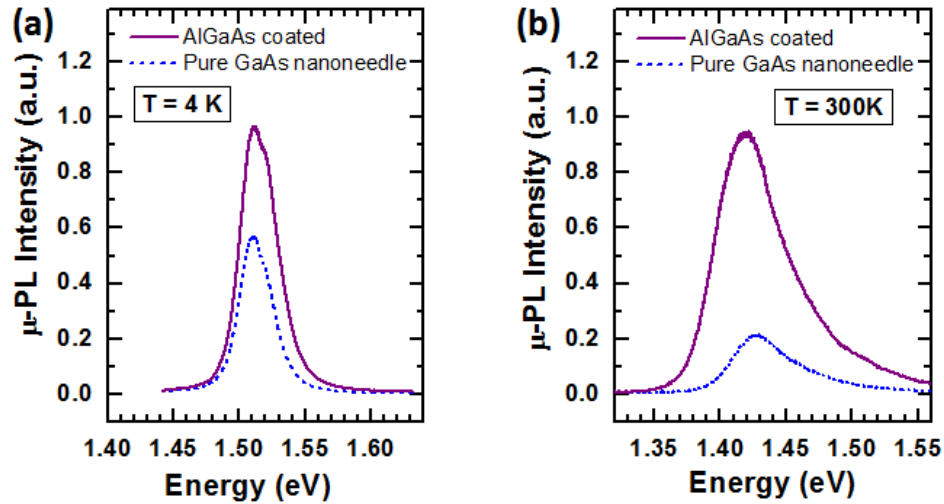


Figure 4.21 (a) 4 K and (b) 300 K PL spectra comparison between an AlGaAs-shell/GaAs-core nanoneedle and a pure GaAs nanoneedles. Both nanoneedles are grown on (111)Si with identical GaAs-portion growth time. It is seen that the AlGaAs passivation indeed increases the PL intensity by $\sim 2\times$ at 4 K and by $\sim 5\times$ at 300 K.

Bulk AlGaAs nanoneedle growth on a (111)Si substrate was also attempted. A lower TMAI mole fraction of 1.25×10^{-6} was used for this bulk AlGaAs nanoneedle growth. The growth temperature was still 400°C . The AlGaAs-shell/GaAs core structure shown in Fig. 4.20 was with a higher TMAI mole fraction of 1×10^{-5} . A lower Al composition was desired for the bulk AlGaAs material since its composition could then be determined by the PL spectrum. It is known that AlGaAs with higher than $\sim 40\%$ of Al composition is of indirect bandgap hence there is nearly no PL emission.¹⁹ Fig. 4.22a shows the preliminary bulk AlGaAs nanoneedle growth on a (111)Si substrate. Although nanoneedles are seen, they have no preferred orientation hence most likely they do not grow epitaxially on the Si substrate. Doubling the TMAI mole fraction to 2.5×10^{-6} resulted in nanoneedle structures with even worse shapes. Kinks are seen indicating the growth is heavily affected by the higher TMAI flow rate. However, the AlGaAs-shell/GaAs core structure shown in Fig. 4.20, which was with even higher Al composition, still grew well meaning AlGaAs can be grown well onto an existing GaAs core as a passivation layer.

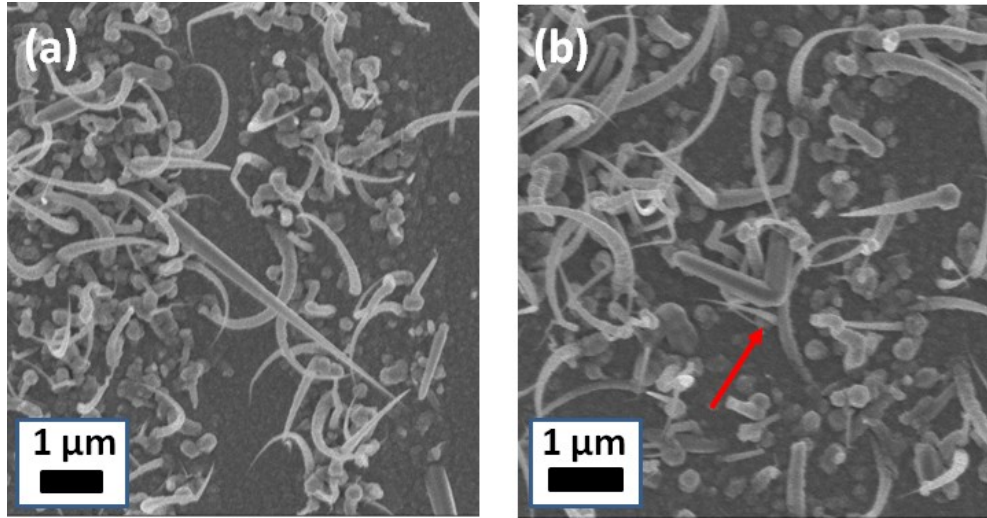


Figure 4.22 Bulk AlGaAs nanoneedles grown on a (111)Si substrate with TMAI mole fraction of (a) 1.25×10^{-6} and (b) 2.5×10^{-6} . The lower TMAI flow rate in (a) resulted in sharp AlGaAs nanoneedles although the nanoneedle is not epitaxial. The higher TMAI flow rate in (b) resulted in nanoneedles with kinks (see red arrow).

A 4 K PL spectrum of the bulk AlGaAs nanoneedle shown in Fig. 4.22a is taken and shown in Fig. 4.23. The spectrum has a main peak at 683 nm (AlGaAs bandgap) with a broad shoulder at longer wavelengths centered about ~ 890 nm. This broad shoulder is thought to be the defect-related emissions since it is below the bandgap and also from the fact that the bulk AlGaAs nanoneedles do not grow epitaxially on Si. The Al composition is then estimated from the 683 nm peak, again using ZB AlGaAs bandgap equation (see below)¹⁴, to be as $\text{Al}_{0.21}\text{Ga}_{0.79}\text{As}$.

$$0 \text{ K } \text{Al}_x\text{Ga}_{1-x}\text{As } E_g \text{ (for } x < 0.4) = 1.519 + 1.447x - 0.15x^2 \text{ (eV)} \quad (4.1)$$

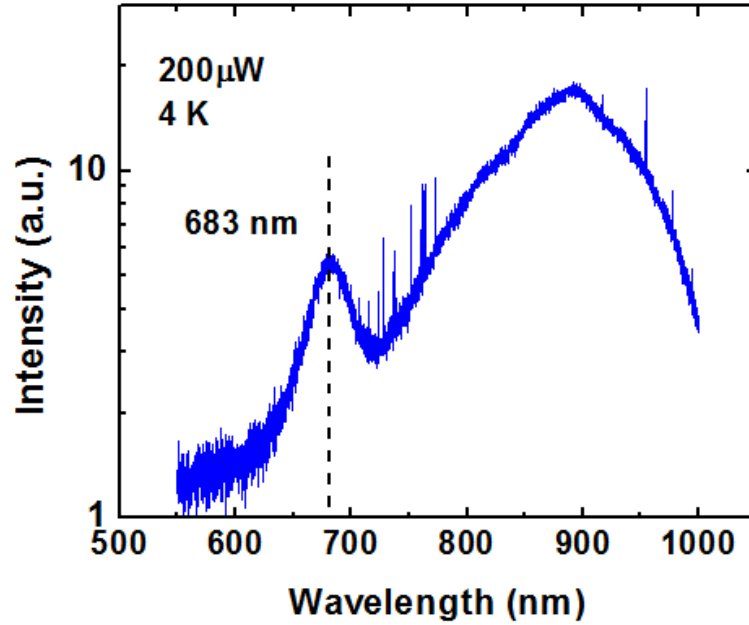


Figure 4.23 PL spectrum of a bulk AlGaAs nanoneedles grown on a (111)Si substrate with TMAI mole fraction of 1.25×10^{-6} . The AlGaAs bandgap emission at 683 nm, corresponding to $\text{Al}_{0.21}\text{Ga}_{0.79}\text{As}$, is seen with a broad shoulder centered about ~ 890 nm. The shoulder emission is thought defect-related.

In conclusion, GaAs-based nanoneedles can be grown epitaxially on to a GaAs, Si or sapphire substrate. Nanoneedles with an ultra sharp tip of only a few nanometers and a small taper angle are synthesized on GaAs with Ge catalyst and mechanical scratching, on Si with only scratching, and completely spontaneous without any surface treatment on a sapphire substrate. This is attributed to the 46% large lattice mismatch between GaAs and sapphire which favors the 3D growth mode. Bulk InGaAs nanoneedles and InGaAs/GaAs QW nanoneedles are also successfully demonstrated which allow the bandgap engineering, and hence the emission wavelength engineering, from the GaAs bandgap all the way to smaller than the Si bandgap. As a consequence InGaAs/GaAs QW nanoneedle structures are suitable active materials for Si photonics applications. AlGaAs nanoneedles and AlGaAs-passivation of GaAs nanoneedles are also demonstrated. The AlGaAs-shell/GaAs-core nanoneedle structures show ~ 5 x room-temperature PL intensity improvement than that of a bare GaAs nanoneedle. The proper AlGaAs passivation largely reduces the non-radiative surface recombinations of a GaAs surface.

References:

- (1) Tavendale, A. J. & Pearson, S. J. Deep level, quenched-in defects in silicon doped with gold, silver, iron, copper or nickel. *J. Phys. C: Solid State Phys.* **16**, 1665-1673 (1983).
- (2) Chuang, L. C., Moewe, M., Chase, C., Kobayashi, N. P., and Chang-Hasnain, C. Critical diameter for III-V nanowires grown on lattice-mismatched substrates. *Appl. Phys. Lett.* **90**, 043115 (2007).
- (3) Moewe, M., Chuang, L. C., Dubrovskii, V. G., & Chang-Hasnain, C. Growth mechanisms and crystallographic structure of InP nanowires on lattice-mismatched substrates. *J. Appl. Phys.* **104**, 044313 (2008).
- (4) Lee, P. W., Omstead, T. R., McKenna, D. R., & Jensen, K. F. In situ mass spectroscopy and thermogravimetric studies of GaAs MOCVD gas phase and surface reactions. *J. Cryst. Growth* **85**, 165-174 (1987).
- (5) Larsen, C. A., Buchan, N. I., Li, S. H., & Stringfellow, G. B. Decomposition mechanisms of tertiarybutylarsine. *J. Cryst. Growth* **94**, 663-672 (1989).
- (6) McMahon, M. I. & Nemes, R. J., Observation of a wurtzite form of gallium arsenide. *Phys. Rev. Lett.* **95**, 215505 (2005).
- (7) Hoang, T. B. et al. Observation of free exciton photoluminescence emission from single wurtzite GaAs nanowires, *Appl. Phys. Lett.* **94**, 133105 (2009).
- (8) Titova, L. et al. Temperature dependence of photoluminescence from single core-shell GaAs-AlGaAs nanowires. *Appl. Phys. Lett.* **89**, 173126 (2006).
- (9) Razeghi, M. et al. High-purity GaAs layers grown by low-pressure metalorganic chemical vapor deposition. *Appl. Phys. Lett.* **55**, 1677-1679 (1989).
- (10) Martelli, F. et al. Photoluminescence of Mn-catalyzed GaAs nanowires grown by molecular beam epitaxy. *Nanotechnol.* **18**, 125603 (2007).
- (11) Kuech, T. F. & Veuhoff, E. Mechanism of carbon incorporation in MOCVD GaAs. *J. Cryst. Growth* **68**, 148-156 (1984).
- (12) Haacke, G., Watkins, S. P., & Burkhard, H. Epitaxial growth of high-mobility GaAs using tertiarybutylarsine and triethylgallium. *Appl. Phys. Lett.* **56**, 478-480 (1990)
- (13) Wang, H. & Chen, A. B. Calculation of shallow donor levels in GaN. *J. Appl. Phys.* **87**, 7859-7863 (2000).
- (14) Chuang, S. L. *Physics of Optoelectronic Devices* (John Wiley & Sons, New York, 1995)
- (15) Zielinski, E. et al. Optical gain and loss processes in GaInAs/InP MQW laser structures. *IEEE J. Quantum Electron.* **25**, 1407-1416 (1989).
- (16) Nobis, T. et al. Whispering gallery modes in nanosized dielectric resonators with hexagonal cross section. *Phys. Rev. Lett.* **93**, 103903 (2004).
- (17) Hasegawa, H. et al. Dynamics and control of recombination process at semiconductor surfaces, interfaces and nano-structures. *Solar Energy* **80**, 629-644 (2006).
- (18) Titova, L. et al. Temperature dependence of photoluminescence from single core-shell GaAs-AlGaAs nanowires. *Appl. Phys. Lett.* **89**, 173126 (2006).
- (19) El Allali, M., Sorensen, C. B., Veje, E., & Tidemand-Petersoon, P. Experimental determination of the GaAs and Ga_{1-x}Al_xAs band-gap energy dependence on temperature and aluminum mole fraction in the direct band-gap region. *Phys. Rev. B* **48**, 4398-4404 (1993).

Chapter 5:

Doping of GaAs Nanoneedles and Nanoneedle P-N Junctions

Dopings, both n-type and p-type, are necessary to create a p-n junction therefore electrical pumping of an optoelectronic device such as a light emitting diode or a laser would be possible. P-n junctions, when reversely biased, could also be used to separate the photogenerated electron-hole pairs inside an III-V semiconductor hence a photodetector or solar cell can be made. Doping the GaAs-nanoneedle structures are challenging since the typical nanoneedle growth temperature of 400°C is low and there are few prior works done in this temperature range. For example, for the most common Si doping source of disilane (Si_2H_6), the doping behavior is only well studied for growth temperatures 600°C and above.¹ The lack of low growth temperature doping study plus the unique wurtzite (WZ) crystal structure of GaAs nanoneedles resulted in nearly no prior work. The low growth temperature itself also adds difficulties to the doping efficiency. Shimazu *et al.* reported that the Si doping concentration, when using disilane, has an Arrhenius dependence on temperature ($K = A \exp(-k/RT)$) for temperatures below ~730°C.¹ By extrapolating their data to estimate the Si doping concentration at 400°C would indicate a Si doping concentration of only $10^{17}/\text{cm}^3$ or lower. As a consequence, both the search for suitable doping sources for ~400°C growths and the understanding of the doping behavior near 400°C have to be done.

5.1 n-type GaAs Nanoneedle with Disilane (Si_2H_6) Doping Source

As I already mentioned, Si doping might be difficult for GaAs nanoneedle materials due to the low doping efficiency at low growth temperatures ~400°C. However, if only $10^{17}/\text{cm}^3$ or lower of the doping concentration is needed, then Si doping is still attractive. It is because Si in GaAs has low diffusion coefficient so the n-doping profile can be well controlled. The availability of high-purity silicon doping sources, e.g., disilane, is also an advantage.

Four GaAs nanoneedle samples, one undoped and three with different disilane doping flow rates, were grown on (111) Si substrates. The growth was done in an MOCVD reactor at a temperature ~400°C. The growth was catalyst free and the process was the same as that shown in Chapter 4.2. The FE-SEM image of an undoped nanoneedle and a Si-doped nanoneedle is shown in Fig. 5.1a and 5.1b, respectively. It is found that the addition of Si dopants, for all the three different disilane flow rates used in this work, did not affect the nanoneedle shape at all. The nanoneedle growth direction [0001] is still parallel to the Si substrate surface normal, which is [111]. The disilane mole fraction, which could be adjusted by the disilane flow rate, for the Si-doped nanoneedle sample shown in Fig. 5.1b was 8.3×10^{-7} in a 12 l/min hydrogen carrier gas flow. This sample is hereafter referred to as “B”. Two other Si-doped samples marked as “A” and “C” are with their disilane flow rates half and twice that of “B”.

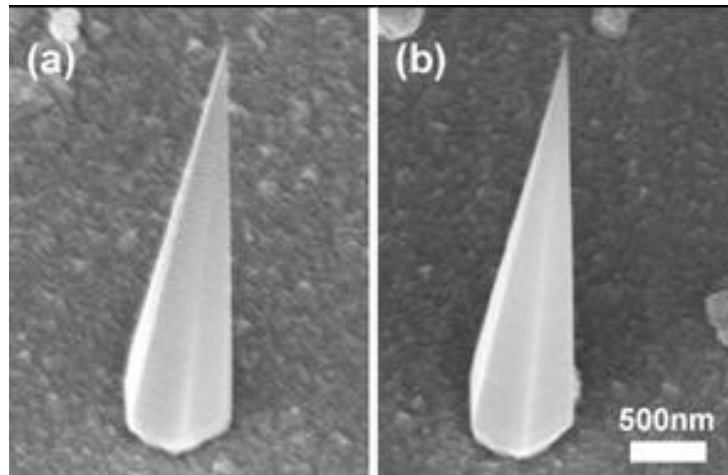


Figure 5.1 30°-tilt FE-SEM images of (a) an undoped GaAs nanoneedle and (b) a Si-doped GaAs nanoneedle on sample B (see text for doping flow rate). The nanoneedle shape was not affected by the addition of Si dopants.

Fig. 5.2a shows the 4 K μ -PL spectra of an undoped nanoneedle and a sample B, Si-doped GaAs nanoneedle under various excitation powers. The laser spot size was focused down to ~ 1.5 μm to ensure that only one nanoneedle was illuminated at a time. Sample B nanoneedle was found to be redder and with higher peak intensity than the undoped one. The wavelength redshift can be explained by bandgap narrowing which is commonly seen in highly doped bulk semiconductors.² Si doping also reduced the width of the surface depletion region, which was referred to as the optically dead layer,³ therefore the μ -PL intensity was higher. Fig. 5.2b and 5.2c show the excitation-power-dependent peak wavelength and intensity, respectively, as extracted from Fig. 5.2a. In Fig. 5.2b, when the excitation power increased from 10 μW to 100 μW , the peak wavelength showed blueshift for both samples due to band filling effect. Thermal effect then came into play when the excitation was higher than 100 μW . It drove the peak wavelength redder.

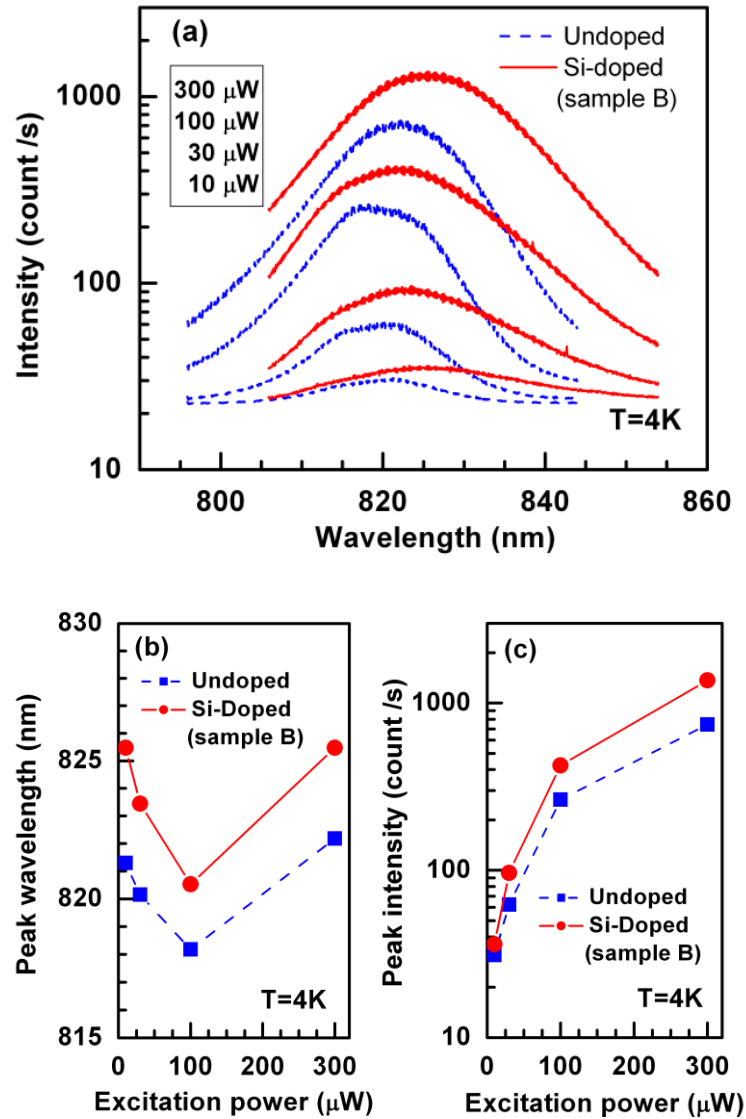


Figure 5.2 4 K μ -PL results of an undoped nanoneedle and a Si-doped nanoneedle on sample B. (a) Spectra taken under various excitation powers from 10 μ W to 300 μ W. The laser spot was focused to ~ 1.5 μ m to ensure the illumination of only one single nanoneedle. (b) Peak wavelength versus excitation power. (c) Peak intensity versus excitation power.

Room-temperature μ -PL was performed on exactly the same nanoneedles shown in Fig. 5.2. As shown in Fig. 5.3a, the wavelength increased monotonically as excitation power increased since thermal effect dominated at room temperature. In Fig. 5.3b, the room temperature μ -PL intensity enhancement for sample B to the undoped sample is comparable to that of the 4 K data (Fig. 5.2c) under the same excitation powers. For example, the intensity ratio of sample B to the undoped sample is roughly two at the 300 μ W excitation.

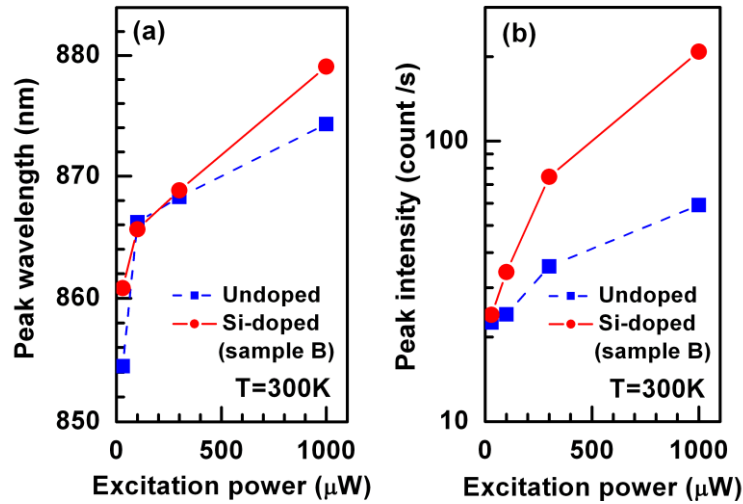


Figure 5.3 Room-temperature μ -PL results of the undoped nanoneedle and the Si-doped nanoneedle on sample B. (a) Peak wavelength versus excitation power. (b) Peak intensity versus excitation power.

The disilane doping flow rate influence on μ -PL characteristics for all four samples is summarized in Fig. 5.4. The horizontal axis is normalized to the doping flow rate of sample B. Hence “0.5”, “1.0”, and “2.0” represent sample A, B, and C, respectively. As shown in Fig. 5.4a, the PL peak wavelength became redder and redder as doping flow rate increased. It indicates bandgap narrowing. From the amount of bandgap narrowing, the Si doping concentration is estimated as $\leq 10^{17}/\text{cm}^3$ for sample B and C.² The peak intensity also increased as illustrated in Fig. 5.4b due to the increasing doping concentration and hence a smaller surface depletion region.

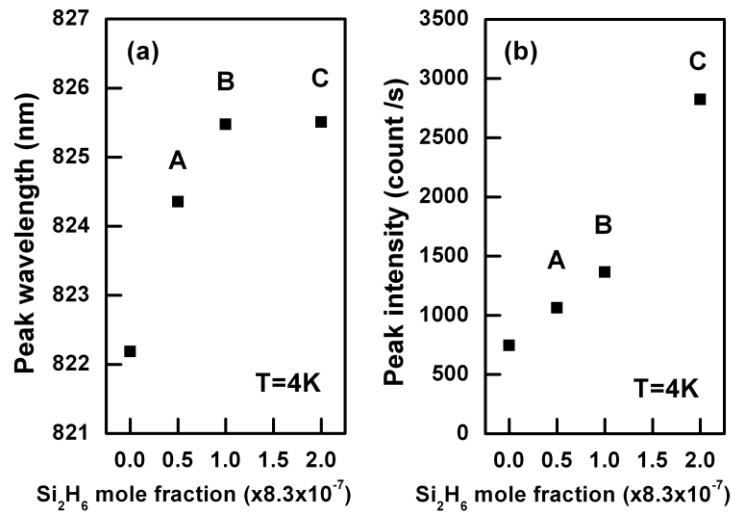


Figure 5.4 Disilane doping flow rate dependence on (a) peak wavelength and (b) peak intensity. μ -PL was done at 4 K with a 300 μ W excitation power.

In conclusion, we report the successful incorporation of Si dopant into the novel GaAs nanoneedle structure although the doping concentration seems to saturate at $10^{17}/\text{cm}^3$. For yielding lightly n-type doped GaAs nanoneedles, disilane doping remains as a good choice.

5.2 n-type GaAs Nanoneedle with Diethyltellurium (DETe) Doping Source

Diethyltellurim (DETe) source is a promising metal organic source for low temperature growths. DETe has been used to grow HgTe material at temperatures as low as 390°C.⁴ Houg *et al.* also reported that the carrier concentration for Te-doped GaAs could go up to as high as $1 \times 10^{19}/\text{cm}^3$ and the carrier concentration had a negative growth temperature dependence, i.e., lower growth temperature would favor the Te dopant incorporation.⁵ Another advantage of Te doping is that it is a group VI dopant. Therefore, it is unambiguously an n-type dopant. Si, on the other hand, might occupy the As site and becomes an unwanted p-type dopant. The only potential drawback for the DETe doping source is the memory effect. Houg *et al.* found that adsorption of DETe onto the stainless steel tube walls gives rise to doping memory effects which produce about $(1-2) \times 10^{15}/\text{cm}^3$ of background impurity concentration in an unintentionally doped GaAs layer. However, if necessary, heating the tube to 60°C can reduce the background doping level back to $2 \times 10^{14}/\text{cm}^3$.

Four Te-doped GaAs nanoneedle samples were grown on n-type (111)Si substrates to investigate the DETe doping behavior. The four GaAs nanoneedle samples are with DETe mole fractions of 1.08×10^{-7} , 2.70×10^{-7} , 5.4×10^{-7} and 8.1×10^{-7} , respectively. The mole fraction ratio between them is 1 : 2.5 : 5 : 7.5 hence they are herein referred as the 1x-Te, 2.5x-Te, 5x-Te and 7.5x-Te samples. The 1x-Te, 2.5x and 5x-Te samples show sharp nanoneedles like the undoped ones. However, there is no sharp nanoneedle seen in the 7.5x-Te sample. Fig. 5.5 shows the top-down SEM images of three samples with higher Te-doping levels. It is clearly seen that the 7.5x-

Te doping is too high, which affects the nanoneedle growth mode. Therefore, the 7.5x-Te sample is “overdoped” in terms of the nanoneedle shape.

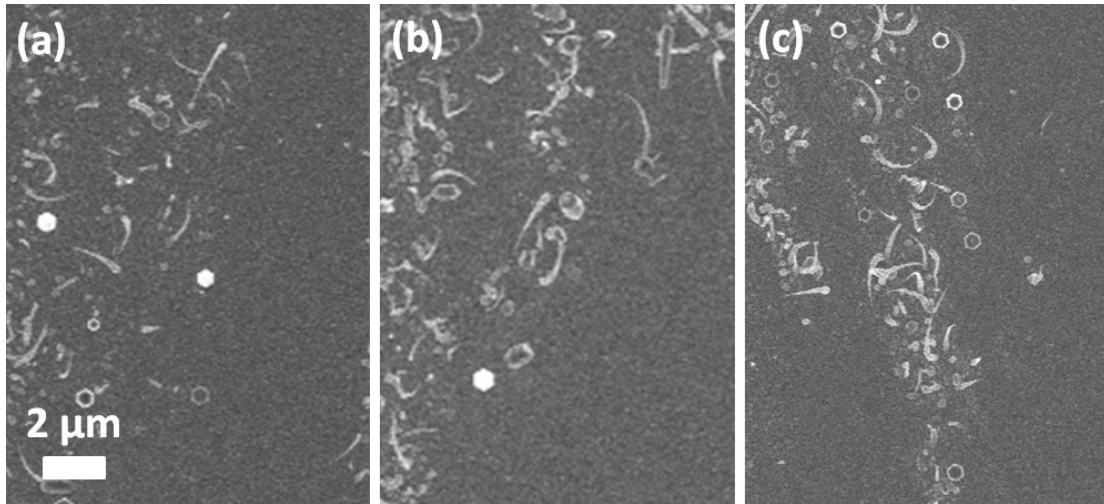


Figure 5.5 GaAs nanoneedles with different DETe doping mole fractions. (a) 2.5x-Te (b) 5x-Te (c) 7.5x-Te (see text for doping mole fraction definition). The 2.5x-Te and 5x-Te samples still resulted in sharp nanoneedles while no sharp nanoneedle can be seen for the 7.5x-Te sample.

For measuring the electrical properties of these Te-doped GaAs nanoneedle samples, some simple devices were fabricated as that shown schematically in Fig. 5.6a. The as-grown nanoneedle samples were first coated with spin-on glass (SOG) followed by the SOG curing. The SOG was cured at a low temperature of 300°C for 2 hours with a slow temperature ramping up and ramping down rate of 100°C/h to avoid SOG cracking. A ~0.65 μm thick SOG layer was used for this batch. After the curing, a short CF₄/O₂ ash was performed in a plasma-thermal parallel plate plasma etcher to remove the remaining SOG on nanoneedle sidewalls. A square patterned Ni/Ge/Au film of 15/25/150 nm was then deposited onto the SOG as the top contact metal. Each top contact pad, which defines the testing device size, contains about 40-50 nanoneedles as estimated under an optical microscope. Another contact was formed at the backside of the Si substrate. The I-V curves of the four Te-doped samples are shown in Fig. 5.6b. It can be clearly seen that the 2.5x-Te sample and the 5x-Te sample I-V have larger current and better linearity while the 1x-Te and 7.5x-Te samples show smaller current and a larger contact resistance (worse linearity). The 1x-Te sample should be with too low of a doping level and 7.5x-Te sample is overdoped as suggested by the nanoneedle shape being affected shown in Fig. 5.5c. The electron mobility for the 7.5x-Te could be very low hence a high resistance is seen. The metal contacts for these samples were the as-deposited ones. They had not been annealed thus this might be the reason for a noticeable contact resistance for all the samples. Further annealing should be able to improve the contact resistance. However, since the device resistance of a nanoneedle-based device would be large due to its high aspect ratio, the contact resistance associated with Fig. 5.6b, although not ideal, might play a very minor role in the overall performance of a nanoneedle optoelectronic device.

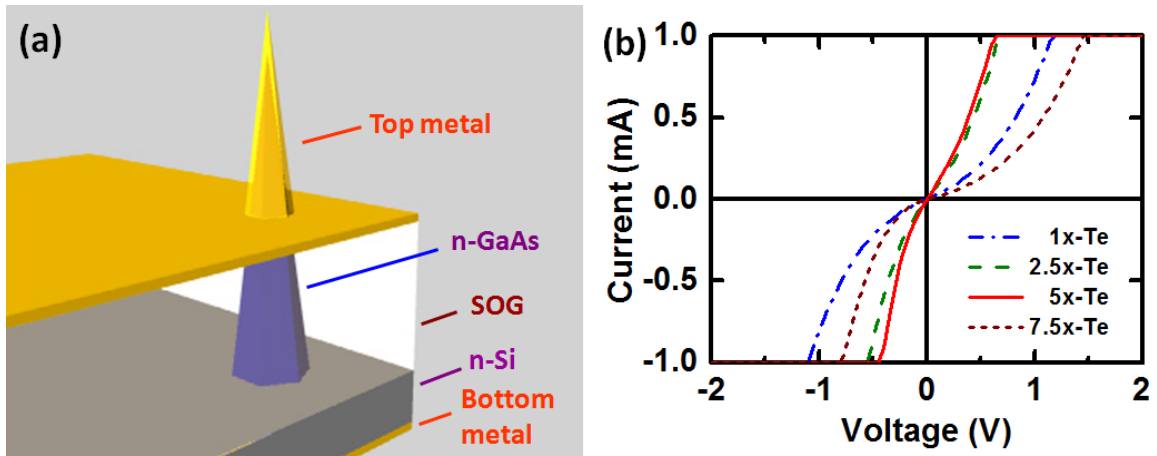


Figure 5.6 I-V measurement of the Te-doped GaAs nanoneedles. (a) Test device schematic. SOG is used as a planarization material. The top contact metal is Ni/Ge/Au. (b) IV curves of four Te-doped samples. The 1x-Te sample has the lowest doping level hence it shows a smaller current and a larger contact resistance (worse linearity). The 2.5x-Te and 5x-Te are sufficiently doped to allow the as-deposited metal contact work well. The current of the 7.5x-Te sample falls smaller again presumably due to the over-doping. Each test device has ~ 50 nanoneedles as counted under an optical microscope.

The free electron concentration of these four samples cannot be accurately determined by the I-V curves since apparently a contact resistance effect is included. Therefore another approach trying to estimate the doping levels with an optical measurement was attempted. Fig. 5.7a shows the μ -PL spectra of the 1x-Te, 2.5x-Te and the 7.5x-Te samples. First of all, all the spectra show a peak near the GaAs bandgap of 816 nm. A red shoulder is also seen for all three samples. This red shoulder is thought from the impurity/defect states as it becomes even larger than the near-bandgap peak for the 7.5x-Te sample. Secondly, the overall PL intensity decreases significantly with the increasing Te-doping density. This can also be explained by the increasing impurity/defect states as the DETe doping flow rate increases. In order to better compare the near-bandgap (near 816 nm) peaks, the PL spectra for the 2.5x-Te and 7.5x-Te samples are enlarged and plotted in Fig. 5.7b. It is very clear that the near-bandedge peak blueshifts with the increasing Te doping. This blueshift with the increasing doping level is well known as the Burstein-Moss shift⁶ and the shift is due to the band filling with the increasing free carrier density. The three peak positions are 819 nm, 791 nm and 768 nm, respectively, for the 1x-Te, 2.5x-Te, and 7.5x-Te samples.

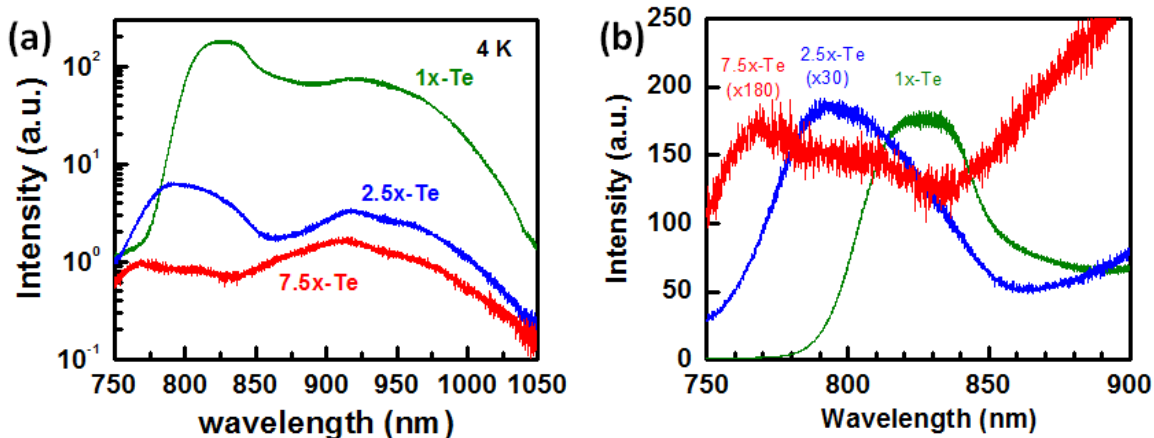


Figure 5.7 (a) 4 K PL Spectra of 1x-Te, 2.5x-Te and 7.5x-Te GaAs nanoneedle samples. All the spectra have a peak near the GaAs bandgap of 816 nm and a red shoulder tentatively assigned to impurity/defect states. The PL intensity decreases significantly with the increasing DETe flow rate. (b) Comparison between the near-bandedge peaks for the three different Te-doped samples. A blueshift with increasing DETe flow rate is clearly seen showing the Burstein-Moss shift. The excitation powers for the 1x-Te and the 2.5x-Te was 100 μ W while that of the 7.5x-Te was 80 μ W. This small excitation power difference does not affect the above analyses.

By comparing these peak positions to a previous report by De-Sheng *et al.*,⁷ the free electron concentration can be estimated optically. The carrier (free electron) concentration as a function of the DETe mole fraction is then plotted in Fig. 5.8. The horizontal axis is with a unit of the 1x-Te DETe mole fraction (1.08×10^{-7}). Therefore the three data points represent 1x-Te, 2.5x-Te and 7.5x-Te GaAs nanoneedle samples. An eye guide (dashed line) shows that the 7.5x-Te sample is indeed overdoped.

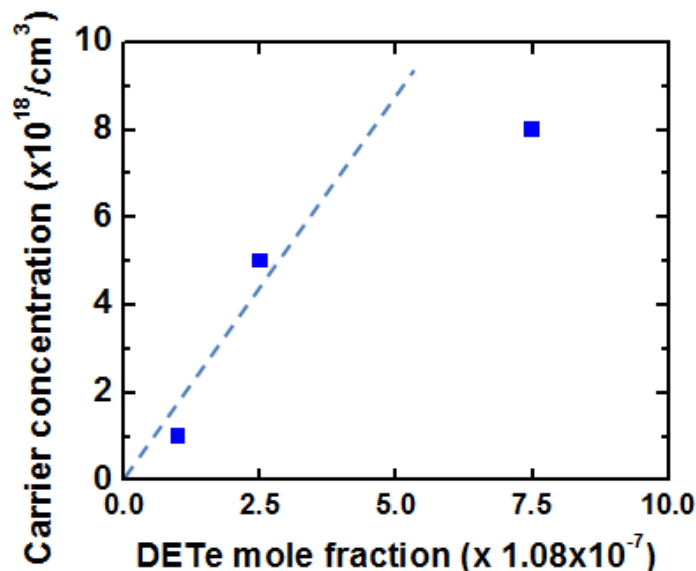


Figure 5.8 Carrier concentration determined by the PL peak position as a function of the DETe mole fraction. The horizontal-axis is with a unit of the 1x-Te DETe mole fraction. Therefore three data points represent the 1x-Te, 2.5x-Te and 7.5x-Te GaAs nanoneedle samples. An eye guide (dashed line) shows that the 7.5x-Te sample is saturated (overdoped).

5.3 p-type GaAs Nanoneedle with Diethylzinc (DEZn) Doping Source

Diethylzinc (DEZn) source is also a common p-type dopant for MOCVD p-type GaAs. Similarly to DETe, the free carrier (hole) concentration when using DEZn as a p-type dopant has a negative temperature dependence. Hageman *et al.* reported that when keeping the DEZn flow rate constant, the free-carrier concentration varies exponentially with $1/T$.⁸ Also similar to DETe, DEZn can yield a high carrier density of $10^{19}/\text{cm}^3$ or even higher.

Three DEZn flow rates were tested for the p-type GaAs nanoneedle growth on p-type (111)Si substrates. The three DEZn mole fractions tested were 1.08×10^{-7} , 5.4×10^{-7} and 2.7×10^{-6} . In order to have a better comparison to the DETe doping study, we define here the 1x-Zn DEZn mole fraction as the same as that of the 1x-Te, which is 1.08×10^{-7} . Therefore, based on the mole fraction ratios, the three Zn-doped samples are then labeled as 1x-Zn, 5x-Zn, and 25x-Zn, respectively. The SEM images of the Zn-doped GaAs nanoneedles are shown in 5.9. While the 1x-Zn and 5x-Zn nanoneedle maintained the smooth sidewall and sharpness, the shape of the 25x-Zn is largely changed. The 25x-Zn GaAs nanoneedle is much smaller than the other two in size. The sidewall is also rough showing lots of defects/stacking faults. It is very obvious the 25x-Zn DEZn flow cannot be used and the sample is overdoped.

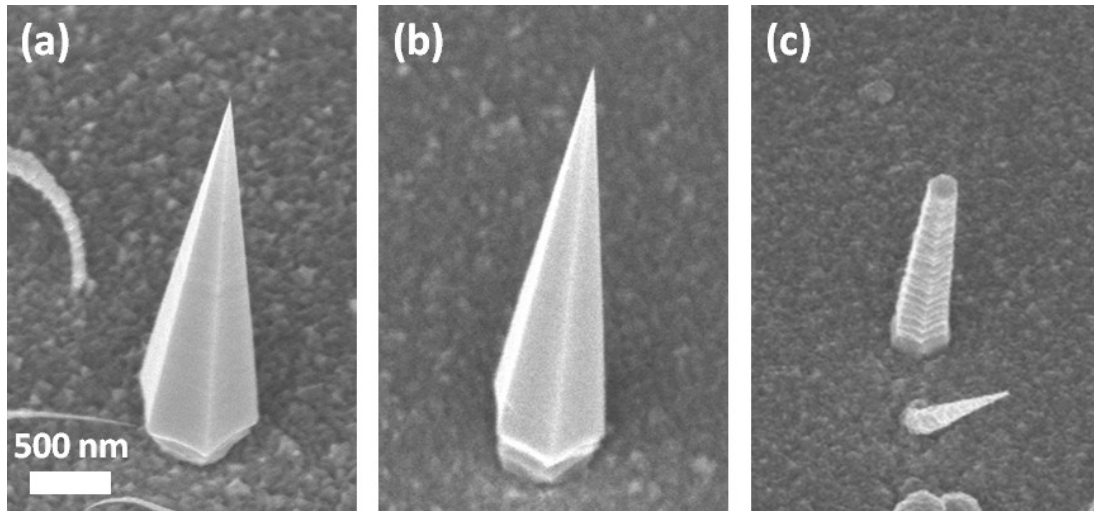


Figure 5.9 GaAs nanoneedles with different DEZn doping mole fractions. (a) 1x-Zn (b) 5x-Zn (c) 25x-Zn (see text for doping mole fraction definition). The 1x-Zn and 5x-Zn GaAs nanoneedles still maintain the smooth sidewalls and sharp tips while the 25x-Zn nanoneedle is much smaller in size with a rough sidewall indicating lots of defects.

The electronic properties of the Zn-doped GaAs nanoneedles are measured via the I-V dependence, which is similar to that done for the Te-doped GaAs nanoneedle characterization. Fig. 5.10a shows the test device schematic. All the processes are nearly the same as that of the Te-doped GaAs nanoneedle device test batch. The only differences are that the SOG is $\sim 1.3 \mu\text{m}$ for these Zn-doped samples and the top contact metal is Ti/Au. The I-V dependence of the 1x-Zn GaAs nanoneedle sample is shown in Fig. 5.10b. Linear I-V characteristics were observed indicating minimum contact resistance. For a device with about 10 nanoneedles and a device with 5 nanoneedles, counted under optical microscope, the current levels changed accordingly. A control device with no nanoneedle was also measured and showed no current at all. This verified the good SOG isolation. Assuming the bulk mobility of p-type GaAs,⁹ the carrier concentration is estimated as 5×10^{17} - $1 \times 10^{18}/\text{cm}^3$ from Fig. 5.10b.

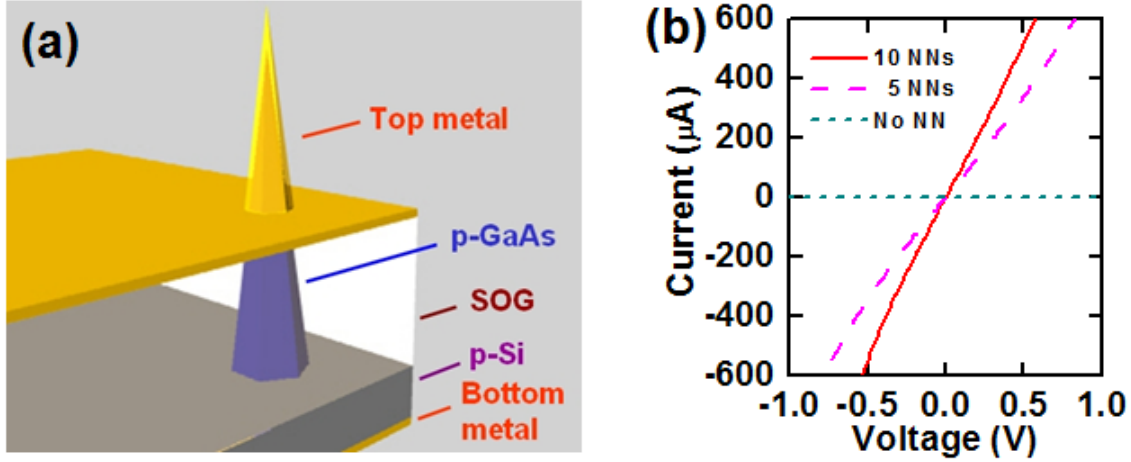


Figure 5.10 I-V measurement of the Zn-doped GaAs nanoneedles. (a) Test device schematic. SOG is used as a planarization material. The top contact metal is Ti/Au. (b) IV curves of the 1x-Zn GaAs nanoneedle sample. The I-V linearity is good indicating minimum contact resistance. The current of a 10-nanoneedle device is approximately 2x than that of a 5-nanoneedle device. A device with no nanoneedle shows no current indicating good SOG isolation.

Similarly to the Te-doped GaAs nanoneedles, the carrier concentration of the Zn-doped GaAs nanoneedles was also investigated via the μ -PL measurement. 4 K μ -PL of the Zn-doped nanoneedles was done with a diode-pumped solid-state 532 nm laser source. The laser spot was focused to $\sim 1.5 \mu\text{m}$ in diameter to ensure the excitation of only a single nanoneedle. Fig. 5.11a shows the normalized PL spectra of the Zn-doped nanoneedles and that of an undoped nanoneedle for comparison. The Zn-doped nanoneedle PL shows blueshift as the DEZn mole fraction increases. The blueshift is again attributed to the Burstein-Moss shift, which happens to materials with very high doping concentrations. The full-width half maximum (FWHM) of the Zn-doped nanoneedles is also largely increased, a signature of heavily doped materials.

A quantitative analysis of the PL spectra is given below. Fig 5.11b shows the peak PL wavelength and the FWHM as a function of the DEZn flow. The PL peak shift, which represents the bandgap change ΔE_g , is an overall effect due to the bandgap narrowing ΔE_{BGN} and Burstein-Moss shift ΔE_{BMS} .

$$\Delta E_g = \Delta E_{BGN} + \Delta E_{BMS} \quad (5.1)$$

$$\Delta E_{BGN} = -C_{BGN} N_A^{1/3} \quad (5.2)$$

$$\Delta E_{BMS} = C_{BMS} p^{2/3} \quad (5.3)$$

C_{BGN} ⁶ is a positive empirical constant $\sim 2 \cdot 10^{-8}$ when the amount of bandgap change ΔE_{BGN} is measured in eV and the Zn acceptor concentration N_A is measured in cm^{-3} . C_{BMS} ⁷ is also a positive empirical constant $\sim 2 \cdot 10^{-14}$ when the amount of bandgap change ΔE_{BMS} is measured in eV and the carrier concentration p is measured in cm^{-3} . Since Zn is a shallow dopant in GaAs, we use the approximation $N_A \sim p$ in our calculation.

The PL FWHM broaden $\Delta FWHM$ due to the doping can be expressed by the following equation,¹⁰

$$\Delta FWHM = \frac{2e^2}{3\pi\epsilon} \sqrt{N_A \frac{\pi r_s}{3}} e^{-3/4} 2\sqrt{2 \ln 2} \quad (5.4)$$

Where e is the single electron charge, ϵ is the permittivity and r_s is the Debye length. This equation provides an independent check for the doping concentration.

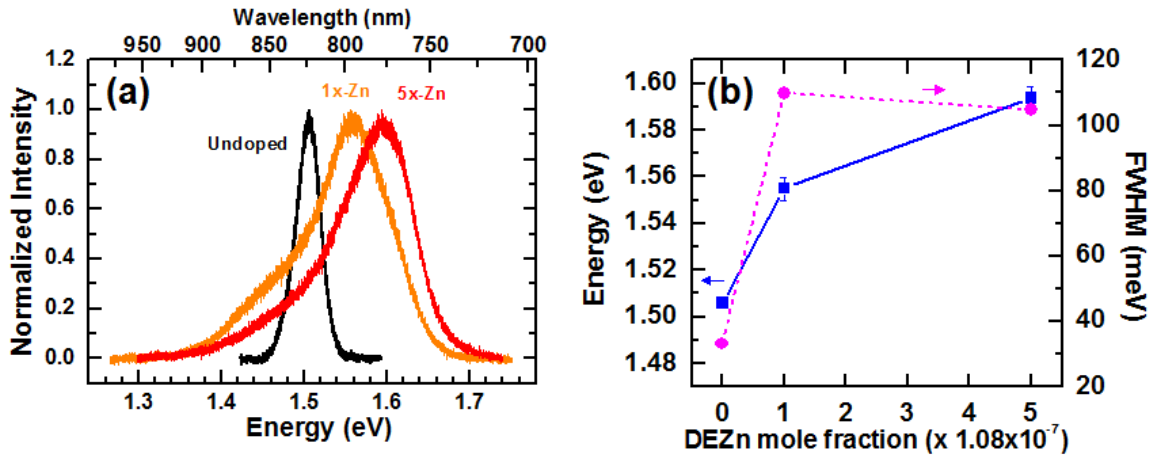


Figure 5.11 μ -PL analyses for Zn-doped GaAs nanoneedles. (a) 4K PL Spectra of an undoped, a 1x-Zn and a 5x-Zn GaAs nanoneedles. The peak shows a large blueshift with an increasing DEZn flow rate which is attributed to the Burstein-Moss shift. (b) Peak energy and the FWHM as a function of the DEZn mole fraction. The FWHM widens with the Zn doping.

For the 1x-Zn GaAs nanoneedle sample, the PL peak wavelength blueshifts for 49 meV from the undoped sample (Fig. 5.11a). The Zn acceptor concentration N_A is then estimated as $\sim 10^{19}/\text{cm}^3$ from equation (5.1)–(5.3). The PL FWHM for the 1x-Zn sample broadens for 77 meV from the undoped control. The Zn acceptor concentration N_A is again estimated as $\sim 10^{19}/\text{cm}^3$ from equation (5.4), by taking the Debye length of highly Zn-doped GaAs as 30 Å.¹¹ Both the bandgap change ΔE_g and the FWHM change $\Delta FWHM$ give identical Zn doping concentration estimation. It is noted that the FWHM of the 1x-Zn sample is slightly larger than that of the 5x-Zn sample. This could be due to the second peak at the lower energy side of 1x-Zn PL (Fig. 5.11a). The presence of the second peak slightly affects the measurement of the FWHM of the main peak. This estimate is about an order of magnitude larger than that estimated from the I-V measurements. Nevertheless, both indicate a high Zn doping concentration which would be enough for typical optoelectronic devices.

5.4 P-N Junctions in a GaAs Nanoneedle

With the capability of doping a GaAs nanoneedle into n-type with Si or Te, and p-type with Zn, p-n junctions were tested. First a simple p-n junction design consisting of only p-type GaAs nanoneedles on an n-type substrate was tested. The junction is at the nanoneedle-substrate interface. The design of the test device is schematically shown in Fig. 5.12a. Both a degenerately doped arsenic-doped Si substrate (n^+ -Si) and a lightly phosphorus-doped Si (n-Si) substrate were used. Surprisingly the I-Vs did not show any rectifying effect (Fig. 5.12b).

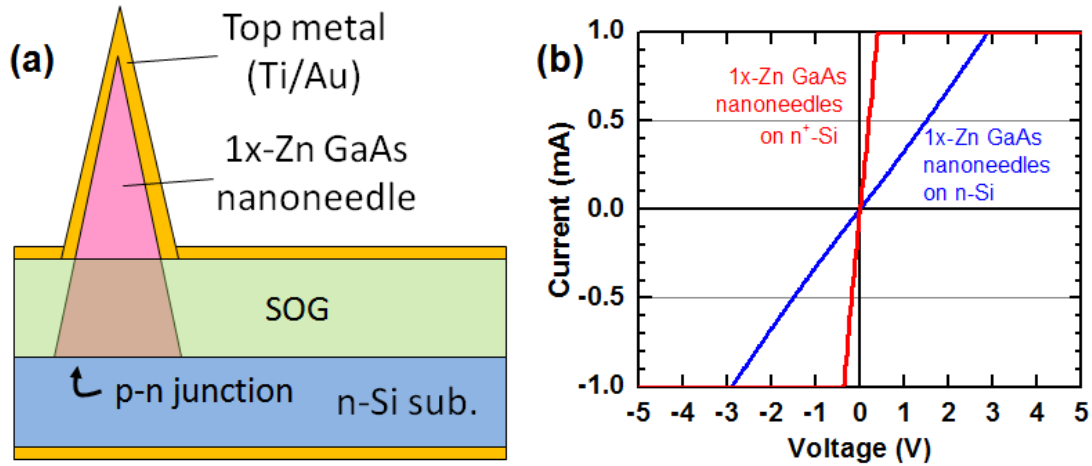


Figure 5.12 (a) A simple p-n junction design putting the junction at the interface between a p-type GaAs nanoneedle and an n-type Si substrate. (b) I-Vs for 1x-Zn GaAs nanoneedles on an n-Si and on an n^+ -Si substrate. Both I-Vs surprisingly do not show any rectifying effect.

In order to find out the cause of this vanishing p-n junction, a detailed examination of the nanoneedle growth, especially for the root portion, was done. It is found that the nanoneedle growth is accompanied with a thin connecting layer as shown Fig. 5.13a. This side-view image of a 60-min GaAs nanoneedle growth on a sapphire substrate shows a 200 nm thick connecting layer covering the whole substrate surface except for the places where nanoneedles grow. The same connecting layer is seen for GaAs nanoneedles grown on Si. The high SEM image contrast for the on-sapphire sample makes the observation of this connecting layer easier. The connecting layer looks very rough under the SEM. Therefore, it is unlikely to be single crystal. It has been reported that GaAs grown on sapphire at low temperatures are polycrystalline.¹² We performed a wet etch on this connecting layer and it had a similar etch rate to the single crystalline GaAs. Therefore, the connecting layer should not be amorphous. We hence tentatively assign the connecting layer crystal structure as polycrystalline. TEM analysis is needed to verify this assumption. With the presence of this connecting layer, the nanoneedle growth is thought as what is shown in Fig. 5.13b. For each incremental growth, a single crystalline thin film is deposited onto the sidewall of a nanoneedle. This is the single-crystal portion of the growth. At the same time, a thin polycrystalline thin film is deposited onto the polycrystalline connecting layer. As a result, for the final nanoneedle structure, the single-crystalline part of the root has a reverse taper angle and has only a small single-crystalline joint (schematically shown in red in Fig. 5.13b) to the substrate. The nanoneedle is securely held onto the substrate by the

surrounding polycrystalline connecting layer. The single-crystalline portion of a nanoneedle is outlined by the dashed lines in Fig. 5.13b.

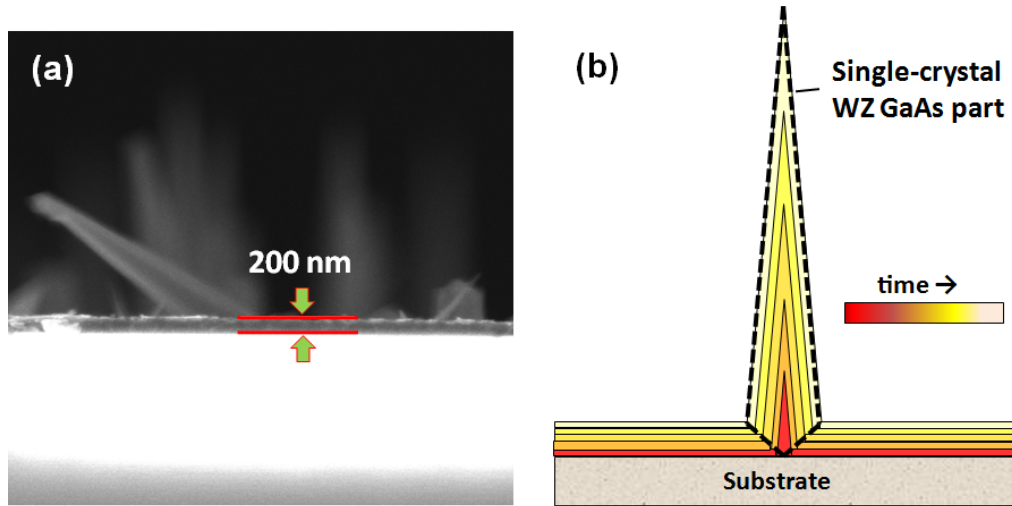


Figure 5.13 (a) Side-view SEM image of a GaAs-nanoneedle-on-sapphire sample. A connecting layer of 200 nm is seen. This connecting layer is tentatively assigned of polycrystalline crystal structure (see text for details). (b) The nanoneedle growth with the accompanying connecting layer deposition. The single-crystal part of a WZ GaAs nanoneedle is outlined by dashed lines.

With the knowledge of the detailed root structure for a GaAs nanoneedle, the current conduction through the p-GaAs nanoneedle to an n-type Si substrate can be understood as follows. Fig. 5.14 illustrates the current conduction path. A current first flows through the p-type GaAs nanoneedle body, then it encounters the 1st junction, the p-nanoneedle and p-poly-GaAs interface (J_{NP}). The current then flows through the poly-GaAs then it encounters the 2nd junction, the p-poly-GaAs and n-Si substrate interface (J_{PS}). Finally the current flows into the n-Si substrate and then be collected at the backside of the substrate. Comparing the p-nanoneedle on n-Si and on n⁺-Si experiments shown in Fig. 5.12, the only differences along the current conduction path are the p-poly-GaAs and n-Si substrate interface (J_{PS}) and the Si substrate itself. It will be shown shortly that the resistance of both types of Si substrate (n and n⁺) are negligible hence the difference in the I-Vs seen in Fig. 5.12b was due to the different J_{PS} junction. J_{PS} junction, although it consists of a p-poly-GaAs and an n-type Si substrate, does not act as a rectifying junction. J_{PS} is simply an ohmic junction with a finite resistance and the resistance for J_{PS} with n-Si is higher than that for J_{PS} with n⁺-Si as can be seen from Fig. 5.12b. We suspect that this ohmic junction may be the result of defect (trap) assisted tunneling.¹³

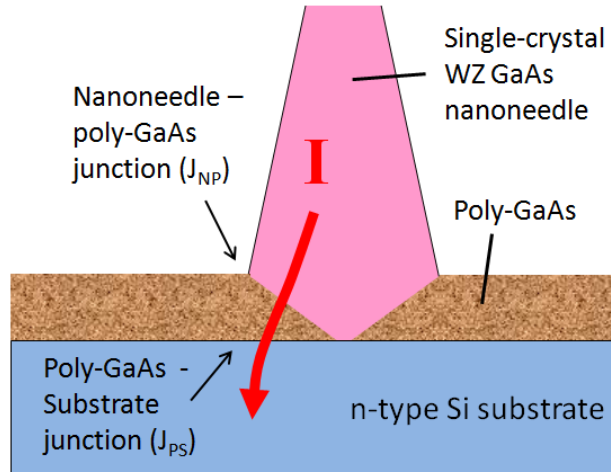


Figure 5.14 Current conduction from a GaAs nanoneedle body to the Si substrate through the poly-GaAs connecting layer. Two junctions are in the conduction path – the nanoneedle to poly-GaAs junction (J_{NP}) and the Poly-GaAs to substrate junction (J_{PS}). J_{PS} dominates the I-V characteristics for the p-GaAs-nanoneedle-on-n-type-Si samples (see text for details).

To verify the above analysis, the electrical property of J_{PS} was tested by a simple method. A probe was in direct contact with the connecting layer to inject current (Fig. 5.15a). Fig. 5.15b shows the I-V characteristics of the two previously mentioned 1x-Zn-on-n-Si and the 1x-Zn-on- n^+ -Si samples, with direct probing of the connecting layers. J_{PS} junction is the only difference in these two samples with the negligible substrate resistance, which is also shown in Fig. 5.15b as nearly overlaying on the vertical axis. It is clearly seen from Fig. 5.15b that the J_{PS} for n-Si is indeed more resistive than the J_{PS} for n^+ -Si, and they are all ohmic. For comparison, the I-Vs with nanoneedles involved in the current conduction path, which were previously shown in Fig. 5.12b, are also plotted here as the dashed lines. With the addition of the p-type GaAs nanoneedle resistance, the current (dashed lines) dropped a little as compared to the pure-connecting-layer I-Vs (solid lines). Nevertheless this shows that J_{PS} is the bottleneck of the current conduction.

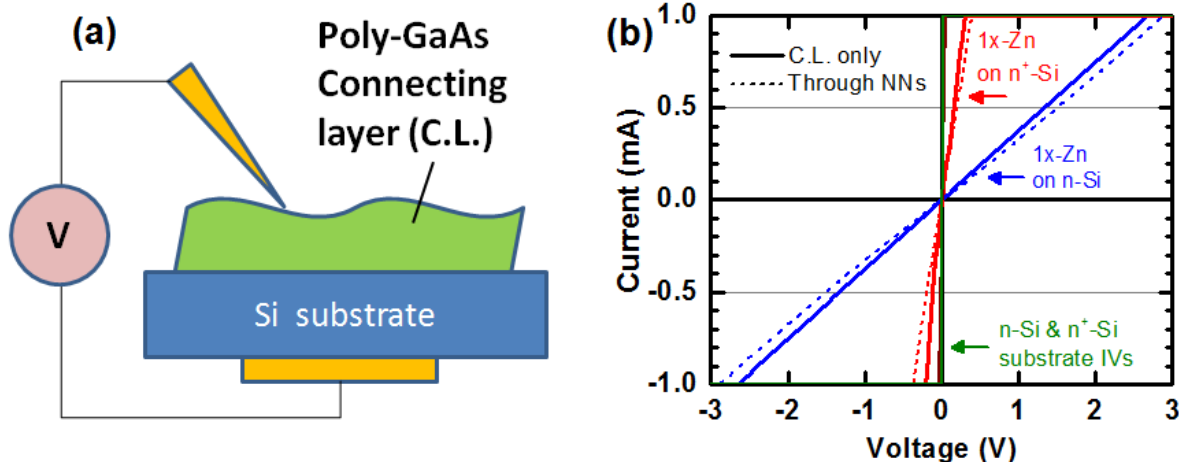


Figure 5.15 (a) Schematic showing direct probing of a connecting layer (C.L.) grown on Si. (b) The I-Vs of the two 1x-Zn connecting layer samples (solid lines). One is on n-Si and another one is on n⁺-Si. The I-Vs are dominated by the poly-GaAs to Si junction, J_{PS} . The I-Vs involving the current conduction through p-GaAs nanoneedles, previously shown in Fig. 5.12b, are also shown for comparison (dashed lines). The I-Vs for a bare n-Si and a bare n⁺-Si substrate are also shown. Both substrates have a negligible resistance.

We can now give a short summary of the electrical properties of the p-nanoneedle-to-n-type-Si junction, J_{PS} . This junction is ohmic and its resistance depends on the doping level of the n-Si substrate. Again we suspect that this ohmic junction is the result of defect (trap) assisted tunneling.¹³

With the understanding of the current conduction at nanoneedle roots, a p-n junction at the nanoneedle and substrate interface is unlikely to be successful. We then moved the p-n junctions inside a nanoneedle instead. Fig. 5.16a shows the schematic of a GaAs p-n nanoneedle structure. A $\sim 10^{17}/\text{cm}^3$ n-type, Si-doped GaAs core of 500 nm in diameter was first grown on an n-type (111)Si substrate, followed by a 50 nm thick, $\sim 10^{18}/\text{cm}^3$ p-type, Zn-doped GaAs shell. The final p-n test device was fabricated through the identical processes described in Chapter 5.3, which was for the p-GaAs nanoneedle on a p-Si substrate. In this simple process flow, the as-grown nanoneedle sample would just go through SOG filling and curing and then the top- and bottom-metal deposition (Fig. 5.16b). The I-V curve of the p-n device is shown in Fig. 5.16c. The I-V curve has a “turn on” at ~ 2 V, indicating that there is a rectifying junction. However, it comes with a large, resistive leakage path. The I-V curve can be easily modeled by a p-n diode in parallel with a shunt resistor (Fig. 5.16d). An eye guide (dashed line) is also plotted in Fig. 5.16c to indicate the I-V of the shunt resistor. The shunt path is attributed to the connecting layer since there is still a connecting layer.

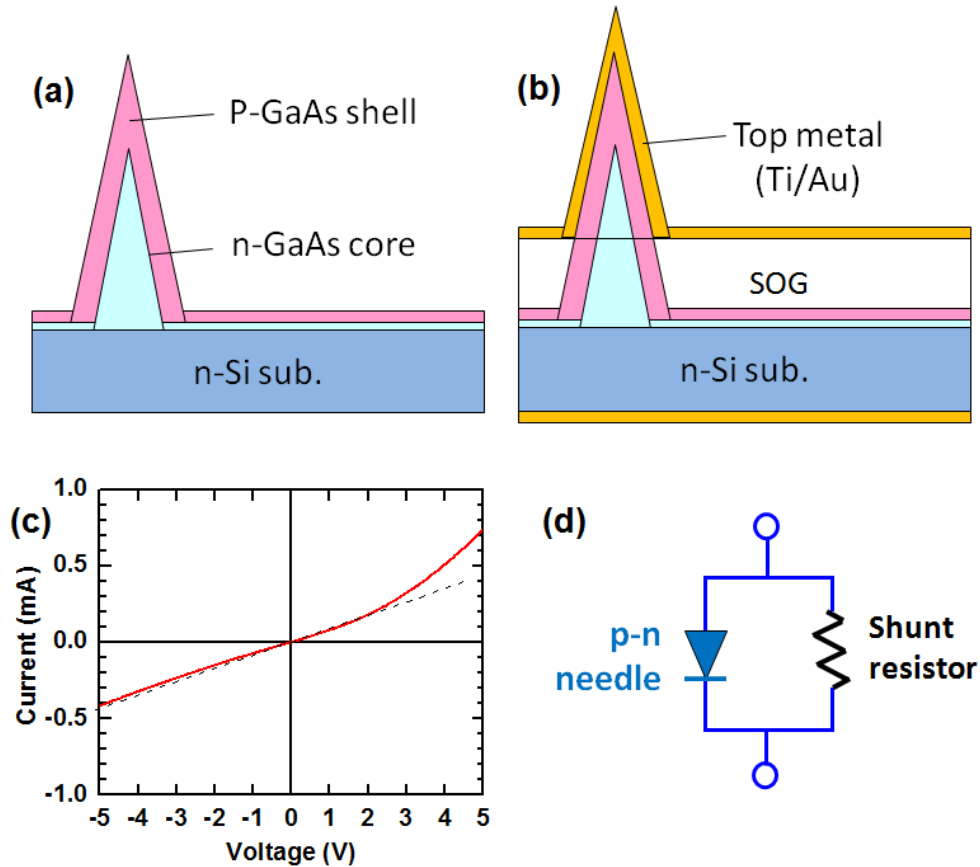


Figure 5.16 P-n junction inside a GaAs nanoneedle. (a) P-n GaAs nanoneedle growth design. The structure consists of an n-type, Si-doped core and a thin, p-type, Zn-doped shell on a n-type (111)Si. The accompanying growth of the connecting layer is also shown. (b) The test device structure after SOG filling and curing, and top and bottom metal deposition. (c) I-V curve of a p-n device. A “turn on” at ~2 V can be seen with a resistive shunt path, attributed to the connecting layer, shown by an eye guide (dashed line). (d) A circuit model for the device.

With the understanding that a connecting layer would cause leakage, physically removing or electrically isolating the bottom p-shell is needed to avoid the leakage. This would hence force the current to flow through the p-n junction inside a nanoneedle body. The schematic in Fig. 5.17 illustrates this device design. The bottom-part of the p-shell is removed by etching, with the removal of the p-poly-GaAs film simultaneously. The rectifying junction is hence placed inside a nanoneedle. The nanoneedle-substrate interface is just an ohmic junction.

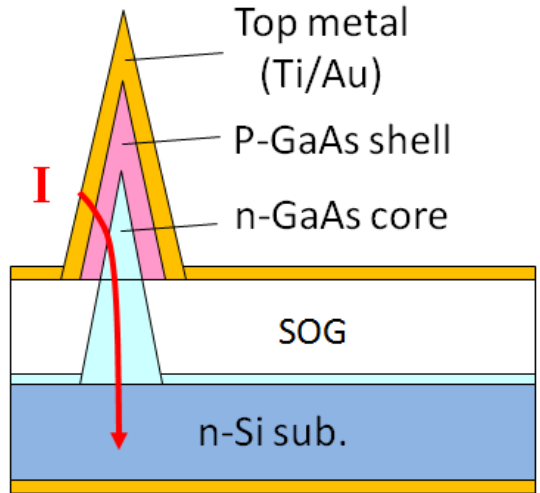


Figure 5.17 A nanoneedle p-n junction design with the connecting-layer leakage path removed. The bottom part of the p-type shell is etched away to force the current flow through the p-n junction inside a nanoneedle. The nanoneedle-substrate interface is just an ohmic junction.

After successfully removing the bottom p-shell region, an excellent p-n diode like curve with a very small reverse bias current can then be seen. The device schematic is shown in Fig. 5.18a and the corresponding I-V curve is shown in Fig. 5.18b. The device design, fabrication processes, and device characteristics of this kind of p-n GaAs nanoneedle device would be discussed in greater details in the next chapter, Chapter 6, in which a nanoneedle photodiode and a nanoneedle light emitting diode will be discussed.

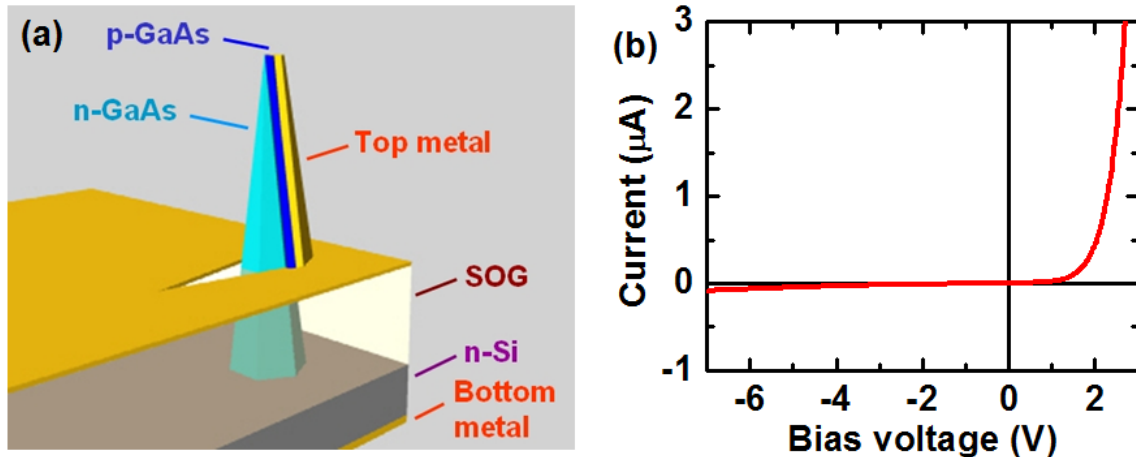


Figure 5.18 (a) Device schematic of a p-shell/n-core GaAs nanoneedle on a n-Si with the bottom p-shell etched away to isolate the leakage path. (b) The I-V of this device shows an excellent p-n diode like curve with a turn-on voltage ~ 1.5 V and a very small reverse bias current.

In conclusion, GaAs nanoneedles grown on Si were successfully doped to n-type with Si and Te, and p-type with Zn. The doping sources used were disilane, DETe, and DEZn. Both the Te and Zn dopings show higher than $10^{18}/\text{cm}^3$ doping levels, which will be suitable for typical electronic and optoelectronic devices. For lightly doped n-type GaAs nanoneedle up to $\sim 10^{17}/\text{cm}^3$, Si doping can also be used. We also have demonstrated a p-n junction inside a core-shell GaAs nanoneedle structure with excellent I-V characteristics. The process leading to this high quality device involves the isolation or removal of the connecting layer, which is a known current leakage path. Other electrical and optical properties of the nanoneedle p-n junction and other more complicated nanoneedle structure designs will be presented in the next chapter.

References:

- (1) Shimazu, M. *et al.* Silicon doping using disilane in low-pressure OMVPE of GaAs. *J. Cryst. Growth* **83**, 327-333 (1987).
- (2) Jain, S. C. & Roulston, D. J. A simple expression for band gap narrowing (BGN) in heavily doped Si, Ge, GaAs and $\text{Ge}_x\text{Si}_{1-x}$ strained layers. *Solid-St. Electron.* **34**, 453-465 (1991).
- (3) Hasegawa, H. *et al.* Dynamics and control of recombination process at semiconductor surfaces, interfaces and nano-structures. *Solar Energy* **80**, 629-644 (2006).
- (4) Hoke, W. E., Lemonias, P. J. & Korenstein, R. An examination of organometallic thermal stability and its relevance to low-temperature MOCVD growth of HgCdTe. *J. Mater. Res.* **3**, 329-334 (1988).
- (5) Houg, Y.-M., Low, T. S. Te doping of GaAs and $\text{Al}_x\text{Ga}_{1-x}\text{As}$ using diethyltellurium in low pressure OMVPE. *J. Cryst. Growth* **77**, 272-280 (1986).
- (6) Hudait, M. K., Modak, P., & Krupanidhi, S. B. Si incorporation and Burstein-Moss shift in n-type GaAs. *Mater. Sci. Eng., B* **56**, 1-11 (1999).
- (7) De-Sheng, J., Makita, Y., Ploog, K., Queisser, H. J. Electrical properties and photoluminescence of Te-doped GaAs grown by molecular beam epitaxy. *J. Appl. Phys.* **53**, 999-1006 (1982).
- (8) Hageman, P. R., de Croon, M. H. J. M., Tang, X., & Giling, L. J. Pressure and temperature dependence of Zn incorporation in metalorganic chemical vapour deposition grown GaAs and AlGaAs using diethylzinc as precursor. *J. Cryst. Growth* **129**, 281-288 (1993).
- (9) Rode, D. L. in *Semiconductors and Semimetals*, edited by R. K. Willardson and A. C. Beer, Vol. 10, Chap. 1 (Academic, New York, 1975)
- (10) Schubert, E. F., Goepfert, I. D., Grieshaber, W., & Redwing, J. M. Optical properties of Si-doped GaN. *Appl. Phys. Lett.* **71**, 921-923 (1997).
- (11) Waddill, G. D., Vitomirov, I. M., Aldao, C. M., & Weaver, J. H. Cluster Deposition on GaAs (110): Formation of Abrupt, Defect-Free Interfaces. *Phys. Rev. Lett.* **62**, 1568-1571 (1989).
- (12) Kenty, J. L. Physical vapor deposition of GaAs on single crystal sapphire. *J. Electron. Mater.* **2**, 239-254 (1973).
- (13) Gopal, V., Singh, S. K., & Mehra, R. M. Analysis of dark current contributions in mercury cadmium telluride junction diodes. *Infrared Phys. Technol.* **43**, 317-326 (2002).

Chapter 6:

InGaAs/GaAs Nanoneedles on Si for Photodetector and Light Emitting Diode Applications

With the capability of growing high-quality GaAs nanoneedles, GaAs/AlGaAs nanoneedles and InGaAs/GaAs quantum-well nanoneedles on Si (see Chapter 4), with the capability of doping the nanoneedles n-type or p-type (see Chapter 5), it is then possible to realize a p-n junction device on Si substrates. This will enable the heterogeneous integration of high-quality nanoneedle optoelectronic devices onto a Si CMOS platform.

In this chapter, I will show the epitaxial growth of a p-n, shell-core GaAs nanoneedle photodetector (PD) on Si. The nanoneedle PD shows a high current gain of 70 at a relatively low bias voltage of 10 V. Two possible gain mechanisms, avalanche multiplication and phototransistor gain, are discussed.

I will also present the preliminary results of a core-shell InGaAs/GaAs nanopillar light emitting diode (LED) on Si. A p-n diode-like I-V curve with a turn-on voltage at ~1 V and an L-I curve was measured. These results demonstrate the heterogeneous integration of high-quality III-V materials and devices onto Si via the novel nanoneedle growth mode.

6.1 GaAs-Based Nanoneedle Photodetectors on a Si Substrate

Fig. 6.1a shows a typical SEM picture of GaAs nanoneedles epitaxially grown on (111)Si by MOCVD. Details of the nanoneedle growth were described in Chapter 4.2. The nanoneedles are initiated by spontaneous clustering (catalyst-free) on a roughened surface and subsequently formed by a thin-film deposition-like process. Therefore, the nanoneedles grow in a core-shell mode. A high-resolution transmission electronic microscope (HRTEM) image of a nanoneedle tip is shown as the Fig. 6.1a inset. The narrow tip is with a radius of curvature of < 5 nm. On the other hand, the tapered nanoneedle shape results in a sub-micron wide base, ~600 nm in diameter, which makes nanoneedles robust enough to survive typical micro-fabrication processes, such as photolithography. The nanoneedle taper angle is measured $6-9^\circ$ which results in a needle shape with high aspect ratio. A TEM figure near the top portion of a nanoneedle is shown in Fig. 6.1b and no dislocation is seen. Fig. 6.1c is the Fast Fourier Transform (FFT) image of Fig. 6.1b. This diffraction pattern with $[\bar{1}\bar{2}10]$ zone axis shows that nanoneedles have a distinct pure wurtzite crystalline phase, in contrast to the typical zinc-blende phase for GaAs crystals. This is the only reported wurtzite GaAs material with bulk volume under typical epitaxial growth temperature and pressure.¹ The nanoneedle growth axis is along the wurtzite $[0001]$ direction therefore nanoneedles grow and align to the Si $\langle 111 \rangle$ direction and are vertical when being grown on a (111) Si substrate (Fig. 6.1a).² This vertical alignment facilitates the device fabrication. The unique wurtzite phase of these GaAs nanoneedle materials is further illustrated in Fig. 6.1d by overlaying the wurtzite ABABAB stacking schematics onto the HRTEM image. The overlay shows a good match.

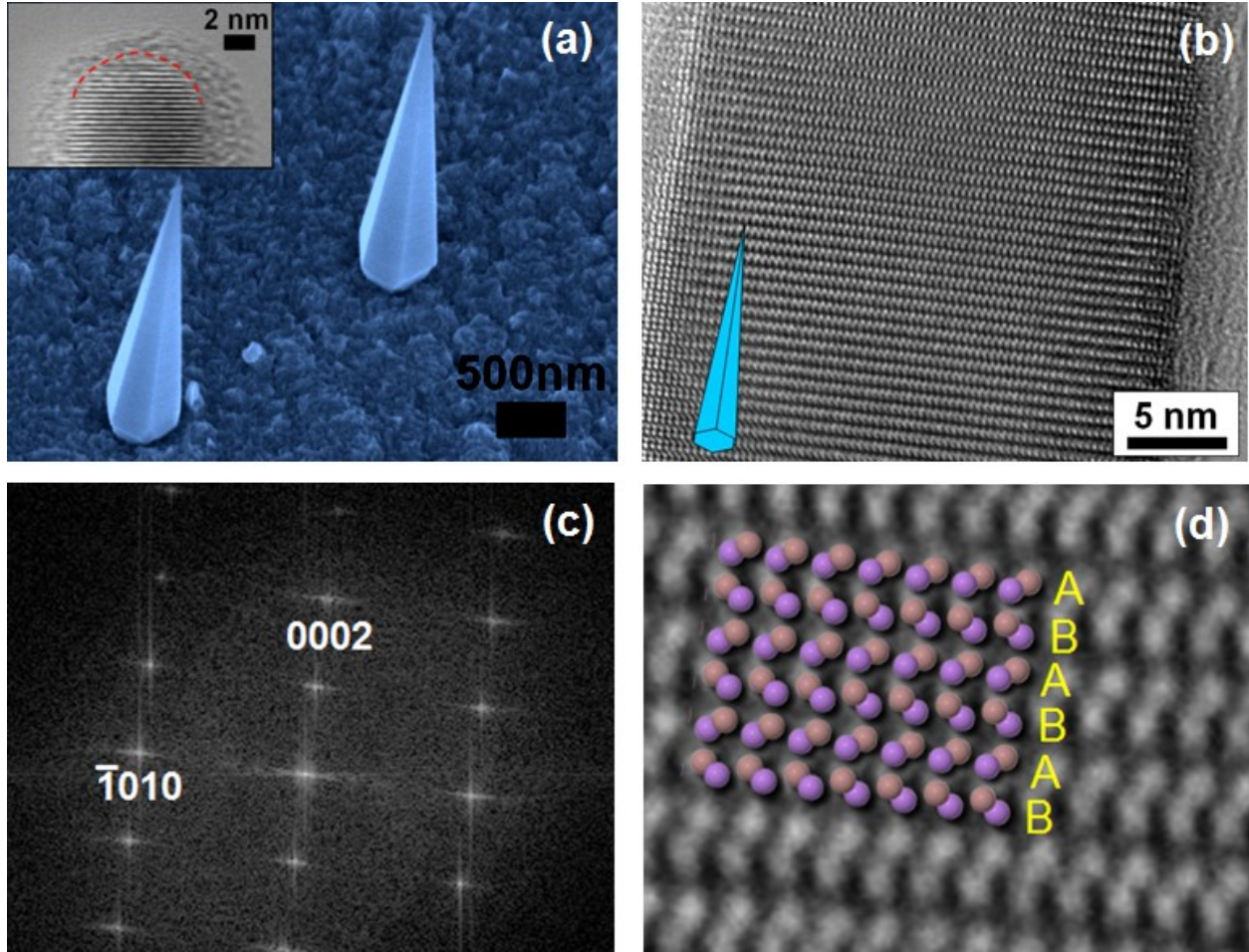


Figure 6.1 Structural characterization of GaAs nanoneedles grown on a (111) Si substrate. (a) 30°-tilt SEM image of as-grown nanoneedles. The nanoneedles are vertical to the substrate. Inset is a TEM image of a nanoneedle tip showing a radius of curvature smaller than 5 nm. The nanoneedle base is ~ 600 nm with a $\sim 7^\circ$ taper angle hence resulting in a needle-like high aspect ratio. (b) TEM of a nanoneedle. No dislocation is seen. (c) FFT image of the nanoneedle TEM image in (b) showing a pure wurtzite structure. The nanoneedle grows along the c -axis. (d) Overlay of a wurtzite ABABAB stacking schematics on the HRTEM image showing a perfect match. Zone axis is $[1\bar{2}10]$ for all the TEM images shown here.

With the core-shell nanoneedle growth mode, the fabrication of p-n nanoneedle PDs starts with the growth of p-shell (Zn doped, $\sim 10^{18}/\text{cm}^3$) / n-core (Si doped, $\sim 10^{17}/\text{cm}^3$) GaAs nanoneedles on an n-type (111) Si substrate ($\sim 10^{15}/\text{cm}^3$). The nominal nanoneedle core radius, shell thickness and height are 250 nm, 50 nm and 4 μm , respectively. We fabricated p-n PDs, schematically shown in Fig. 6.2a, using standard photolithography and metallization processes.

The PD fabrication process is described here. First a ~ 1.1 μm photoresist was spun onto an as-grown p-n nanoneedle wafer and then followed by a photoresist soft bake. An O_2 plasma ash

was performed to remove ~ 200 nm of the photoresist to ensure the protruding nanoneedle portion was free of photoresist residue. A thin Ti/Au film ($\sim 5/15$ nm) was then deposited onto only one side of the nanoneedles by a 30° angled deposition. The photoresist was then lifted off, leaving the metal film only on the upper portion of the nanoneedles. This Ti/Au film was then used as an etching mask to remove the bottom part of the p-type nanoneedle shell, which represents a current leakage path (see Chapter 5.4). This partial p-shell removal is illustrated in Fig. 6.2a. Spin-on-glass (SOG) with ~ 1.3 μm thickness was used to fill up the surrounding of the nanoneedles to provide a template for the top metal contact. SOG curing was done at 300°C for two hours with a 100°C/hr temperature ramping rate. A CF_4/O_2 plasma etch was performed to remove ~ 200 nm of the SOG to ensure that the protruding nanoneedle portion was free of SOG coverage. A photolithography step was then carried out to define the top p-metal regions, which are $200 \mu\text{m} \times 200 \mu\text{m}$ squares. A thicker Ti/Au film ($\sim 10/120$ nm) was then deposited (also with a 30° tilt), onto the previous thin metal on nanoneedles and onto the SOG surface, as the top p-metal contact. A photoresist lift off was done to complete the p-metal contact definition. N-metal contact was fabricated at the entire backside of the n-Si substrate.

Each PD device is defined by the top p-metal contact, which is a $200 \mu\text{m} \times 200 \mu\text{m}$ square. Considering the nanoneedle density, each device typically contains 30-50 nanoneedles. It is worthwhile to mention that one side of the nanoneedles was intentionally left uncoated for optical coupling. This was done by keeping all the metal deposition processes at a 30° -tilt angle. An SEM image of a single nanoneedle in an as-fabricated device is shown in Fig. 6.2b. Due to the angled metal depositions and the nanoneedle shadowing effect, a triangular area on the SOG surface next to each nanoneedle has no metal coverage. Light can also couple into a device through this triangular opening as it will be further discussed shortly.

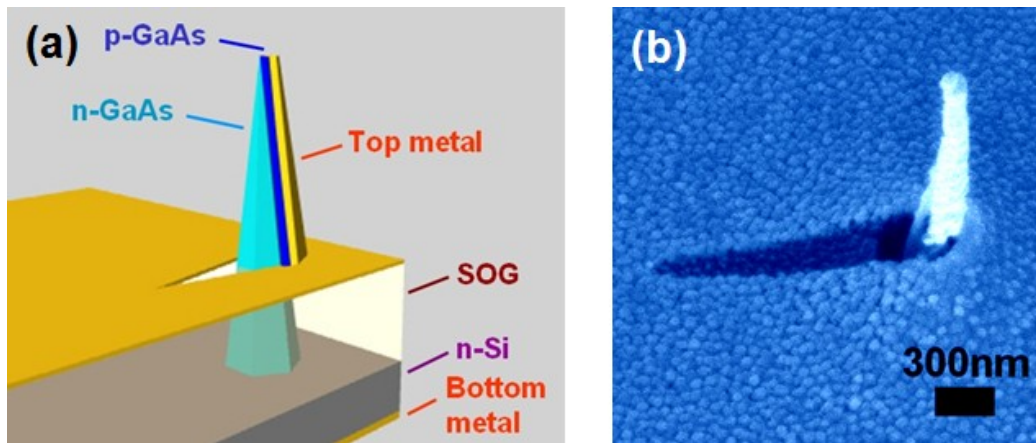


Figure 6.2 Nanoneedle PD device schematic and SEM image. (a) A nanoneedle PD device schematic. Each device is defined by a $200 \mu\text{m} \times 200 \mu\text{m}$ top p-metal contact and consists of 30-50 p-n GaAs nanoneedles on an n-type Si substrate. One side of the nanoneedles is intentionally left uncoated with metal for optical coupling. (b) 30° -tilt SEM image of a single nanoneedle in an as-fabricated PD device.

Device characteristics of the nanoneedle PDs were then carried out at room temperature. Fig. 6.3a shows the dark and light I-V characteristics of a nanoneedle PD under an 850 nm

illumination. The illumination spot size was approximately 200 μm in diameter and was carefully adjusted to be totally confined within the top 200 μm x 200 μm p-metal contact area. This ensured that light was only coupling into the device through the uncoated sides of the nanoneedle and the adjacent triangular openings shown in Fig. 6.2b. The dark I-V resembles a typical rectifying p-n diode I-V curve with a sharp turn-on at ~ 1.5 V. A reasonably small reverse-bias dark current is seen up to -5 V and followed by a breakdown at -11 V. The photocurrent of the nanoneedle PD, defined as the difference between the dark current and the current under illumination, increases with the reverse bias voltage and is shown in Fig. 6.3b. The photocurrent has two slopes as indicated by the dashed eye guide. This slope change at ~ 1.5 V suggests that the device might cross different operation regimes as bias voltage increases, such as that of a phototransistor. Details will be discussed shortly. The external quantum efficiency (QE) of the device can be calculated from

$$\eta_{ex} = \frac{I_p}{q\Phi_{ph}A_e} \quad (6.1)$$

where I_p is the photocurrent, q is the electron charge, Φ_{ph} is the incident photon flux, and A_e is the estimated exposed (non-metalized) area of the device. The external QE of this device under the 850 nm illumination is also shown in Fig. 6.3b. At -10 V bias, the external QE of this nanoneedle PD was as high as 3,280%, or 32.8, showing a current gain.

The breakdown mechanism at -11 V was investigated. Temperature-dependent dark I-V characterizations were done as shown in Fig. 6.3c. First of all, the dark current increases with the temperature since typical dark current components such as diffusion current and band-to-band tunneling current both have this temperature dependence.³ However, the dark I-Vs for different temperatures intersect at the breakdown voltage of -11V. This intersection means that the absolute value of the breakdown voltage must be increasing with the temperature so the I-V curves cross each other. Such a temperature dependence of the breakdown voltage indicates avalanche effect as the breakdown mechanism.⁴ The possible current gain mechanism via avalanche multiplication will be discussed shortly.

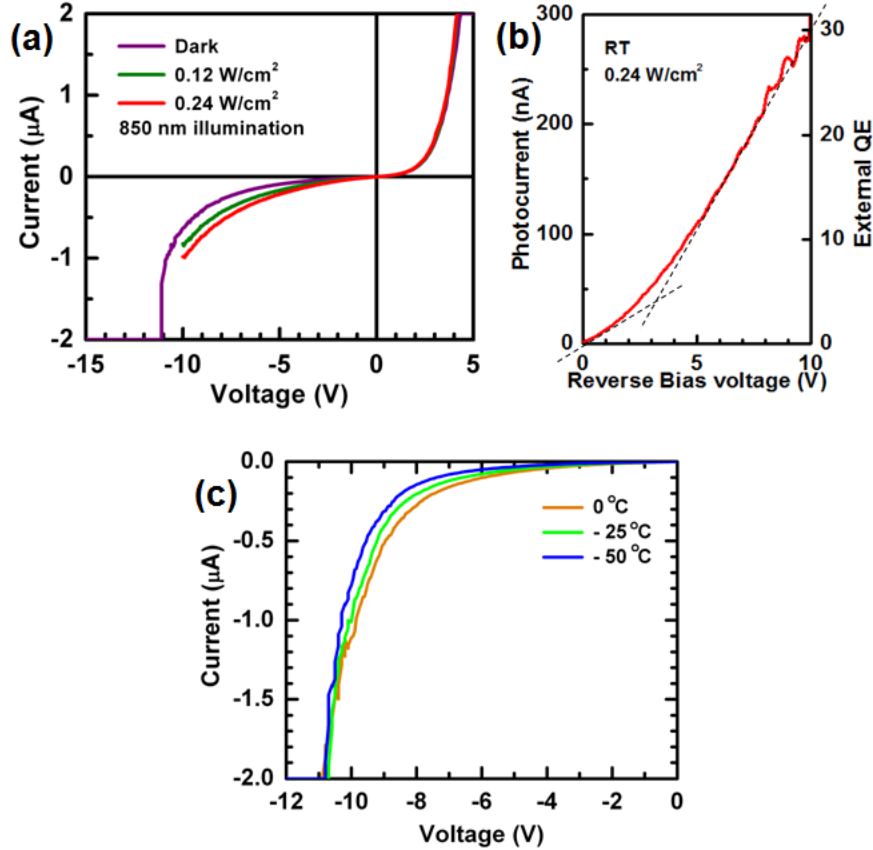


Figure 6.3 Nanoneedle PD electrical characterizations. (a) Dark and light I-Vs of a nanoneedle PD. The illumination wavelength is 850 nm with two irradiances, 0.12 and 0.24 W/cm². (b) Photocurrent versus reverse bias voltage for the 0.24 W/cm² illumination. The external QE is also shown. The external QE is 3,280% at -10 V bias. (c) Temperature-dependent dark I-V at the reversion bias region. The dark I-V for 0°C, -25°C and -50°C intersect each other at the breakdown voltage indicating the avalanche breakdown mechanism.

Fig. 6.4a shows the photocurrent of a nanoneedle PD device as a function of irradiance for various wavelengths. The device was biased at -10 V. A linear dependence is seen for all the wavelengths for the irradiance range tested here, indicating the device was operated at the low-injection regime. The finite (non-zero) response below the GaAs-band gap (> 870 nm) and the nearly zero response at 1200 nm match the Si band gap characteristics. This indicates that, in addition to the GaAs nanoneedles, the Si substrate also participates in the light absorption. The external QE as a function of illumination wavelengths is calculated and shown in Fig. 6.4b. Area considered in the calculation of the total incident power is the sum of all the triangular no-gold openings at each nanoneedle site (Fig. 6.2b) since both the GaAs nanoneedle and Si substrate absorb light. The external QE's for a typical Si and a GaAs detector (enlarged 50 times) are also plotted for comparison. The long-wavelength portion (980–1200 nm) of the external QE plot resembles a typical Si PD as expected and as explained above. That the external QE peaks at 850 nm and rolls off at 633 nm well resembles the feature for a GaAs PD, but could also fit the Si PD spectrum. It is believed that both the GaAs nanoneedles and Si substrate contribute to the photocurrent for this middle wavelength regime.

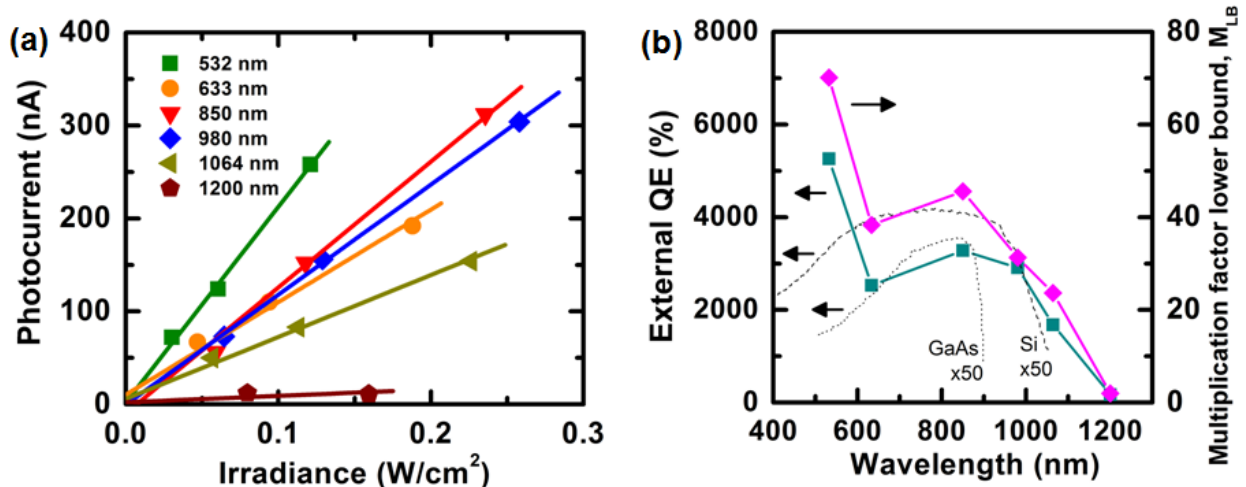


Figure 6.4 Illumination wavelength dependence on photoresponse for a nanoneedle PD. (a) Photocurrent as a function of irradiance for various wavelengths. The below-GaAs-bandgap absorption (> 870 nm) and nearly zero 1200 nm response implying that, in addition to the GaAs nanoneedles, the Si substrate also participates in the light absorption. (b) External QE and experimental multiplication factor lower bound ($M_{ex, LB}$, see text for explanation) as a function of wavelength. The external QE for the 532 nm illumination has a jump which implies additional current multiplication mechanisms which might be the emission of Auger electrons and/or direct generation of multiexcitons. The QE's (enlarged by 50 times) for a typical Si PD and a GaAs PD are also plotted here for comparison.

Going towards shorter wavelength, we observed an external QE jump for the 532 nm illumination. This is particularly interesting since a 532 nm photon has an energy (2.33 eV) which is more than twice of that of the Si bandgap (1.12 eV). This external QE jump might suggest an emission of Auger electron and/or direct generation of multiexcitons (two in this case) due to this higher than 2x Si-bandgap-energy photon.⁵ These mechanisms might also contribute to the current gain and require further investigation.

The external QE η_{ex} can be expressed as,

$$\eta_{ex} = (1 - R)\eta_i M \quad (6.2)$$

where R is the device reflectivity, η_i is the internal QE and M is the current multiplication factor. Since the device reflectivity R , which is the reflectivity of the SOG/Si layer, can be calculated for each illumination wavelength (Table 6.1), the $\eta_i M$ product can be extracted from the external QE. Considering the largest possible η_i value of 1, the experimental lower bound of M , $M_{ex, LB}$, was obtained and also plotted in Fig. 6.4b. For the 532 nm illumination, the external QE is 5260% and its multiplication factor lower bound $M_{ex, LB}$ is 70.

Table 6.1 Reflectivity of the SOG/Si layer as a function of incident wavelength.

Wavelength (nm)	Reflectivity	Transmissivity
532	0.25	0.75
633	0.34	0.66
850	0.28	0.72
980	0.07	0.93
1064	0.29	0.71
1200	0.13	0.87

To understand the origin of the large M factor at such a small bias voltage (-10 V or less) we performed a three-dimensional device simulation using Sentaurus Device software. Since this -10 V bias voltage is close to the avalanche breakdown at -11 V, the possibility of the avalanche multiplication mechanism is first investigated. Fig. 6.5a shows the electric field distribution inside a nanoneedle PD device at a -10 V bias. Regions with electric field greater the breakdown field (4.5×10^5 V/cm) are clearly seen, which should contribute to the impact ionization hence the current multiplication. The electron multiplication factor M_n and the hole multiplication M_p are calculated along the integration path shown in Fig. 6.5a and plotted in Fig. 6.5b. What are also plotted in Fig. 6.5b are the experimental current multiplication factor lower bound ($M_{ex, LB}$) for the 532 nm & 850 nm illuminations. It is thought that the hole multiplication factor M_p , but not the electron multiplication factor M_n , dominates the multiplication process and accounts for the overall M . This is because the high field region is located at the p-n junction, which is directly under the metal-coated nanoneedle sidewall. This location is shielded from incident photons, so photocarriers are not generated in this high-field region. Instead, photocarriers are generated in the low-field, uncoated half of the nanoneedle and in the Si under the triangular opening discussed previously. As a consequence, the nanoneedle PD might act as a separate absorption and multiplication APD which injects only holes into the high-field multiplication region.⁶ A simulated M_p of 32 at -10 V bias is close to the experimental data. The small nanoneedle cross-section dimension and hence the highly-curved cylinder-like p-n junction shape is thought to enhance the electric field via the lighting rod effect. The electric field enhancement and therefore the breakdown voltage reduction of a cylindrical or spherical p-n junction are discussed in details by Ghandhi *et al.*⁷

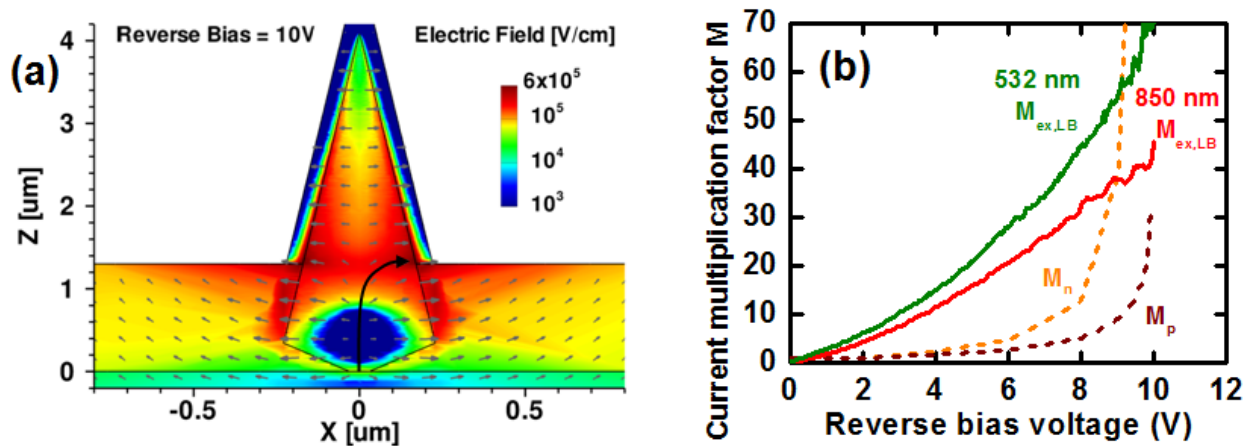


Figure 6.5 Avalanche gain model of for a nanoneedle PD. (a) Electric field distribution inside a nanoneedle PD device at a -10 V bias. Regions with electric field greater the breakdown field (4.5×10^5 V/cm) are seen as the dark-red areas, which contribute to the impact ionization hence the current multiplication. A path for calculating the electron and hole multiplication factors (M_n and M_p) is also shown here. (b) Comparison of the simulated M_n and M_p to the experimental M lower bounds for the 532 nm and 850 nm illuminations.

The avalanche multiplication model, however, cannot well explain the high current gain seen at smaller bias voltages. Another gain mechanism is needed especially for describing the small bias voltage conditions. The ~ 1.5 V kink in photocurrent-voltage curve shown in Fig. 6.3b might imply the turning point of the saturation regime and the forward-active regime for a phototransistor. A phototransistor model is hence analyzed here. The large slope between 1.5 V and 10 V in Fig. 6.3b can be attributed to a very large Early effect, with some calculations to be shown shortly. The band diagram of the nanoneedle PD device in Fig. 6.5a, along the nanoneedle central axis ($x = 0$), is shown in Fig. 6.6a. The band diagram strongly resembles that of a pnp transistor although the nanoneedle PD shown here is actually an n⁺np structure. The very lightly doped n-type Si substrate ($\sim 10^{15}/\text{cm}^3$) here takes the role of a p-type emitter for a regular pnp transistor.⁸ The photogenerated holes in the n-Si region would flow to and accumulate at the Si/GaAs junction due to the valence band slope in the n-Si region and the hole potential barrier at the Si/GaAs interface. The accumulated holes are believed to “photo-dope” the lightly-doped n-Si region into p-type for sufficient hole emission.⁹ The n-type GaAs nanoneedle core is the base ($\sim 10^{17}/\text{cm}^3$) and the p-type GaAs shell ($\sim 10^{18}/\text{cm}^3$) is the collector. Photogenerated holes are being injected from the n-Si side and collected at the p-GaAs shell en route the n-GaAs base. The pnp-like structure traps electrons in the base region hence providing the control of emitter-base junction voltage via illumination, which is essentially the operation principle of a phototransistor.¹⁰ The phototransistor gain β can be estimated as,

$$\beta = \frac{\tau_p}{\tau_n} \quad (6.3)$$

where τ_p is the minority carrier lifetime in the base (hole lifetime in this case) and τ_r is the base transit time.¹¹ Base transit time can be estimated as the time diffusing through the neutral base region since the drift velocity is much faster than the diffusion velocity so the time spent in the depletion regions (corresponding to drift carrier transport) can be neglected. τ_r is then given by,

$$\tau_r = \frac{w'_B{}^2}{2D_{p,B}} \quad (6.4)$$

where w'_B is the neutral base width and $D_{p,B}$ is hole diffusion constant. Using $\tau_p \sim 10$ ns,¹² $D_{p,B} = 10$ cm²/s, and w'_B from our device simulation, the phototransistor gain β as a function of reverse bias voltage is plotted in Fig. 6.6b. For comparison, the experimental phototransistor gain is calculated as follows. Since only the photogenerated current in the base region would be amplified with a phototransistor gain, the current equation should take the following form,

$$\frac{4}{5}I_{po} + \frac{1}{5}I_{po}\beta = I_p = I_{po}M \quad (6.5)$$

where 4/5 and 1/5 come from the fact that the absorption area ratio for the n-Si “emitter” region to the n-GaAs “base” region is 4:1. I_{po} is the unamplified photogenerated current, β is the phototransistor gain, I_p the measured total photocurrent, and M is the current multiplication factor defined earlier. Rewriting equation (6.5) yields a β and M relationship as,

$$\beta = 5M - 4 \quad (6.6)$$

The experimental phototransistor gain for 532 nm and 850 nm illumination is then calculated from the experimental $M_{ex,LB}$ shown in Fig 6.5b, with equation (6.6) used, and plotted in Fig. 6.6b to compare to the simulated β . Since again the $M_{ex,LB}$ is a lower bound (by assuming internal QE equal to one) of the actual M , the calculated phototransistor gain would also be a lower bound of the actual value and herein defined as $\beta_{ex,LB}$ to avoid confusion. The experimental $\beta_{ex,LB}$ and the simulated β show good agreement as seen in Fig. 6.6b. Considering this $\beta_{ex,LB}$ is only the lower bound, the actual gain could be even closer to the simulated value. The phototransistor gain for less than 2 V reverse bias is not discussed since the phototransistor device is still in the saturation region and would not provide gain.

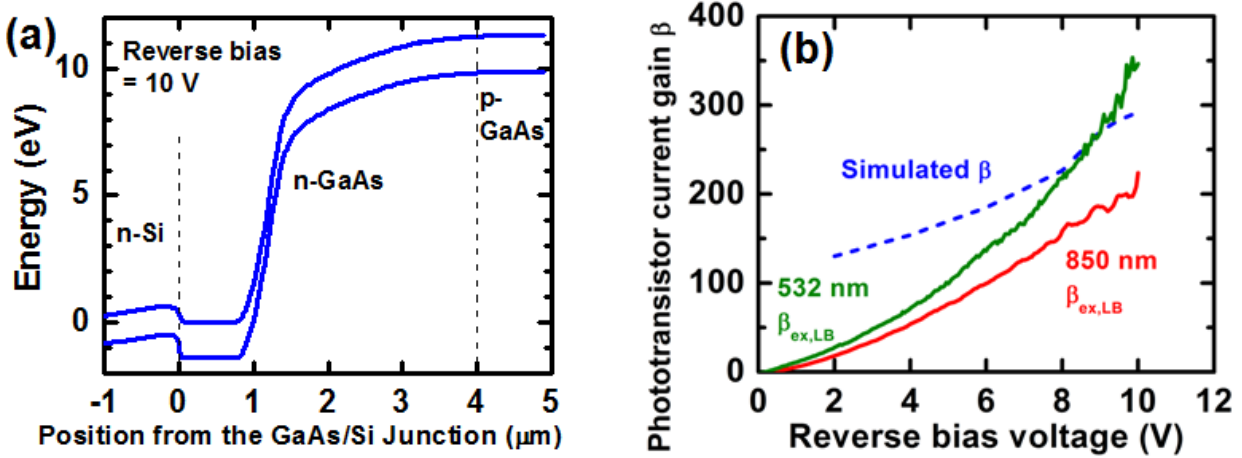


Figure 6.6 Phototransistor model for a nanoneedle PD. (a) Band diagram of a nanoneedle PD along the nanoneedle axis. The n⁻-Si/n-GaAs/p-GaAs band diagram resembles that of a pnp transistor. (b) Comparison of the simulated phototransistor gain β and the experimental phototransistor gain lower bound $\beta_{ex,LB}$. The experimental gain follows the slope of the simulated phototransistor gain β quite well.

In short, the phototransistor model seems to fit the experimental data better. However, it is possible that both the phototransistor gain and avalanche gain, as well as other gain mechanisms, exist simultaneously. Further investigations are still needed to fully explain the large current gain observed.

6.2 GaAs/InGaAs Quantum-Well-Based Nanoneedle Light Emitting Diodes on a Si Substrate

A more complicated nanoneedle structure with AlGaAs surface passivation was studied for light emitting applications since light emission is prone to non-radiative recombination centers such as the surface states of GaAs. Fig. 6.7a is the designed nanoneedle LED growth structure with InGaAs quantum well (QW) and GaAs barriers with AlGaAs surface passivation. The growth starts with a sharp n-type (Te-doped) GaAs nanoneedle core epitaxially grown on an n⁺-(111) Si substrate. An i-GaAs inner barrier is deposited onto the nanoneedle core, resulting an i-GaAs shell/n-GaAs core sharp nanoneedle structure. Subsequently, a nominal 8.5 nm In_{0.3}Ga_{0.7}As QW is deposited onto the nanoneedle structure, which stops the vertical growth due to the high indium composition transforming the sharp nanoneedle to a flat-top pillar, referred herein as a nanopillar. All the subsequent layers are grown in the lateral direction with very minimum growth on the top plane. An outer i-GaAs barrier, a p-Al_{0.2}Ga_{0.8}As cladding and a p-GaAs contact layer are then deposited for the final nanopillar LED structure. Zn is used as the p-type dopant. Both the n- and p-type doping levels are in the $\sim 10^{18}/\text{cm}^3$ range. The as-grown nanopillar LED structures are shown in Fig. 6.7b for both the 30°-tilt view and the top-down view. The nanopillar dimensions are very close to the designed values indicating the stable and highly controllable nanoneedle-based growth mode, even for this complicated heterostructure. All the

nanopillars indeed show a flat top indicating that the nanoneedle vertical growth is perturbed by the $\text{In}_{0.3}\text{Ga}_{0.7}\text{As}$. This vertical growth interference was discussed in detail in Chapter 4.5. Hexagonal cross sections are still clearly seen for these nanopillars indicating that the lateral growth is not affected by the introduction of $\text{In}_{0.3}\text{Ga}_{0.7}\text{As}$.

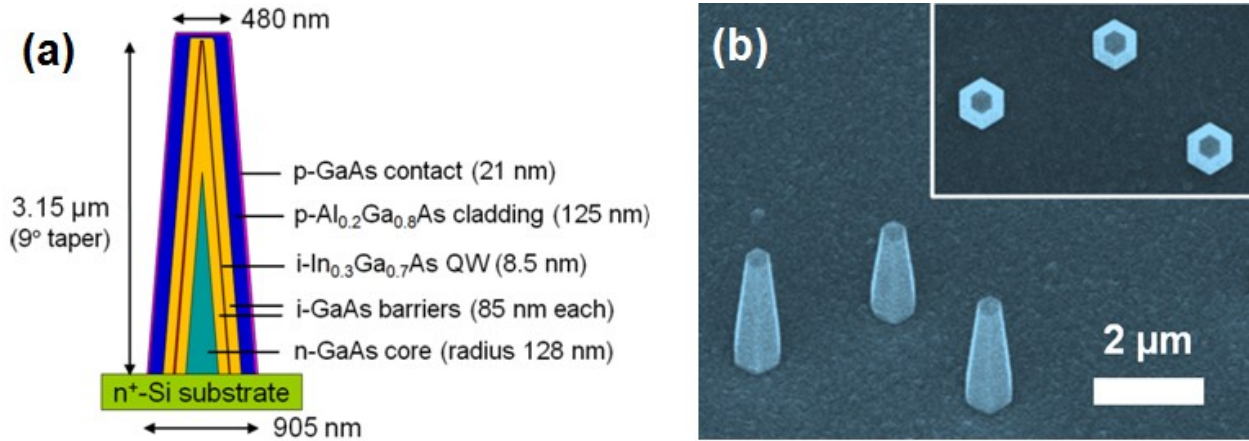


Figure 6.7 (a) Nanopillar LED growth structure design. The structure consists of a sharp n-GaAs nanoneedle core and a sharp i-GaAs inner nanoneedle barrier. The i- $\text{In}_{0.3}\text{Ga}_{0.7}\text{As}$ QW then stops the nanoneedle vertical growth and makes the rest of the growth only in the lateral direction. This results in a flat-top nanopillar structure. The outer i-GaAs barrier, a p- $\text{Al}_{0.2}\text{Ga}_{0.8}\text{As}$ cladding and a final p-GaAs contact were all grown only in the lateral direction with very minimum top c-plane deposition. (b) 30°-tilt SEM image of as-grown nanopillar LED structures. Inset is the top-down view. Hexagonal nanopillar cross sections are clearly seen. The dimensions of the nanopillars are close to the design.

The room-temperature $\mu\text{-PL}$ spectra of an undoped as-grown nanopillar LED structure are shown in Fig. 6.8a in wavelength scale. This control sample is with exactly the same dimensions as those shown in Fig. 6.7a except that all the dopants are taken away. This is because the presence of the Te and Zn dopants would affect the wavelength determination of the QW, as the dopant-related PLs shown in Chapter 5. The InGaAs/GaAs QW in this nanopillar control sample shows a very bright emission at ~ 1142 nm, which is close to the designed wavelength. The same spectra are shown again in energy scale in Fig. 6.8b. The FWHM of the 100 μW pumping peak is only 83 meV, at room temperature, which testifies the excellent QW material quality. This PL FWHM is comparable to the state-of-the-art thin-film QW structures measured at room temperature.

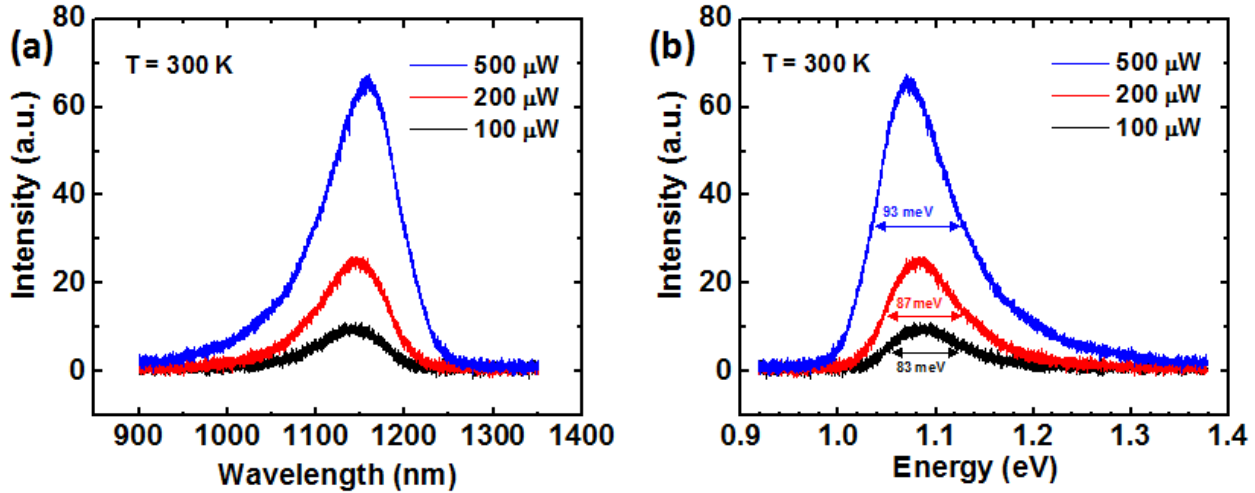


Figure 6.8 As-grown, undoped nanopillar LED μ -PL spectra. (a) Shown in wavelength scale. The peak wavelength at ~ 1142 nm is close to the design. (b) Shown in energy scale. The FWHM is a narrow 83 meV for the 100 μ W excitation testifying excellent material and QW qualities.

The nanopillar LED devices were fabricated with the same processes of those of the nanoneedle PDs. The p-GaAs contact layer and the p-AlGaAs cladding layer near the bottom of the nanopillar structure were again etched away to remove this current leakage path. The timed etch stopped at the outer i-GaAs barrier to leave a proper passivation for the InGaAs QW. SOG was again used to planarize the device. One major difference to the PD devices is that the nanopillars for LEDs were intentionally placed under a long, thin ($500 \mu\text{m} \times 10 \mu\text{m}$) contact metal finger as shown in the inset of Fig. 6.9a instead of under a $200 \mu\text{m} \times 200 \mu\text{m}$ square probing pad as the case for the PD. The reason for this design change is the following. For an LED, scattered light is desired so minimizing the top contact metal size is necessary. For a PD, we wanted to maximize the nanoneedle contribution but not the Si substrate contribution hence we covered most of the PD device area by metal and left only a small opening at each nanoneedle site.

Fig. 6.9a shows the room-temperature I-V characteristics of a nanopillar LED. The device has a long metal finger extending into the region where nanopillars grow (black region seen in the inset) and contacted ~ 15 nanopillars as estimated under the optical microscope. The I-V resembles that of a p-n rectifying junction with a turn-on voltage at ~ 1 V. The device has a small breakdown at ~ -5 V probably due to the very thin undoped layers. For the L-I measurement, a Si APD operated in the Geiger mode was used to measure the power. The L-I curve (Fig. 6.9b) shows a linear dependence. It is worthwhile to mention that the Si APD should have nearly zero efficiency in picking up the signal at the QW wavelength of ~ 1142 nm. Therefore, what was shown in Fig. 6.9b was supposed to be the emission from the GaAs barriers due to the overspilled carriers from the InGaAs QW. As a consequence, the real QW emission should have been much brighter than what the APD picked up in the current case if an InGaAs APD were used. The collection of an electroluminescence spectrum using an InGaAs detector is now underway.

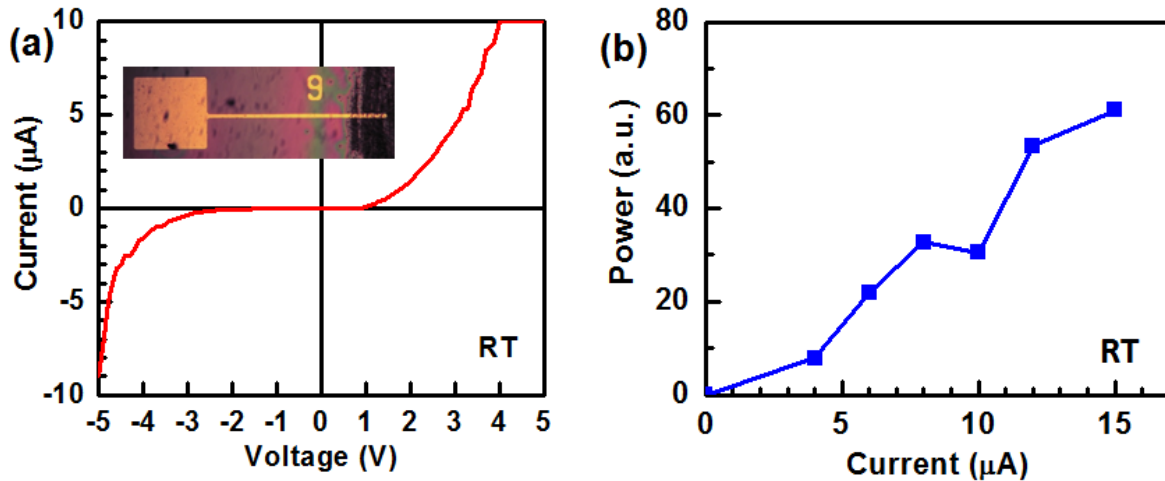


Figure 6.9 Nanopillar LED device characterization. (a) I-V characteristics of a nanopillar LED device containing ~ 15 nanopillars. Inset is the optical microscope image of the device. The device has a $200\ \mu\text{m} \times 200\ \mu\text{m}$ probing pad and a long $10\ \mu\text{m}$ -wide finger. The nanopillars are grown near the end of the metal finger (black region). (b) Room-temperature L-I curve collected with a Si APD operated in the Geiger mode. A linear L-I dependence is seen.

In conclusion, we present wurtzite phase, shell-core p-n GaAs nanoneedles epitaxially grown on an n-type (111) Si substrate. The growth was done at a CMOS-compatible growth temperature of 400°C . Nanoneedle PDs were then fabricated using standard micro-fabrication processes. A current gain is seen. The nanoneedle PD shows a high current gain of 70 at a relatively low bias voltage of 10 V. Two possible gain mechanisms, avalanche multiplication and phototransistor gain, are discussed.

A core-shell $\text{In}_{0.3}\text{Ga}_{0.7}\text{As}/\text{GaAs}$ QW nanopillar LED structure with $\text{Al}_{0.2}\text{Ga}_{0.8}\text{As}$ cladding was also grown on an $\text{n}^+-(111)\text{Si}$ substrate via the novel nanoneedle growth mode. The room-temperature PL has an emission peak at $\sim 1142\ \text{nm}$ with a narrow FWHM of only 83 meV. The LED device shows a room-temperature I-V curve with $\sim 1\ \text{V}$ turn-on voltage and a linear L-I dependence. The capability of integrating III-V detectors and emitters on Si with the CMOS-compatible growth and processing conditions would enable important applications such as the on- or off-chip optical interconnects.

References:

- (1) McMahon, M. I. & Nemes, R. J., Observation of a wurtzite form of gallium arsenide. *Phys. Rev. Lett.* **95**, 215505 (2005).

- (2) Moewe, M., Chuang, L. C., Crankshaw, S., Chase, C., & Chang-Hasnain, C. Atomically sharp catalyst-free wurtzite GaAs/AlGaAs nanoneedles grown on silicon, *Appl. Phys. Lett.* **93**, 023116 (2008).
- (3) Blanks, D. K., Beck, J. D., Kinch, M. A., & Colombo, L. Band-to-band tunnel processes in HgCd-Te: Comparison of experimental and theoretical studies. *J. Vac. Sci. Technol. A* **6**, 2790-2794 (1988).
- (4) Sze, S. M. *Physics of Semiconductor Devices* (John Wiley & Sons, New York, 1981).
- (5) Bhardwaj, A., Balakrishnan, V. R., Srivastava, P. & Sehgal, H. K. Carrier multiplication in nanoparticle PbSe/single crystal Si heterojunctions. *Semicond. Sci. Technol.* **23**, 095020 (2008).
- (6) Nishida, K., Taguchi, K., & Matsumoto, Y. InGaAsP heterostructures avalanche photodiodes with high avalanche gain. *Appl. Phys. Lett.* **35**, 251-252 (1979).
- (7) Baliga, B. J. & Ghandhi, S. K. Analytical solutions for the breakdown voltage of abrupt cylindrical and spherical junctions. *Solid-State Electron.* **19**, 739-744 (1976).
- (8) Chuang, S. L. *Physics of Optoelectronic Devices* (John Wiley & Sons, New York, 1995)
- (9) Thunich, S. *et al.* Photocurrent and photoconductance properties of a GaAs nanowire. *Appl. Phys. Lett.* **95**, 083111 (2009).
- (10) Campbell, J. C., Dentai, A. G., Burrus, Jr., C. A., & Ferguson, J. F. InP/InGaAs heterojunction phototransistors. *IEEE J. Quantum Electron.* **QE17**, 264-269 (1981).
- (11) Zeghbroeck, B. V. *Principle of Semiconductor Devices*. Online at <http://ecee.colorado.edu/~bart/book/book/index.html>
- (12) Hwang, C. J. Doping dependence of hole lifetime in n-type GaAs. *J. Appl. Phys.* **42**, 4408-4413 (1971).

Chapter 7:

Wurtzite GaAs Nanoneedles Epitaxially Grown on 46% Lattice-mismatched Sapphire with Bright Luminescence

Heterogeneous integration of thin-film III-V materials onto non-III-V substrates has long been an important task for increasing the functionalities of III-V devices.¹ However, the large lattice mismatch between the III-V materials and the foreign substrate is one of the major issues for yielding high quality thin films.² Recently it has been shown that three-dimensional growth, such as the nanowires and nanoneedle discussed in the previous chapters, can accommodate lattice mismatch more effectively hence better material quality is expected.³⁻⁶ Here I will focus on discussing a unique case of the nanoneedle growth, the epitaxial GaAs nanoneedle growth with a very large 46% lattice mismatch to sapphire. I will show that the photoluminescence of these GaAs nanoneedles still show a narrow 18 meV linewidth, indicating an excellent crystal quality, despite of the 46% mismatch. A theoretical model is briefly mentioned showing that a very efficient relaxation of elastic stress on the sidewalls may favor the formation of coherent nanoneedles in highly mismatched material systems. Our results demonstrate a novel, catalyst-free method for growing high-quality, wurtzite (WZ) phase GaAs materials on sapphire.

7.1 Structural Properties of GaAs Nanoneedles Grown on Sapphire

GaAs thin film growth on sapphire substrates has been previously attempted.⁷⁻⁹ However, due to the large lattice mismatch between GaAs and sapphire, high dislocation density in the GaAs film is observed, and the electrical and optical properties are affected by the dislocations.

We report the GaAs nanoneedle growth on a sapphire substrate to overcome the lattice mismatch issue. The growth procedures and growth conditions were described in Chapter 4.2 hence is not repeated here. However, it is worthwhile to mention the pre-growth annealing process since this will be related to our later discussion. Prior to the growth, the substrate is annealed in-situ in the MOCVD reactor at a higher temperature, herein defined as the annealing temperature, for 3 minutes. This step is critical to the nanoneedle nucleation on a sapphire substrate and will be discussed shortly. Annealing temperatures of 400-650°C and nanoneedle growth temperatures of 385-415°C were tested in this experiment.

Fig. 7.1a shows the side view of GaAs nanoneedles spontaneously grown on a (0001) sapphire substrate with growth temperature of 400°C and annealing temperature of 606°C. The growth is catalyst free and no substrate surface treatment is needed to initiate the nanoneedle growth. This is different from the previously reported GaAs nanoneedles on Si, which requires substrate surface roughening prior to the growth.¹⁰ The majority of the nanoneedles are perpendicular to the substrate showing the epitaxial growth feature of GaAs nanoneedles on the sapphire substrate. The epitaxial growth is verified by the TEM analysis and will be discussed shortly. Fig. 7.1b shows a 30°-tilt SEM image of a GaAs nanoneedle with 82-minute growth

time. The sharp tip, submicron-wide base and smooth sidewall facets are observed. The nanoneedle taper angle is typically $11\pm 1^\circ$.

A top-down SEM image of a nanoneedle is shown in Fig. 7.1c. The hexagonal cross section corresponding to the 6 sidewall facets is clearly seen. It is observed that the GaAs nanoneedle in-plane orientation is rotated by 30° with respect to the sapphire substrate. The nanoneedle facet orientation is assigned via the TEM analysis and will be shown later. A similar 30° in-plane rotation is known for thin-film GaN grown on a sapphire substrate. This rotation is necessary to stack wurtzite (WZ) GaN onto sapphire with group III atoms, Al from sapphire and Ga from GaN, aligned at the 6 corners of a basal-plane unit cell.¹¹ The 30° in-plane rotation for GaAs-nanoneedles on sapphire is thought due the same reason since the GaAs nanoneedle crystalline structure is WZ. The lattice mismatch is calculated as 46% (compressive).

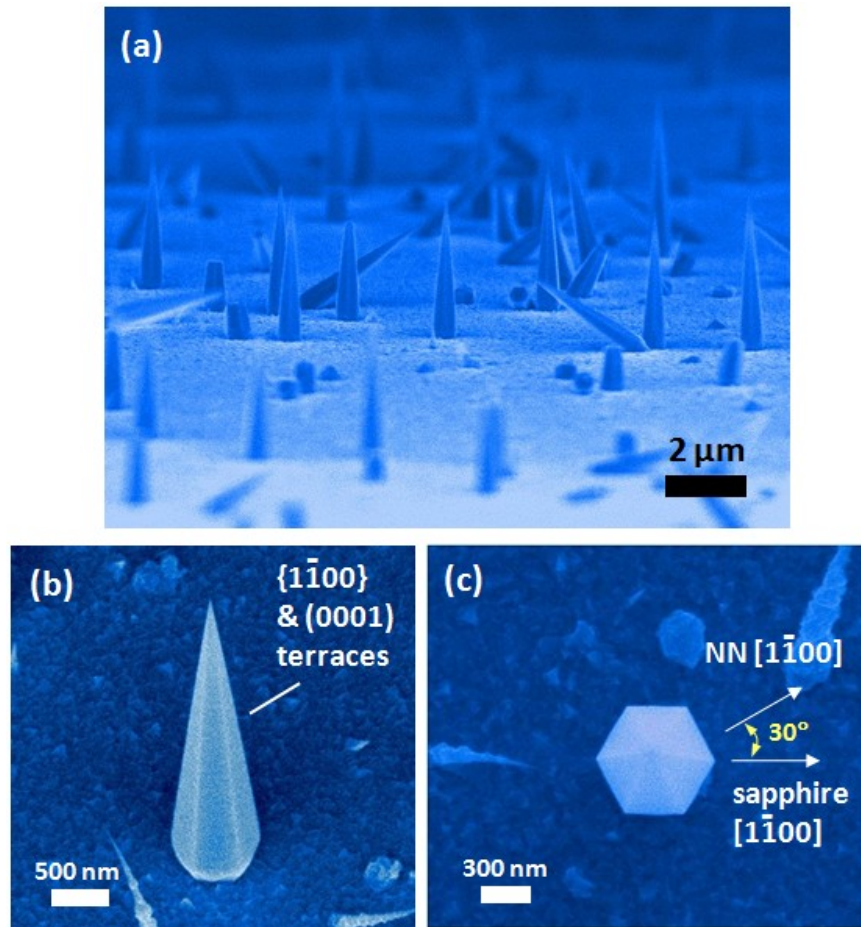


Figure 7.1 SEM images of GaAs nanoneedles grown on a sapphire substrate. (a) Side-view SEM image of as-grown nanoneedles. The nanoneedles are vertically aligned to the substrate indicating the epitaxial growth nature. (b) 30° -tilt SEM image of a nanoneedle. The sharp tip, submicron base, and smooth sidewall facets are seen. The sidewalls consist of $\{1\bar{1}00\}$ and (0001) terraces. (c) Top-down view of a nanoneedle showing a hexagonal cross section. The in-plane orientation of the nanoneedle shows a 30° rotation with respect to the sapphire substrate. This rotation is needed to stack a WZ GaAs crystal onto a c-plane sapphire substrate.

Several nanoneedles with different growth times ranging from 1.5 min to 180 min are shown in Fig. 7.2a for comparison. The sharp nanoneedle feature and the aspect ratio, hence the taper angle, are maintained even for the very short 1.5 min growth. A quantitative comparison is given as Fig. 7.2b. The inset shows the definition of the nanoneedle base diameter, length, and taper angle used throughout this paper. The nanoneedle base diameter increases linearly with growth time and the nanoneedle taper angle is maintained between 10-12°. This indicates that the nanoneedle growth starts with a nanoneedle seed nucleation and is then followed by a two-dimensional thin-film deposition on the preferred six sidewall facets. The nanoneedle growth mode is hence core-shell.¹⁰ The six tapered sidewall facets are essentially $\{1\bar{1}00\}$ surfaces with 5-6° tilt towards the $[0001]$ direction, for which the growth should mimic that on a 5-6° miscut $\{1\bar{1}00\}$ WZ GaAs substrate.

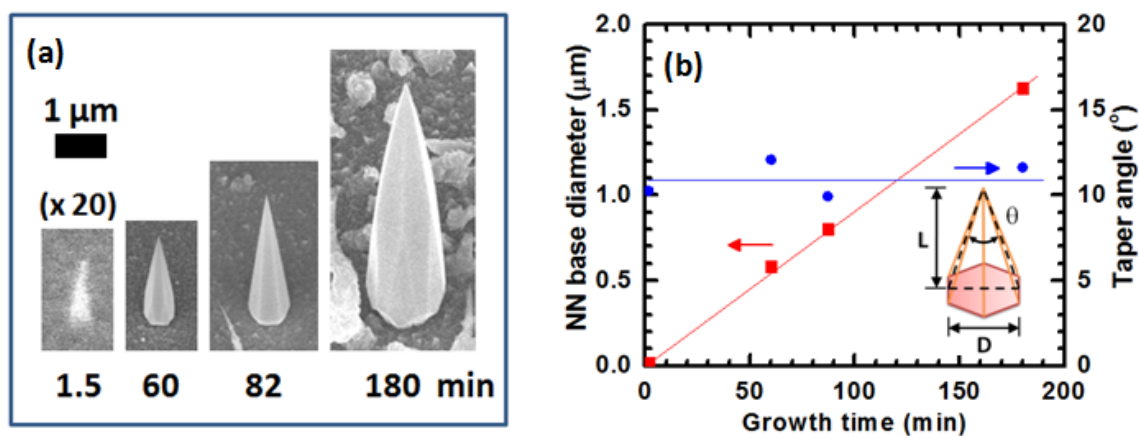


Figure 7.2 (a) 30°-tilt SEM images of nanoneedles with different growth times. The sharp nanoneedle feature is seen for all the nanoneedles shown here. The image of the nanoneedle with 1.5-min growth time is enlarged by 20x. (b) Nanoneedle base diameter and taper angle as a function of growth time. The diameter increase linearly with growth time and the taper angle is maintained between 10-12° indicating stable growth of the tilted $\{1\bar{1}00\}$ planes. Inset shows the definition of nanoneedle base diameter, length and taper angle.

A high-resolution TEM (HRTEM) image of a nanoneedle tip is shown in Fig. 7.3a. The nanoneedle tip diameter is narrower than 3 nm hence resembling a sharp needle feature. The Fast Fourier Transform of the TEM image (Fig. 7.3a inset) shows that the GaAs nanoneedle is with WZ structure, which is different from the common zinc-blend bulk GaAs structure. Bulk WZ GaAs has only been reported previously in powder form and is fabricated through a high pressure (~14 GPa) treatment.¹² Thin vapor-liquid-solid GaAs nanowires with 30-60 nm in diameter are also reported with WZ crystalline structure.¹³ The MOCVD GaAs nanoneedle growth reported in this work is the only known method of synthesizing WZ GaAs of bulk size at typical crystal growth temperature and pressure. The nanoneedle axis is here seen along the $[0001]$ direction and hence verifies the epitaxial growth on the c-sapphire substrate. The TEM

zone axis is $[1\bar{1}00]$ for this nanoneedle, which sat on one of its six sidewall facets on a carbon film for the TEM inspection. The nanoneedle taper is further investigated with the HRTEM image shown in Fig. 7.3b. Single atomic steps are clearly seen on the side of the nanoneedle which result in the taper. The taper sidewall facets are hence determined as made of $\{1\bar{1}00\}$ and (0001) terraces, as labeled in Fig. 7.1b. Fig. 7.3c shows the selective-area diffraction pattern of a nanoneedle sitting on its ridge on the carbon film. The diffraction pattern associated with this $[1\bar{2}10]$ zone axis is unique to WZ and hence it provides an unambiguous identification of the nanoneedle crystal structure as the WZ phase.

The WZ phase of the GaAs nanoneedles was further investigated with the micro-Raman (μ -Raman) scattering. An epitaxial GaAs nanoneedle grown on sapphire with 180-minute growth time (previously shown in Fig. 7.2a) was transferred and laid flat on a separate sapphire substrate for μ -Raman measurement. The excitation source is a tunable single-mode Ti:Sapphire ring laser. The laser spot was focused down to $\sim 2 \mu\text{m}$ to excite only one single nanoneedle at a time. A backscattering geometry was used which meant that the direction of the incident light \mathbf{k}_i is antiparallel to the collected scattered light, or $\mathbf{k}_s = -\mathbf{k}_i$. The x , y and z directions for the measurement is defined as the schematic shown in Fig. 7.3d. The polarization configuration can then be specified in the standard shorthand notation of Raman scattering measurements as $\mathbf{k}_i(\mathbf{e}_i \mathbf{e}_s)\mathbf{k}_s$, where \mathbf{e}_i and \mathbf{e}_s represent the polarization of the incident and scattered light. The different polarization configurations directly relate to the observable scattering lines governed by the form of the Raman tensor. A comparison of the μ -Raman spectra between the GaAs nanoneedle and a ZB epilayer is shown in Fig 7.3d. The solid lines are the multi-Lorentzian fits of the raw data, which is represented by the gray dots. The fresh-cut ZB epilayer shows a distinct SO phonon at 280 cm^{-1} in addition to its LO mode at 292.1 cm^{-1} and TO mode at 268.6 cm^{-1} . An SO contribution is also used to fit the polarized -x(z y)x and -x(zz)x GaAs nanoneedle spectra, which can be clearly seen having an additional line (labeled by a dashed line in Fig. 7.3d) compared to the ZB at 257.5 cm^{-1} attributable to a WZ E2 mode.¹⁴ This further verifies the high-quality, WZ crystalline phase for the GaAs nanoneedle s grown on a sapphire substrate. More details of the μ -Raman characterization for the GaAs nanoneedle s will be published elsewhere.

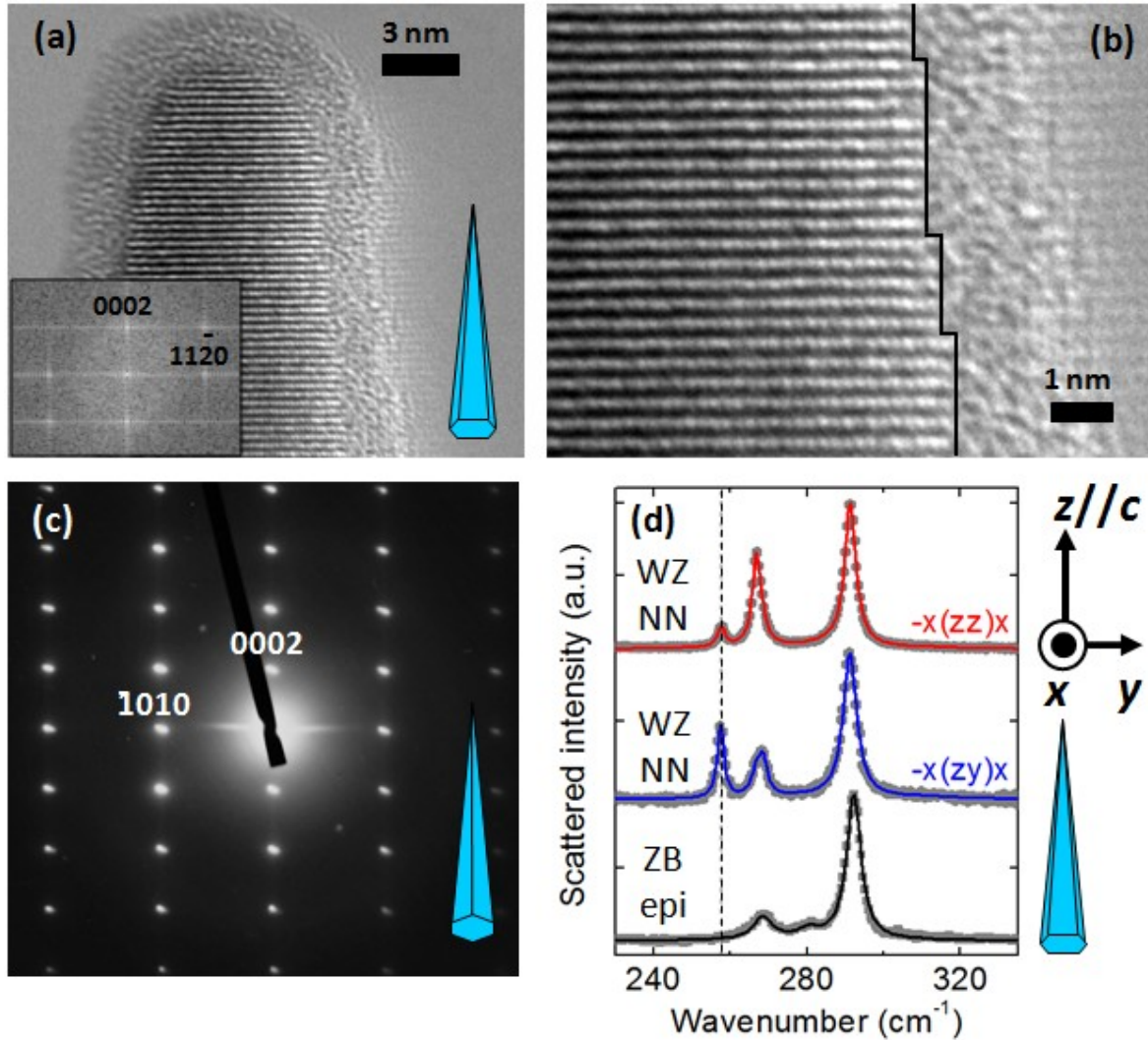


Figure 7.3 Nanoneedle HRTEM images and Raman scattering spectra. (a) Image showing a nanoneedle tip with less than 3nm tip diameter. Inset is the FFT image showing the WZ crystalline structure. The nanoneedle growth axis is $[0001]$ on a c -plane sapphire substrate verifying the epitaxial growth. Zone axis is $[1\bar{1}00]$ for this nanoneedle sitting on one of its 6 facets on the carbon film. (b) An HRTEM image showing that nanoneedle side consists of atomic steps which result in the taper of a nanoneedle. The tapered sidewall hence is determined consisting of $\{1\bar{1}00\}$ and (0001) terraces. (c) Selective-area diffraction pattern for a nanoneedle with $[1\bar{2}10]$ zone axis. The nanoneedle orientation is schematically shown. The diffraction pattern of this zone axis is unique to WZ hence it provides an unambiguous determination of the WZ crystal structure. (d) Backscattering spectra of a ZB GaAs epilayer and wurtzite GaAs nanoneedles at room temperature, each normalized to the intensity of its LO line and offset for clarity. Gray dots represent raw data, while the solid lines are multi-Lorentzian fits. The fresh-cut ZB epilayer shows a distinct SO phonon at 280 cm^{-1} in addition to its LO mode at 292.1 cm^{-1} and TO mode at 268.6 cm^{-1} . An SO contribution is also used to fit the polarized $-x(z\bar{y})x$ and $-x(z\bar{z})x$ WZ spectra, which have an additional line compared to the ZB at 257.5 cm^{-1} attributable to a WZ E2 mode (indicated by a dashed line).

V/III ratio is found critical for initiating the GaAs nanoneedle growth on a sapphire substrate. Fig. 7.4 shows the nanoneedle density as a function of V/III ratio, with the TEGa flow rate kept constant while varying the TBA flow rate. The nanoneedle density is higher than 10^6 cm^{-2} for V/III ratios between 48 and 72 and quickly drops by an order of magnitude when slightly outside this V/III ratio range. V/III ratios as 12 and 192 were also tested and resulted in no nanoneedles at all (not shown in this semi-log figure). At the low V/III ratio side between V/III ratios 12 and 48, the nanoneedle density increases with the V/III ratio. This positive dependence suggests the nanoneedle seed nucleation mode as the direct vapor-solid island formation with Ga_xAs_y -type cluster as the migration species. This refers to the vapor-solid island formation model for heteroepitaxy, for which the migrating cluster mass increases during the migration and eventually stops and forms an island.¹⁵ Higher V/III ratio, meaning more As, should result in a larger Ga_xAs_y -type cluster at all times therefore the cluster stops in a shorter migrating length and results in higher nanoneedle density. The driving force for the three-dimensional island formation instead of two-dimensional thin film growth could be the basic material property difference between GaAs and sapphire, such as lattice mismatch, which are commonly seen in the heterogeneous nucleation processes,^{15,16} and will be discussed later. At the high V/III ratio side between V/III ratios 72 and 192, the nanoneedle density drops as V/III ratio increases and eventually becomes zero for V/III = 192. This should be that high V/III ratio promotes thin-film growth and inhibits the island formation.¹⁶

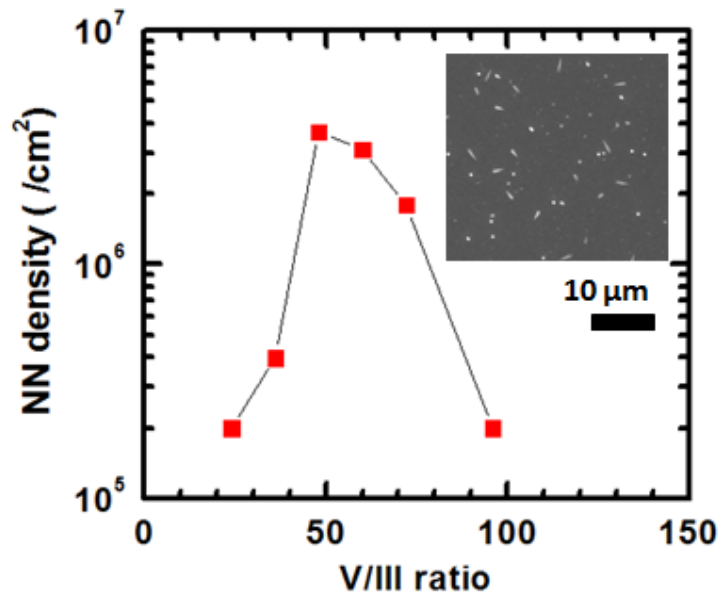


Figure 7.4 Nanoneedle density as a function of V/III ratio. V/III ratios 12 and 192 were also tested and resulted in no nanoneedles, therefore they were not shown on this semi-log plot. Between V/III ratios 12 and 48, the nanoneedle density increases with V/III ratio implying vapor-solid nanoneedle seed nucleation with the migrating species as Ga_xAs_y -type clusters. Inset shows the V/III = 48 sample.

The annealing temperature, with TBA present, also affects the nanoneedle density. For annealing temperatures 450°C and lower, nanoneedles were not found. However, annealing temperature does not affect the nanoneedle shape so it is only related to the nanoneedle nucleation stage. A run with high annealing temperature of 606°C but without TBA was found with no nanoneedle at all. This suggests that a high enough annealing temperature and the presence of TBA are both required for nucleating GaAs nanoneedle seeds on a sapphire substrate. Although the actual mechanism of how they help the nanoneedle seed nucleation still needs further investigation, a possible explanation is given below. It is thought that the annealing with TBA does the “arsenidation”, which replaces the oxygen by arsenic on the sapphire substrate surface and is similar to the nitridation process reported for the GaN or InN growth on sapphire.^{17,18} It has been shown that a nitridation temperature of 600°C or above could change the subsequent InN film property.¹⁷ Some nitridation conditions would result in substrate surface morphology change which promotes the 3D growth for subsequent layers.¹⁸

The growth temperature dependence of GaAs nanoneedles is also studied. Fig. 7.5a shows a nanoneedle with 415°C growth temperature. The nanoneedle growths for this growth temperature study were all with a 60-minute growth time. At this 15°C higher growth temperature, 6 more facets near the nanoneedle root, with 30° rotation to the upper 6 main $\{1\bar{1}00\}$ and (0001) terraces, are observed. These new set of facet are the $\{1\bar{2}10\}$ facets. No sharp nanoneedles are seen at this growth temperature. All the nanoneedles show a flat c-plane top surface. The formation of these additional facets should be corresponding to the formation of a Wulff shape, for which surface energy is minimized for a given volume.¹⁹ For a lower growth temperature of 385°C as shown in Fig. 7.5b, the sharp nanoneedle feature is maintained. The nanoneedle diameter, however, became 31% smaller than the 400°C nanoneedle while the nanoneedle length is about the same for these two growth temperatures. Therefore the taper angle of the 385°C nanoneedle is reduced to only 8°. On the other hand, although the 415°C growth did not result in sharp nanoneedles, a taper angle can still be defined and measured as 13°. The nanoneedle taper angle versus the growth temperature is shown in Fig. 7.5c. The nanoneedle taper angle decreases with decreasing growth temperature. This dependence can be well explained by the nanoneedle nucleation model and will be described shortly. Fig. 7.5c also shows the nanoneedle density as a function of growth temperature. The nanoneedle density is larger than $10^7/\text{cm}^2$ for the 385°C growth but drops by nearly two orders of magnitude when the temperature is 415°C, which is only 30°C higher. An explanation of this nanoneedle density change with temperature will also be given after the introduction of the theory.

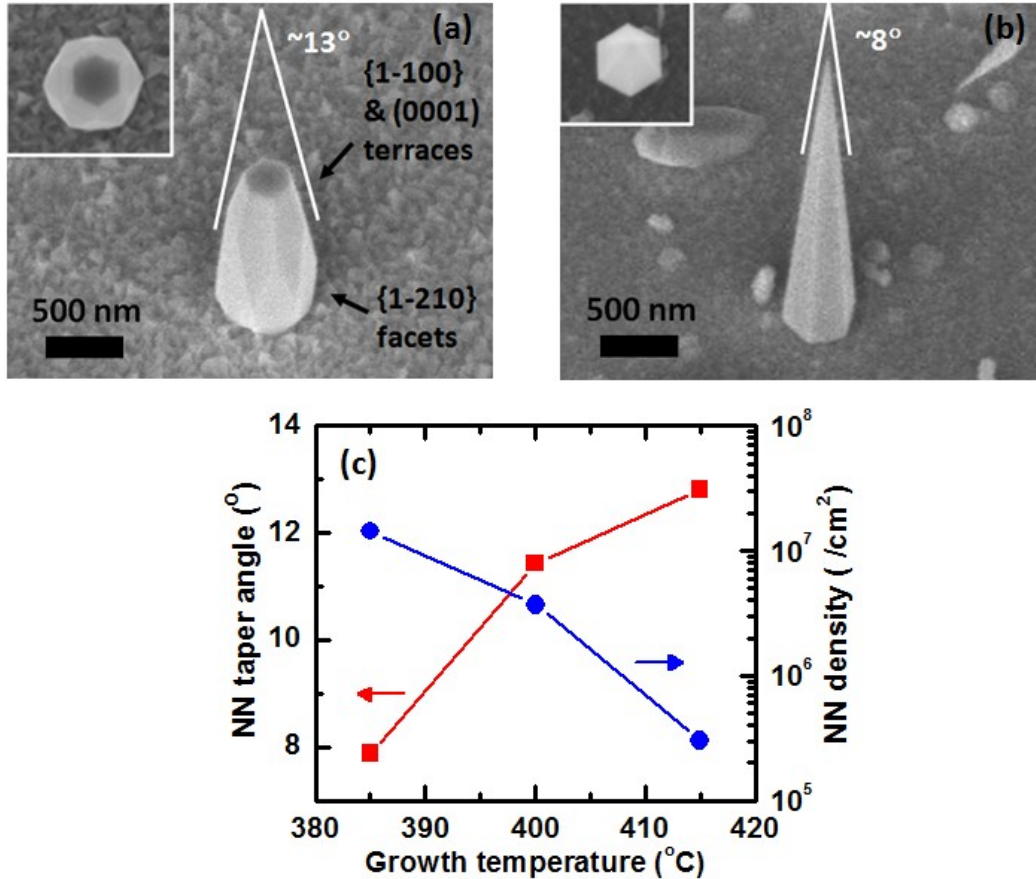


Figure 7.5 (a) 30°-tilt view of a nanoneedle grown at 415°C. Inset is the top-down view. 6 additional, $\{1\bar{2}10\}$ facets near the nanoneedle root were observed. No sharp nanoneedle was seen for this growth temperature. The additional 6 bottom facets and the flat c-plane top should be the result of the crystal energy minimization. (b) 30°-tilt view and the top-down view (inset) of a nanoneedle grown at 385°C. The nanoneedle shape still shows 6 tapered facets with sharp tip, which is similar to the nanoneedles grown at 400°C but with a smaller taper angle. (c) Nanoneedle taper angle and nanoneedle density as a function of growth temperature. The nanoneedle taper angle decreases with the decreasing growth temperature. The nanoneedle density has strong negative growth temperature dependence.

7.2 Nucleation Theory for GaAs Nanoneedles Grown on Sapphire

Through the collaboration with Dr. Vladimir G. Dubrovskii and Dr. Nickolay V. Sibirev in Ioffe Physical-Technical Institute of the Russian Academy of Sciences and Dr. Frank Glas in CNRS-LPN, France, a theoretical model of catalyst-free nanoneedle nucleation in lattice mismatched material systems is given below.

Formation enthalpy ΔG of a surface island in some simplified geometries can be written down in the form²⁰⁻²²

$$\Delta G = -\Delta\mu(V/\Omega) + \gamma_F S_F + (\gamma_W + \gamma_B - \gamma_S) S_B. \quad (7.1)$$

Here, $\Delta\mu$ is the difference of chemical potentials in the vapor and the island, V is the island volume, Ω is the elementary volume in the solid phase; γ_F is the surface energy of vertical facets of area S_F (formed due to the nucleation), γ_W is the surface energy of lateral facets (formed due to the nucleation) of area S_B , γ_B is the surface energy of solid-solid interface at the nanoneedle base of same area S_B (also formed due to the nucleation) and γ_S is the surface energy of pre-existing substrate surface (eliminated by the nucleation). Re-arranging Eq. (7.1), the formation enthalpy can be presented as the function of two variables, the number of atoms in the island $i = V/\Omega$ and the aspect ratio $\beta = L/D$, where L is the nanoneedle length and D is the base dimension:

$$\Delta G(i, \beta) = -[\Delta\mu_0 - w(\beta)]i + \pi^{1/3}(\Omega/2)^{2/3} [4\gamma_F \beta^{1/3} + (\gamma_W + \gamma_B - \gamma_S) \beta^{-2/3}] i^{2/3}. \quad (7.2)$$

Due to the lattice mismatch between the substrate and the deposit, the volume term $\Delta\mu = \Delta\mu_0 - w(\beta)$ contains two contributions: the chemical vapor-solid energy difference $\Delta\mu_0$ and the β -dependent elastic energy per atom $w(\beta)$. For the function $w(\beta)$, we use a fit to the finite element calculations of the elastic energy of a uniformly strained cylinder of the form:

$$w(\beta) = \frac{E\Omega\varepsilon_0^2}{(1-\nu)} \left[\frac{p_1}{1+p_2\beta} + (1-p_1)e^{-p_3\beta} \right], \quad (7.3)$$

This formula was obtained from linear isotropic elasticity calculations, taking identical Young's moduli E and Poisson's ratios ν for nanoneedle and substrate, with relative lattice misfit ε_0 . The p_k are ν -dependent fitting coefficients such that $p_1 = 0.5566$, $p_2 = 10.15$ and $p_3 = 9.352$ at $\nu = 0.31$. The first factor in the right hand side of Eq. (7.3) gives the elastic energy w_{2D} of a uniformly strained 2D layer and the β -dependent factor measures the effect of strain relaxation at the free lateral surfaces. Free enthalpy given by Eq. (7.2) always has a β -dependent maximum $\Delta G_*(\beta)$ in i . The nucleation barrier is now determined by the minimum of $\Delta G_*(\beta)$ in β at a certain β_* relating to the saddle point of the formation enthalpy,²¹ as shown in the insert to Fig. 7.6a. The embryos tend to maintain the energetically favorable value of β_* at the follow up stages of growth. Using Eqs. (7.2) and (7.3), the nucleation barrier $\Delta G_*(\beta)$ can be presented as $\Delta G_*(\beta) = \text{const} * f(\beta)$, where the function f is given by

$$f(x) = \frac{(x+a)^3}{x^2 \left[1 - b \left(\frac{p_1}{1+x} + (1-p_1)e^{-cx} \right) \right]^2}. \quad (7.4)$$

with $x = p_2\beta$. Here, $a = (\gamma_W + \gamma_B - \gamma_S)p_2/(4\gamma_F)$ is the constant relating to surface energy, $b = w_{2D}/\Delta\mu_0$ is the constant relating to elastic energy and $c = p_3/p_2$.

Possible behaviors of function $f(\beta)$ are shown in Fig. 7.6a. The simplest case of homoepitaxy relates to $\gamma_W = \gamma_S$, $\gamma_{WS} = 0$ and $\varepsilon_0 = 0$, yielding $a = b = 0$, where the function $f(x) = x$ is minimum at $x \rightarrow 0$. Homoepitaxial films therefore always tend to grow in a 2D form, which is indeed the well known result²². For heteroepitaxial lattice matched systems ($b = 0$, $a \neq 0$), the case of $a < 0$ ($f(0) = -\infty$, wetting system) relates to 2D layer and $a > 0$ ($f(0) = +\infty$, non-wetting system) to 3D islands.²² Strain-driven catalyst-free growth of nanoneedles with high aspect ratios requires a sufficiently large contribution of the elastic energy such that $b \gg 1$. This is well illustrated by the modification of the curves in Fig. 7.6a with increasing b . In calculations, we use the known constants of ZB GaAs ($\nu = 0.31$, $E = 8.6 \times 10^{10}$ Pa, $\Omega = 0.0225 \text{ nm}^3$),²³ at typical $\Delta\mu_0 = 100 \text{ meV}$,²⁴ yielding $b = 38$ at $\varepsilon_0 = 0.46$. The curves in Fig. 7.6b show that the value of surface energy constant a is not very important for the strain-induced formation of nanoneedles: the aspect ratio increases to very large values ~ 4.5 - 6.8 at $\varepsilon_0 = 0.46$ for both wetting ($a = -6$, $a = 0$) and non-wetting ($a = 6$) cases. The obtained aspect ratios include the experimentally observed range: taper angle $\theta = 10$ - 12° corresponds to $\beta_* = 4.8 - 5.7$. Since the energetic constants of hexagonal and cubic phases should have the same order of magnitudes, this will remain qualitatively valid also for WZ GaAs nanoneedles. As discussed in Ref. 20 and Refs 25-27, small nanoneedles may initially form in WZ phase due to a lower effective surface energy of $\{1\bar{1}00\}$ lateral facets and then will continue to grow as WZ.

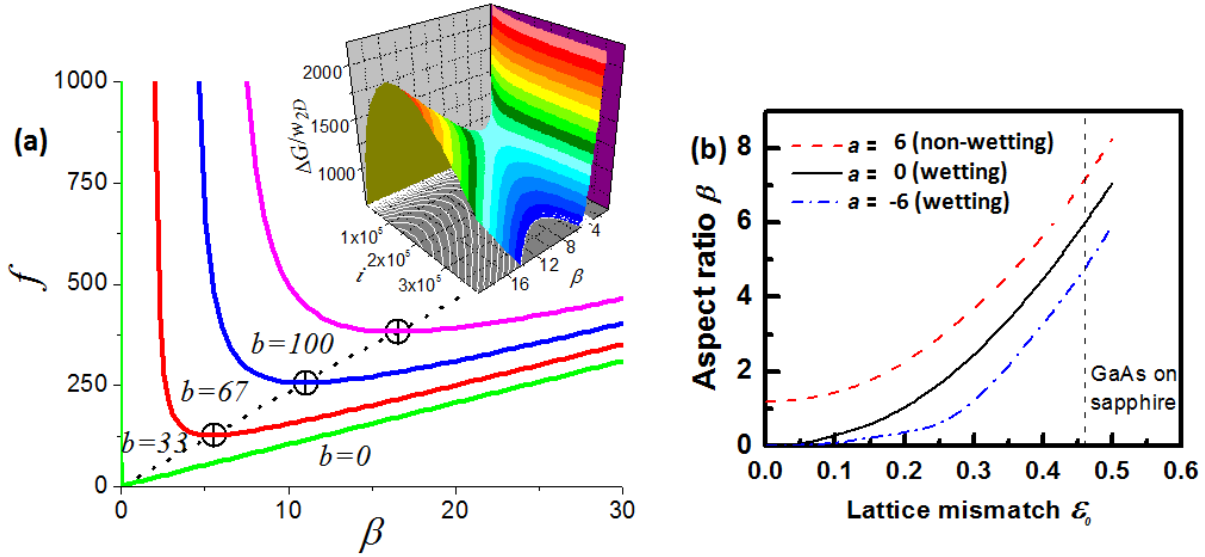


Figure 7.6 (a) Functions $f(\beta)$ at different b and fixed $a = 6$, dotted line shows the shift of saddle point β_* at increasing b (a). The insert shows the saddle shape of the relative nucleation barrier $\Delta G/w_{2D}$ over the (i, β) plane at $b = 38$, relating to the case of GaAs nanoneedles on sapphire. It is seen that for a larger b (corresponding to large lattice misfit), the optimum β (aspect ratio) is also larger. (b) Dependences of aspect ratio on the lattice misfit at different a .

With the above nanoneedle nucleation model, the nanoneedle taper angle versus the growth temperature dependence shown in Fig. 7.5c can be explained as the following. For MOCVD growth, a lower growth temperature would be corresponding to a smaller $\Delta\mu_0$, because of a lower precursor decomposition rates. According to the definition of $b = w_{2D}/\Delta\mu_0$, b would be larger for lower growth temperatures. From Fig. 7.5b, a larger nanoneedle aspect ratio hence a smaller nanoneedle taper angle would be expected at a lower growth temperature. Experimentally observed decrease of nanoneedle density with increasing the growth temperature, demonstrated by Fig. 7.5c, can be quantitatively explained by the known temperature dependence of the island morphology in a kinetically controlled nucleation mode with the density typically exponentially decreasing at larger T .²⁸ Quantitative analysis requires, however, the consideration of an ensemble of nanoneedles rather than a single nanoneedle and will be presented elsewhere.

7.3 Optical Properties of GaAs Nanoneedles Grown on Sapphire

The optical properties of the GaAs nanoneedles were investigated by μ -PL. The excitation laser was an Argon laser at 514 nm and the spot size was focused down to $\sim 1.5 \mu\text{m}$ in diameter to pump only one single nanoneedle. Fig. 7.7a is the typical 4 K μ -PL spectra of a nanoneedle grown at 400°C for 60 minutes, with annealing temperature = 606°C and V/III ratio = 48. Two peaks are clearly seen especially for excitation powers below 500 μW . The PL spectra are fitted

with two Lorentzian functions in order to accurately determine the peak energies. A fitting example for the PL spectrum with the 100 μW excitation power is shown in Fig. 7.7b. The two peaks are at 1.505 eV and 1.519 eV, respectively. The intensities of the two peaks are comparable for this 100 μW excitation. The intensities of the two peaks as a function of the excitation power are then plotted in Fig. 7.7c. The ~ 1.519 eV peak increases a little superlinearly with the excitation power while the ~ 1.505 eV peak starts to saturate at 500 μW and above. Based on the power dependence of the two peaks, ~ 1.519 eV peak is assigned as the free exciton emission and ~ 1.505 eV peak as the impurity related emission. The linewidth of the free-exciton peak at 1.519 eV is a narrow 18 meV (Fig. 7.7b) even under the 46% lattice mismatch. It is only slightly larger than the 7 meV reported by Hoang *et al.* from the measurement of WZ GaAs nanowires grown on a GaAs substrate,¹³ and is comparable to the 23 meV reported by Titova *et al.* for AlGaAs-passivated GaAs nanowires, also on a GaAs substrate.²⁹ The narrow linewidth from the WZ GaAs nanoneedles indicates good crystal quality. The power dependence of the two peak energy positions is shown in Fig. 7.7d. Firstly, the two peak energies show redshift as the excitation power increases (Fig. 7.7d). We attribute this redshift to the thermal effect. Secondly, the difference between the two peak energies is a fixed 14 meV for all the excitation powers. This further verifies that the ~ 1.505 eV peak is a shallow-impurity related transition which is with 14 meV less energy than the free-exciton energy for WZ GaAs. The exact type of this shallow impurity and the details of this impurity-related transition require further investigation. Carbon is currently suspected since it is the most common residual impurity for MOCVD-grown undoped GaAs and the carbon related transition is ~ 22 meV less than the free-exciton energy for ZB GaAs.³⁰ The 1.519 eV free-exciton energy for WZ GaAs nanoneedles is 4 meV larger than that of ZB GaAs. This is very close to the 7 meV reported by Martelli *et al.* from a WZ GaAs nanowire measurement.³¹

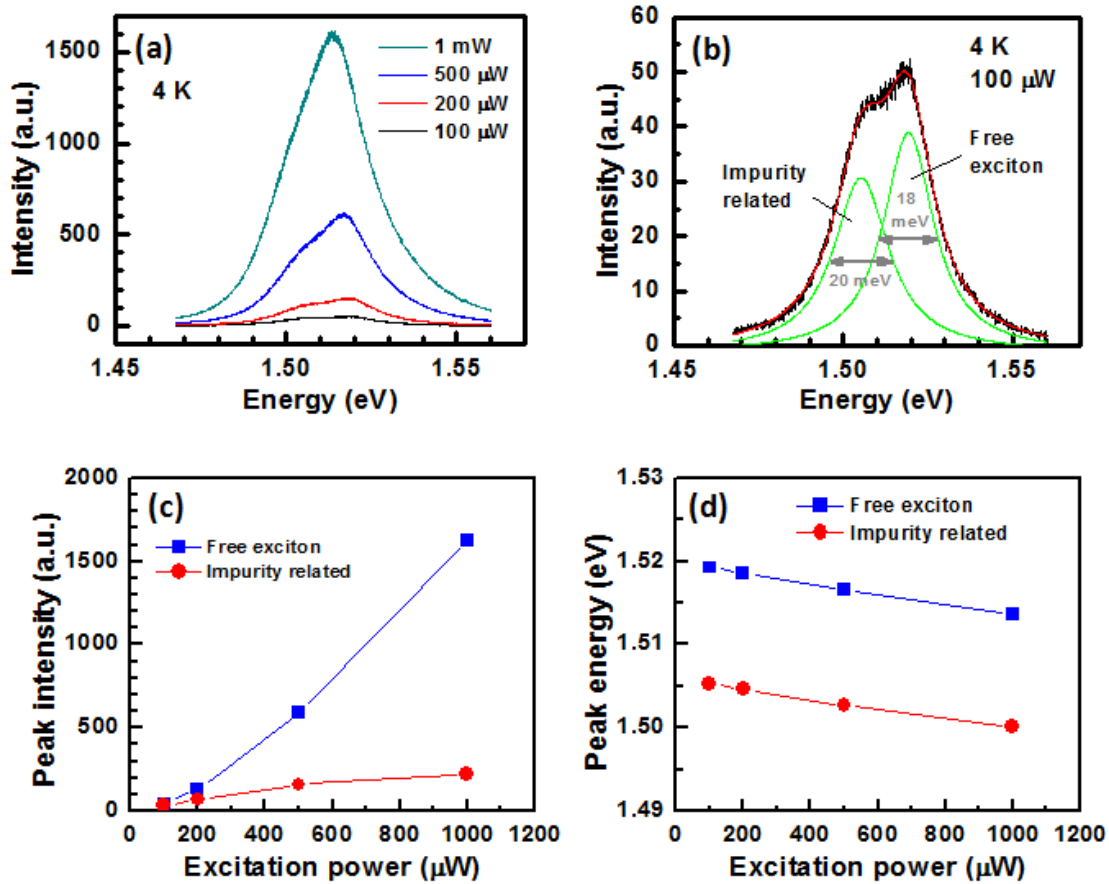


Figure 7.7 4 K μ -PL study of nanoneedles grown at 400°C with V/III = 48. (a) μ -PL spectra for a nanoneedle with various excitation powers. Two peaks were seen especially for lower excitation powers. (b) A two-Lorentzian fitting example for the spectrum with 100 μ W excitation power. Two peaks at 1.505 eV and 1.519 eV are seen. The linewidth of the two peaks is 20 meV and 18 meV, respectively. The narrow linewidth indicates good crystal quality. The 1.505 eV peak is later assigned as the impurity related transition and the 1.519 eV peak as the free-exciton recombination. (c) Peak intensity as a function of excitation power for the two peaks. The \sim 1.519 eV peak (free exciton) intensity increases with the excitation power while the \sim 1.505 eV peak (impurity related) starts to saturate for 500 μ W and higher excitations. (d) Peak energies as a function of excitation power for the two peaks. The difference is a constant 14 meV for all the excitations.

Room-temperature μ -PL was also measured and is shown in Fig. 7.8. Only one single peak can be observed at room temperature. This is expected since the previously mentioned impurity level is too shallow to be seen with the thermal energy $kT \sim 25$ meV at room temperature. This single peak is therefore assigned to the bandedge emission. The assignment is also due to that the intensity does not saturate as the excitation power increases. The room-temperature peak energy of the lowest pumping level, 500 μ W, is 1.432 eV. This is 8 meV larger than the bulk 300 K ZB GaAs bandgap of 1.424 eV. The 8 meV Room-temperature WZ-to-ZB bandgap difference is close to the 4 meV WZ-to-ZB free-exciton energy difference determined at 4 K. Overall the free-

exciton recombination dominates the 4 K PL with a narrow linewidth. This testified the excellent crystal quality of GaAs nanoneedles even with a 46% lattice mismatch to the sapphire substrate.

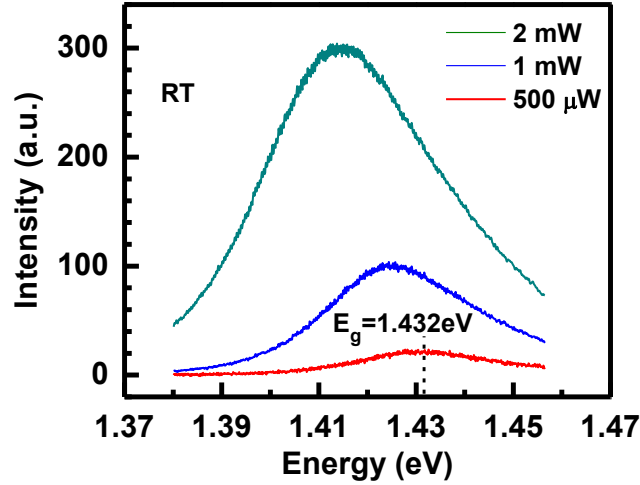


Figure 7.8 Room-temperature μ -PL spectra for a nanoneedle with various excitation powers. Only one peak, the bandedge emission, can be seen since the large thermal energy kT of ~ 25 meV. The peak energy redshifts as the excitation power increases due to the thermal effect.

In conclusion, we reported here the first demonstration of catalyst-free, self-assembled growth of epitaxial WZ GaAs nanoneedles on a 46% lattice-mismatched sapphire substrate. The nanoneedles are with a hexagonal cross section, a sharp tip with a typically less than 3 nm diameter and a small nanoneedle taper angle of 11° . The nanoneedle tapering is a result of the $\{1\bar{1}00\}$ and (0001) terraces. The nanoneedle in-plane orientation is identified with a 30° rotation to the c-plane sapphire substrate, which is required to align WZ GaAs onto a c-sapphire substrate. The vapor-solid growth mechanism of GaAs nanoneedle seeds is discussed via the nanoneedle density dependence on V/III ratio. Annealing temperatures have impact to the nanoneedle density while the growth temperatures have impact to the nanoneedle shape as well as the nanoneedle density. The catalyst-free, strain-induced nucleation model shows that the nanoneedles can reach a high aspect ratio relating to the experimentally observed taper angle of 10 - 12° at 46% lattice mismatch. 4 K and room-temperature μ -PL have been measured and bright photoluminescence was seen despite of the large lattice mismatch. This high-quality GaAs nanoneedle opens an opportunity for fabricating high-quality electronic and optoelectronic devices onto a sapphire substrate.

References:

- (1) Fang, S. F., *et al.* Gallium arsenide and other compound semiconductors on silicon. *J. Appl. Phys.* **68**, R31-R58 (1990). (maybe also Razeghi's text book)
- (2) Lum, R. M. *et al.* Effects of misfit dislocations and thermally induced strain on the film properties of heteroepitaxial GaAs on Si. *J. Appl. Phys.* **64**, 6727-6732 (1988).
- (3) Stoica, T. & Vescan L. Misfit dislocations in finite lateral size $\text{Si}_{1-x}\text{Ge}_x$ films grown by selective epitaxy. *J. Cryst. Growth* **131**, 32-40 (1993). (maybe also GaN pyramid)
- (4) Chuang, L. C., Moewe, M., Chase, C., Kobayashi, N. P., and Chang-Hasnain, C. Critical diameter for III-V nanowires grown on lattice-mismatched substrates. *Appl. Phys. Lett.* **90**, 043115 (2007).
- (5) Glas, F. Critical dimensions for the plastic relaxation of strained axial heterostructures in free-standing nanowires. *Phys. Rev. B* **74**, 121302 (2006).
- (6) Ertekin, E., Greaney, P. A., Chrzan, D. C., & Sands, T. D. Equilibrium limits of coherency in strained nanowire heterostructures. *J. Appl. Phys.* **97**, 114325 (2005).
- (7) Kenty, J. L. Physical vapor deposition of GaAs on single crystal sapphire. *J. Electron. Mater.* **2**, 239-254 (1973).
- (8) Kasai, K., Nakai, K., & Ozeki, M. Material and device properties of GaAs on sapphire grown by metalorganic chemical vapor deposition. *J. Appl. Phys.* **60**, 1-5 (1986).
- (9) Diebold, A. C. *et al.* Growth and characterization of GaAs on sapphire (0001) by molecular beam epitaxy. *Surf. Interface Anal.* **15**, 150-158 (1990).
- (10) Moewe, M., Chuang, L. C., Crankshaw, S., Chase, C., & Chang-Hasnain, C. Atomically sharp catalyst-free wurtzite GaAs/AlGaAs nanoneedles grown on silicon, *Appl. Phys. Lett.* **93**, 023116 (2008).
- (11) Lei, T., Ludwig, K. F. Jr., & Moustakas, T. D. Heteroepitaxy, polymorphism, and faulting in GaN thin films on silicon and sapphire substrates. *J. Appl. Phys.* **74**, 4430-4437 (1993).
- (12) McMahan, M. I. & Nelmes, R. J., Observation of a wurtzite form of gallium arsenide. *Phys. Rev. Lett.* **95**, 215505 (2005).
- (13) Hoang, T. B. *et al.* Observation of free exciton photoluminescence emission from single wurtzite GaAs nanowires, *Appl. Phys. Lett.* **94**, 133105 (2009).
- (14) Begum, N. *et al.* Structural characterization of GaAs and InAs nanowires by means of Raman spectroscopy. *J. Appl. Phys.* **104**, 104311 (2008).
- (15) Soga, T., George, T. Jimbo, T., & Umeno, M. Initial growth mechanism for GaAs and GaP on Si substrate by metalorganic chemical vapor deposition. *J. Appl. Phys.* **30**, 3471-3474 (1991).
- (16) Soga, T. *et al.* Transmission electron microscopy characterization of the initial stage of epitaxial growth of GaP on Si by low-pressure metalorganic chemical vapor deposition. *Appl. Phys. Lett.* **58**, 2108-2110 (1991).
- (17) Yamamoto, A., Tsujino, M., Ohkubo, M., Hashimoto, A. Nitridation effects of substrate surface on the metalorganic chemical vapor deposition growth of InN on Si and $\alpha\text{-Al}_2\text{O}_3$ substrates. *J. Cryst. Growth* **137**, 415-420 (1994).
- (18) Uchida, K. Nitridation process of sapphire substrate surface and its effect on the growth of GaN. *J. Appl. Phys.* **79**, 3487-3491 (1996).

- (19) Taylor, J. E., Cahn, J. W., & Handwerker, C. A. Geometric models of crystal growth. *Acta metall. Mater.* **40**, 1443-1474 (1992).
- (20) Dubrovskii, V.G. & Sibirev, N.V. Growth thermodynamics of nanowires and its application to polytypism of zinc blende III-V nanowires. *Phys. Rev. B* **77**, 035414 (2008).
- (21) Osipov, A.V., Schmitt, F., Kukushkin, S. A., & Hess, P. Stress-driven nucleation of coherent islands: theory and experiment. *Appl. Surf. Sci.* **188**, 156-162 (2002).
- (22) Kashchiev, D. *Nucleation: basic theory with applications*. (Butterworth Heinemann, Oxford, 2000).
- (23) *Group IV Elements, IV-IV and III-V compounds*, edited by U. Rössler, Landolt-Börnstein, New Series, Group III, Vol. 41, Part A (Springer, Berlin, 2006).
- (24) Moewe, M., Chuang, L. C., Dubrovskii, V. G., & Chang-Hasnain, C. Growth mechanisms and crystallographic structure of InP nanowires on lattice-mismatched substrates *J. Appl. Phys.* **104**, 044313 (2008).
- (25) Glas, F., Harmand, J. -C., & Patriarche, G. *Phys. Rev. Lett.* **99**, 146101 (2007).
- (26) Leitsmann, R., & Bechstedt, F. Surface influence on stability and structure of hexagon-shaped III-V semiconductor nanorods. *J. Appl. Phys.* **102**, 063528 (2007).
- (27) Akiyama, T., Sano, K., Nakamura, K. & Ito, T. An empirical potential approach to wurtzite-zinc-blended polytypism in group III-V semiconductor nanowires. *Jpn. J. Appl. Phys.* **45**, L275 (2006).
- (28) Dubrovskii, V. G., Cirilin, G. E., & Ustinov, V. M. Kinetics of the initial stage of coherent island formation in heteroepitaxial systems. *Phys. Rev. B* **68**, 075409 (2003).
- (29) Titova, L. *et al.* Temperature dependence of photoluminescence from single core-shell GaAs-AlGaAs nanowires. *Appl. Phys. Lett.* **89**, 173126 (2006).
- (30) Haacke, G., Watkins, S. P., & Burkhard, H. Epitaxial growth of high-mobility GaAs using tertiarybutylarsine and triethylgallium. *Appl. Phys. Lett.* **56**, 478-480 (1990)
- (31) Martelli, F. *et al.* Photoluminescence of Mn-catalyzed GaAs nanowires grown by molecular beam epitaxy. *Nanotechnol.* **18**, 125603 (2007).

Chapter 8:

Conclusion

In this dissertation, I discussed the growth and characterization as well as the device demonstrations of III-V nanowires and nanoneedles on lattice mismatched substrates such as Si and sapphire. These one dimensional materials are with excellent crystal quality even under the large lattice mismatch. The growth temperatures of these nanomaterials are also low and CMOS-compatible.

Regarding the III-V nanowire epitaxial critical diameter study, I reported the experimental evidence of a critical diameter for epitaxial-nanowires on lattice-mismatched substrates, with nanowires smaller than this value demonstrating extremely narrow PL linewidths and bright PL intensity. I showed that critical diameter is inversely dependent on the lattice mismatch. The critical diameter can serve as a general guideline in heterogeneous material growth for obtaining high brightness, well-aligned III-V nanowires on Si or other dissimilar substrates. This observation will be important for monolithic integration of optoelectronic and electronic devices with highly mismatched lattice constants.

In searching for the optimum growth conditions for InP nanowires, I showed the V/III ratio effects on both the shape and optical properties for InP nanowires grown on (111) Si substrates. The higher the V/III ratio is, the more tapered the nanowires become. The PL intensity increases dramatically with the V/III ratio. When the V/III ratio is optimized to 67, non-tapered InP nanowires were grown. These nanowires show a record narrow PL peak and weak excitation-power dependence, resembling features of ideal one-dimensional structures. In our experiments, non-tapered InP nanowires could be synthesized for V/III ratios ranging from 60-90 hence offering a reasonable growth window. I also showed that the PL peak intensity could be increased with the increase of V/III ratio.

For the exciting, novel GaAs-based nanoneedle growth study, I showed that nanoneedles can be grown epitaxially on to a GaAs, Si or a sapphire substrate. Nanoneedles with an ultra sharp tip of only a few nanometers and a small taper angle are synthesized on GaAs with Ge catalyst and mechanical scratching, on Si with only scratching, and completely spontaneous without any surface treatment on a sapphire substrate. This is attributed to the 46% large lattice mismatch between GaAs and sapphire which favors the 3D growth mode. Bulk InGaAs nanoneedles and InGaAs/GaAs QW nanoneedles are also successfully demonstrate which allow the emission wavelength engineering from the GaAs wavelength all the way to redder than the Si bandgap. As a consequence InGaAs/GaAs QW nanoneedle structures are suitable active materials for Si Photonics. AlGaAs nanoneedles and AlGaAs-passivation of GaAs nanoneedles are also demonstrated. The AlGaAs-shell/GaAs-core nanoneedle structures show $\sim 5x$ room-temperature PL intensity improvement than that of a bare GaAs nanoneedle. The proper AlGaAs passivation largely reduces the non-radiative surface recombinations of a GaAs surface.

For modifying the electrical properties of nanoneedles, GaAs nanoneedles grown on Si have seen successfully doped n-type with Si and Te, and p-type with Zn. The doping sources used were disilane, DETe, and DEZn. Both the Te and Zn dopings show higher than $10^{18}/\text{cm}^3$ doping levels, which will be suitable for typical electronic and optoelectronic devices. For lightly doped n-type GaAs nanoneedle up to $\sim 10^{17}/\text{cm}^3$, Si doping can also be used. I also demonstrated

a p-n junction inside a core-shell GaAs nanoneedle structure with excellent I-V characteristics. The process leading to this high quality device involves the isolation or removal of the connecting layer, which is a known current leakage path.

For the device-level work, I demonstrated a GaAs-nanoneedle-based PD grown on Si. A current gain is seen. The nanoneedle PD shows a high current gain of 70 at a relatively low bias voltage of 10 V. Two possible gain mechanisms, avalanche multiplication and phototransistor gain, are discussed. A core-shell $\text{In}_{0.3}\text{Ga}_{0.7}\text{As}/\text{GaAs}$ QW nanopillar LED structure with $\text{Al}_{0.2}\text{Ga}_{0.8}\text{As}$ cladding was also grown on an n^+ -(111)Si substrate via the novel nanoneedle growth mode. The room-temperature PL has an emission peak at ~ 1142 nm with a narrow FWHM of only 83 meV. The LED device shows a I-V curve with ~ 1 V turn-on voltage and a room-temperature linear L-I dependence. The capability of integrating III-V detectors and emitters on Si with the CMOS-compatible growth and processing conditions would enable important applications such as the on- or off-chip optical interconnects.

Lastly, we reported here the first demonstration of catalyst-free, self-assembled growth of epitaxial WZ GaAs nanoneedles on a 46% lattice-mismatched sapphire substrate. The nanoneedles are with a hexagonal cross section, a sharp tip with a typically less than 3 nm diameter and a small nanoneedle taper angle of 11° . The nanoneedle tapering is a result of the $\{1\bar{1}00\}$ and (0001) terraces. The nanoneedle in-plane orientation is identified with a 30° rotation to the c-plane sapphire substrate, which is required to align WZ GaAs onto c-sapphire. The catalyst-free, strain-induced nucleation model shows that the nanoneedles can reach a high aspect ratio relating to the experimentally observed taper angle of $10\text{-}12^\circ$ at 46% lattice mismatch. 4 K and room-temperature μ -PL have been measured and bright photoluminescence was seen despite of the large lattice mismatch. This high-quality GaAs nanoneedle opens an opportunity for fabricating high-quality electronic and optoelectronic devices onto a sapphire substrate.